Structural and electrical properties of MnO films grown by pulsed laser deposition

Submitted by

Sin Wai Lun

A thesis submitted in partial

fulfillment of the requirements

for the Degree of

Master of Philosophy in Physics

at

The Department of Applied Physics

The Hong Kong Polytechnic University

December 2003

CERTIFICATE OF ORIGINALITY

I hereby declare that this thesis is my own work and that, to the best of my knowledge and belief, it reproduces no material previously published or written nor material which has been accepted for the award of any other degree or diploma, except where due acknowledgement has been made in the text.

_____(Signed)

_____SIN WAI LUN_____(Name of student)

Abstract

Manganese monoxide (MnO) thin films of pure rock salt structure were prepared on single crystal MgO(001) and TiN buffered silicon(001) substrates by pulsed laser deposition method using dense ceramic Mn_3O_4 targets. In general, single phase MnO films were obtained at low ambient oxygen pressure of $< 10^{-4}$ Torr. Structural characterization by X-ray diffraction (XRD) showed that the MnO films started to crystallize at growth temperature as low as 200 °C. Progressively improved crystalline structure and orientation were seen at higher deposition temperatures. XRD 360°-phi scans revealed epitaxial relationships of (001)MnO||(001)TiN||(001)Si and (001)MnO||(001)MgO for MnO films grown at low substrate temperature of 300 °C. MnO films of excellent structural quality were obtained at 600 °C and under a base pressure of 2×10^{-5} Torr. In the case of MnO/TiN/Si, higher deposition temperature, however, caused structural deterioration in the MnO films due to chemical interdiffusion across the interface and oxidation of the TiN sub-layer. The electrical properties of the epitaxial MnO films integrated with Si were examined by depositing platinum spot electrodes to form a Pt/MnO/TiN/Si capacitor structure. MnO films grown at optimum condition yielded a room temperature dielectric constant of 17.4 with a dissipation factor as small as 0.049 at 10 MHz. They exhibited dielectric constant similar to that of bulk MnO single crystal. The correlation between leakage current and film thickness was also investigated. With an E-field of 1×10^5 V cm^{-1} applied across the MnO film, the leakage current

decreased from 78.6 to 1.17×10^{-8} A cm^{-2} for a film thickness change from 37 nm to 450 nm.

Resistivity versus temperature measurements revealed that the MnO films had a semiconducting transport behavior. Films deposited on MgO substrate exhibited a hopping energy of 0.51 eV and a thermal coefficient of resistivity that varied from -5.5 to -2.4 % K^{-1} for different deposition pressure. Electrical measurements thus showed possible applications of MnO films as negative temperature coefficient (NTC) thermistor.

Heteroepitaxial structures of Au/MnO/TiN/MgO(111) were also prepared. Electrical measurements on these heterostructures at temperature from 80 K to 310 K showed no obvious dielectric anomaly as those observed in bulk samples. This deviation was partially attributed to the stress and asymmetric interface nature of the thin film.

Mixed-metal monoxides of composition of $Mn_xCo_{1-x}O$ were fabricated too. Structural and electrical conduction of epitaxial films with $0<x<1$ were studied. The lattice parameters of these films were tuned from 0.426 nm to 0.441 nm according to Vegard's law based on the mole ratio (x). The structural measurement showed possible applications as template for strain layer growth.

THE HONG KONG POLYTECHNIC UNIVERSITY

ACKNOWLEDGEMENTS

I would like to acknowledge Dr. K. H. Wong, for his close supervision throughout these two years. I also thank to Mr. K. S. So for his enlightenment, encouragement and support during my study. Special thanks are also due to Dr. W.B. Wu, for his suggestions and discussion on my research work. I would like to thank my research companions, Mr. W.S. Tsang, Mr. S.F. Wong, Miss. F.F. Hau and Miss. C.Y. Lam, for their useful suggestions. I am heartfelt grateful to Miss. P.Y. Chu for her encouragement and kindness.

I owe a great deal of my accomplishment to the immeasurable love and the never-ending support of my parents. They are the ones who always believe that my efforts will be rewards.

List of Figures

List of Tables

TABLE OF CONTENTS

CHAPTER 3   21

Characterization method

CHAPTER 4   35

Fabrication and characterization of MnO on TiN buffered Si substrate

CHAPTER 5   74

Fabrication and characterization of MnO on MgO substrate

CHAPTER 1

Introduction

1.1 Background

Metal oxide thin films, which become more and more important in micro-electronic devices [Prinz et al., 1995, Dax, M., 1997], have attracted much attention lately. Oxide materials possess a wide range electrical properties spanning from insulators to high temperature superconductors and from ferroelectrics to ferromagnetic materials. Apart from many useful applications, there is however a general interest in oxide thin films fabrication and characterization, especially in the case of the 3d transition metal oxide (TMO) [Muller et al., 2002].

Among the 3d transition metal oxides, manganese monoxide (MnO) is of particular importance due to the high spin ground state of the $3d^5$ configuration of Mn^{2+}. Therefore, MnO could be an excellent model system to investigate many kinds of spin dependent or magnetic interactions between electrons in the surface of an antiferromagnetic solid. The electronic structure of MnO in the bulk form has been extensively studied for many years. But in practice, most experimental investigations on crystalline MnO surface of a bulk sample always suffer from bad structural quality. For example, the cleavage of a single crystal along the MnO(001) plane usually leads to a surface structure that consists of arrays of pyramids with (111) surface [Henrich et al., 1996]. So, one of the challenges is to provide a good crystalline MnO surface for further studies [Muller et al., 2002].

1.2 Manganese Oxide

Manganese monoxide (MnO) is the simplest form of manganese oxide in terms of its geometric and electronic structure. It occurs naturally as a relative rare mineral. As shown in Fig. 1.1, MnO possesses a rocksalt crystal structure with a lattice constant of 0.444 nm [Pearson et al., 1958] in their paramagnetic phase above the Néel temperature T_N=118 K. Below T_N, it is a type-II antiferromagnetic (AFM II) insulator with rhombohedrally-distorted structure (see Fig. 1.2). The rhombohedral distortion takes the form of compression along the [111] direction and changes the angles of the cubic structure from $90°$ to $90.62°$ [Roth et al., 1958; Haywood et al., 1971]. The distortion, however, is small and the structure is usually considered as cubic symmetry even below T_N [Gupta et al., 1977]. Recent theoretical investigation gives evidence that this assumption is not valid [Massidda et al., 1999]. Even assuming a perfect cubic ionic arrangement below T_N, the antiferromagnetic ordering by itself induces substantial non-cubic behavior of some non-magnetic properties, such as the dielectric anomaly.
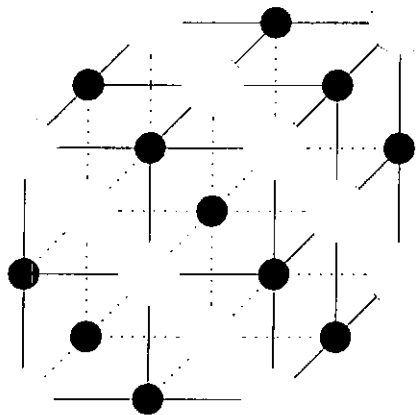
Figure 1.1 Rocksalt structure of manganese monoxide (MnO).
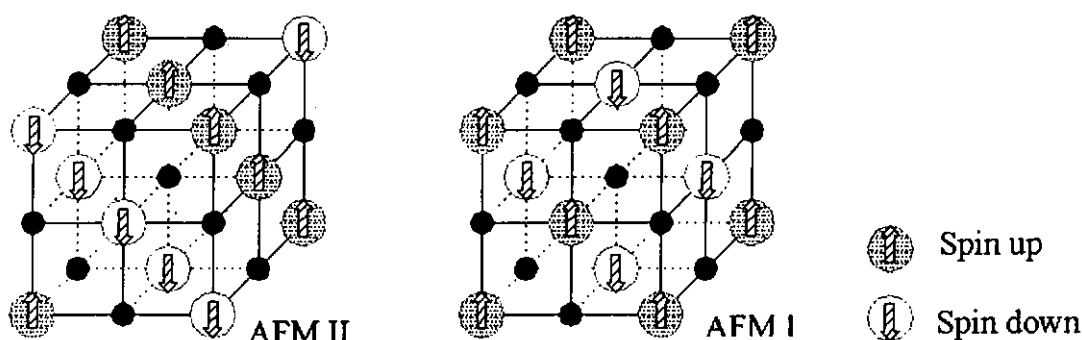
Figure 1.2 AFM I ([001]) and AFM II ([111]) magnetic orderings in a rocksalt structure. In the AFM I structure, ferromagnetic planes stack along the [001] direction; in AFM II, the structure consists of ferromagnetic [111] planes stacked antiferromagnetically in the direction normal to the planes.

Manganese exhibits formal oxidation state of +2, +3 and +4 in the solid form [Levason, et al., 1972]. Among these oxides, manganese in high oxidation states such as Mn_2O_3 (C-Rare Earth Structure) or Mn_3O_4 (Spinel) [Galasso et al., 1970] are the most stable ones. According to Langell [Langell et al., 1996], MnO(001) can be selectively oxidized to produce Mn_2O_3- and Mn_3O_4- like surfaces under mild oxidation. Indeed, the oxidation state of manganese can be readily altered under different oxidation/reduction environment. In addition these oxidation phases are easily intermixed and it is difficult to isolate pure phase layers that are uncontaminated by other oxide phases.

The ready formation and intermixture of these oxide species, on the other hand, imply that the redox-properties of manganese oxide surfaces are important in determining their surface chemical reactivity and gas adsorption characteristics. Thus, this series of oxides show a good catalytic function because of their ability to change

their oxidation states. They can strongly absorb other substance on to their surfaces, and activate them in the chemical reaction [Henrih et al. 1996]. In a single crystal MnO, the oxide itself exhibits an appreciable metal deficit ($Mn_{1-y}O$) at high temperature. The y may have values of up to 0.15. Studies of nonstoichiometry in MnO single crystal have been reported based on bulk sample [Davies et al., 1959; Hed et al., 1967]. It is agreed that the deviation from stoichiometry in the MnO phase is a function of partial pressure of oxygen and temperature. In fact MnO-like films can be fabricated in a precisely controlled oxygen ambient condition. Higher oxidation impurities, however, persist in most cases.

There are many studies on the preparation of rocksalt TMO films. Various thin film preparation techniques, such as thermal evaporation, RF sputtering, molecular beam epitaxy, metal-organic chemical vapor deposition, and pulsed laser deposition have been used. Pulsed laser deposition (PLD) is a promising and versatile technique for growing complex oxide thin films [Neubeck et al., 1999]. In this project, we have fabricated epitaxial MnO thin films by PLD method. The quality of the deposited films is determined by various characterization techniques. It is also aimed to identify a set of optimized parameters, including substrate temperature, laser energy and ambient oxygen pressure, that can reliably produce pure phase MnO films on different substrates.

1.3 Outline of thesis

This thesis describes the experimental investigation of manganese oxide (MnO) thin films deposited by pulsed laser deposition. The objectives in the research can be divided into two main parts. (1) The development of the pulsed laser deposition system for producing high quality MnO thin films. This includes experimental investigation of the fundamental properties and phenomena of the deposition process in order to understand the behavior of the MnO thin films as a function of the deposition condition. As a result, optimized deposition conditions like substrate temperature and ambient pressure are identified and used in the fabrication of high quality MnO films. (2) The electrical properties of the MnO thin films grown on different substrates and electrodes, and having different crystalline orientations are studied. The aim is to gain a better understanding of the relation between their electrical characteristics and their structural properties. The potential applications of MnO thin film are also discussed.

In Chapter 2, a brief description on the fundamental mechanism of PLD is presented. Topics on epitaxial growth mode of thin film are also reviewed. The PLD system used in the present studies is presented in the second half of this chapter. The advantages and disadvantages of PLD are also explicitly described.

The thin film characterization techniques in the present studies are addressed in Chapter 3. The working principles of some major characterization equipments such as X-ray diffractometry (XRD) are discussed. Techniques of SEM, surface profiling,

leakage current measurement, dielectric measurement and temperature-resistivity measurement are also explained.

In Chapter 4, we report the fabrication and characterization of MnO films on TiN buffered silicon substrates. An emphasis is placed on the correlation between the film quality and the deposition conditions. The dielectric properties of the MnO film prepared by PLD are discussed.

In Chapter 5, results of MnO films grown on insulating MgO(001) and MgO(111) single crystal substrates are given. The temperature dependent electrical conductivity which varies as a function of deposition pressure is presented. The investigation of the dielectric anomaly in MnO(111) oriented thin film due to magnetic transition of MnO is also given in this chapter.

Chapter 6 deals with the fabrication and characterization of $Mn_xCo_{1-x}O$ films. Different substrates such as TiN/Si(001), MgO(001) and MgO(111) are used. The structural and electrical properties of the films are characterized and compared.

Conclusions of this thesis with a summary of the important results and achievements attained in the present investigation are given in Chapter 7. In view of the successes of PLD of MnO films, as demonstrated in our work, suggestions for further studies in the future, on MnO in particular, and on all transition metal monoxide in general, are given at the end of this same chapter.

CHAPTER 2

Pulsed Laser Deposition

2.1 Introduction

Among the large number of processes to fabricate thin films of materials, pulsed laser deposition (PLD) has emerged as a versatile method to obtain epitaxial and single crystal like thin films of multi-component oxides. Thin films of high Tc superconducting oxide [Dijkkamp et al., 1987], ferroelectric [Ramesh et al., 1990], ferromagnetic [Haupt et al., 1992], dielectric oxides [Bykovskii et al., 1978] and their multilayers have been successfully grown by this method.

Conceptually and experimentally, PLD is an extremely simple technique. A pulsed laser beam enters a vacuum chamber through a window and impinges on the target material to be deposited. The laser is focused to an energy density of up to a few J cm^{-2}. The short duration (in our case $\sim$ 20 ns) of the laser pulse ensures that only the surface layer of the ablation target is being heated up. This is because the thermal conduction has not set in for such a short time scale. Consequently, all the absorbed laser energy is confined within the surface layer, which attains a few thousand degree Celsius quite easily. The result is the congruent evaporation of the target materials − a unique and useful feature of PLD of multicomponent oxide thin films. Typically, laser ablation is done using UV-wavelength lasers due to their high absorption coefficient for a large variety of materials. The most commonly used laser

is excimer laser with wavelengths spanning from 157 to 351 nm, depending on the selected gas mixture employed.

Laser beam-solid interaction is a complex phenomenon. Energy of the laser photon is absorbed by the solid surface leading to electronic excitation. Since thermal conductivity of the target solid is far too slow to dissipate energy in the short period of the laser pulse, photon energy is converted into thermal and chemical energy. Due to the local heating, temperature of the order of 3500 °C is reached in a small volume at near the target surface, leading to instantaneous evaporation, ionization and decomposition of the materials.

The ejected vapor contains neutral atoms, positive and negative ions, electrons, molecules, molecular ions and free radicals of the target material in their ground and excited states. These particles acquire high kinetic energy and move in the direction perpendicular to the target surface. The moving front of such a collection of particles constituting a luminous plasma is called the plume (see Fig. 2.1). The plume is highly directional with a distribution of $\cos^n\theta$ [Singh et al.,1990], where n can be up to 10. The sum total of all the particles in the plume corresponds to the chemical composition of the target. They deposit on a substrate that is generally heated to temperature for growing crystalline films.
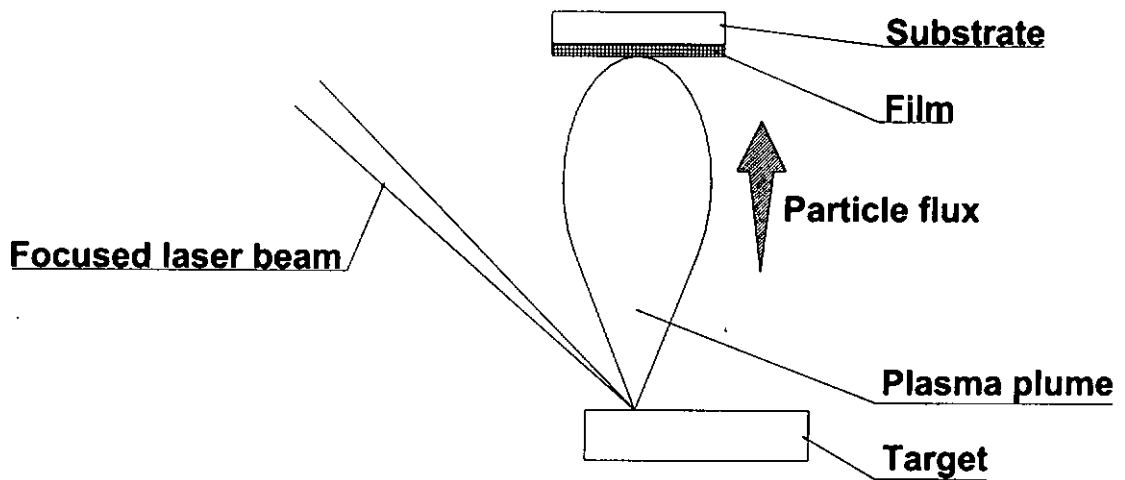
Figure 2.1 Schematic diagram of pulsed laser deposition of thin film.

2.2 Thin film growth mode

The growth of thin films can be categorized into three different modes [Greene, 1993] (see Fig. 2.2). Island (Volmer-Weber) growth results in the formation of isolated islands on the surface. This occurs when the cohesive energy of the atoms within the film is greater than the cohesive energy between the film and atoms on the surface. Layer-by-Layer (Frank-Van der Merwe) growth involves a deposition of one monolayer at the time and results in a very smooth epitaxial film. It occurs when the cohesive energy between the film and the surface atoms is greater than the cohesive energy of the film atoms. The cohesive energy will decrease monotonically as each film layer is added. Mixed growth mode (Stranski-Krastanov) involving growth of islands after the first monolayer has been formed successfully. This occurs

when the monotonic decrease in binding energy is energetically over-ridden by other

factors such as strain due to lattice mismatch, with the result that island formation

becomes more favorable. PLD is known to have very high deposition rate. The

process therefore favors Frank-Van der Merwe mode growth.

Volmer-Weber mode

Frank-Van der Merwe mode

Strankski-Krastanov mode
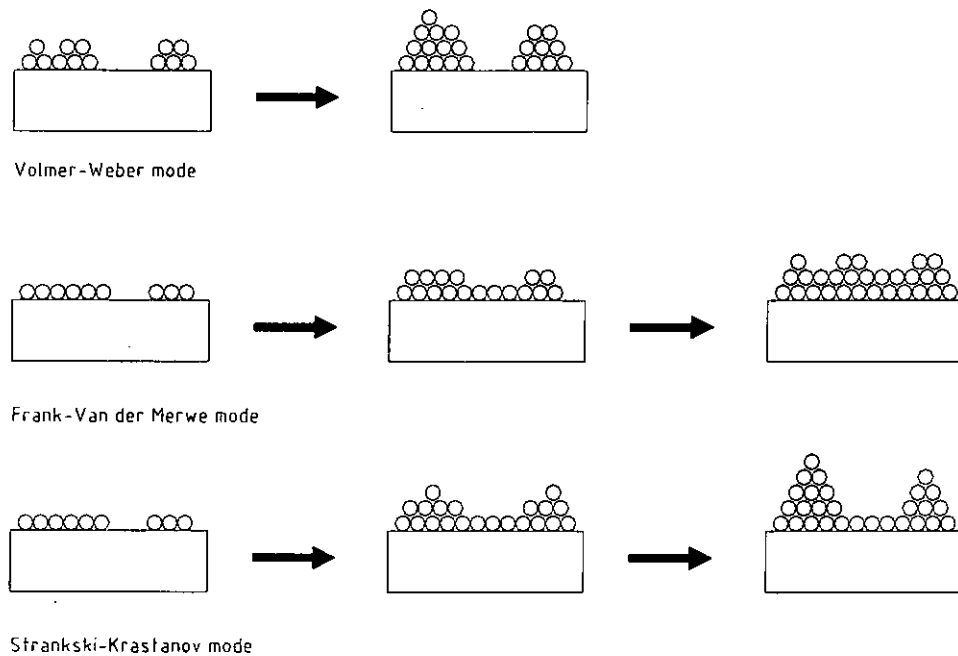
Figure 2.2 The common modes of film growth (i) Island (Volmer – Weber) mode, (ii) Layer-by-Layer (Frank-Van der Merwe) mode and (iii) Mixed (Stranski- Krastranov) mode.

2.3 Epitaxial growth

"Epitaxy" is in fact derived from the Greek-term meaning "order upon". In epitaxial growth of thin film, the crystal structure of the substrate serves as a template for the arrangement of the atoms in the growing layer. Many layers can be stacked on top of each other to form multilayered samples with atomically sharp junctions, and all of the grown layers adopt a definite crystalline relationship to the substrate. In order to verify the quality of the crystalline structure of films, it is essential to consider several important factors.

A primary consideration in forming epitaxial layers on any type of substrate is the chemical reaction. To illustrate this point we may take, for example, epitaxial growth of metal oxides on silicon. It is essential to oxidize the metal species rather than the silicon substrate, since the formation of even a thin amorphous silicon oxide layer before the establishment of epitaxy would prevent epitaxy altogether.

A secondary consideration is the structural similarity of the deposited layer and the substrate. Since the materials of the films and the substrate may not be the same, their crystal structure and lattice parameter are normally different. The difference in lattice parameter between the film and the substrate is called "lattice mismatch". The lattice mismatch (f) is defined as:

$$f = \frac{\left|a_s - a_f\right|}{a_s}$$

where a_s and a_f are the lattice constant for substrate and film, respectively.

In the conventional approach, the lattice mismatch should be small enough so that there is a smooth transition in atomic arrangement from one material to another. Otherwise, the bonding between atoms across the interface of the components will be irregular and weak. As a result, the films can peel off, crack, or contain a large density of crystalline defects.

Another consideration in forming an epitaxial film on a substrate is their compatibility in thermal expansion coefficient. The total strain in the film is a combination of multiple sources such as the intrinsic strain incurred during growth, transformation strain, and strain induced by the mismatch in thermal expansion coefficient. Frequently, the latter effect dominates; the stress built up in the film can be defined as:

$$\sigma_{th} = \frac{E_f}{1-v_f}\varepsilon_{th} = \frac{E_f}{1-v_f}\int_{T_o}^{T}(\alpha_f - \alpha_s)dT$$

where E_f is the film Young's modulus, ε_{th} is the thermal strain, v_f is the Poisson ratio, α is the thermal expansion coefficient and T represents the temperature.

When the thermal strains exceed the elastic limit of the film, they are relaxed by various mechanisms such as dislocation glide. As the relaxation processes are inherently accompanied by simultaneous changes of the film morphology they are often detrimental for the stability and performance of thin-film devices, which are not operated at their deposition temperature.

In this project, in order to select the appropriate materials used for the substrate layer, the buffer layer and the electrode for MnO thin films, we need to consider the relevant parameters of materials. Some important data of materials involved in this project are summarized into Table 2.1.

Material	*Structure*	*Lattice constant (nm)*	*Lattice mismatch to MnO (%)*	*Temperature expansion coefficient (TCE) $(x\ 10^{-6}\ K^{-1})$*	*TCE mismatch to MnO (%)*	*Melting point ($^\circ$C)*	*Nature*	*Resistivity (Ω cm)*
MnO	Rocksalt	0.444	--	11.0	--	1650	Insulator	$> 10^{9}$
CoO	Rocksalt	0.426	-4.05	15.0	36.36	1935	Insulator	$> 10^{8}$
MgO	Rocksalt	0.420	-5.41	10.8	-1.818	2800	Insulator	$> 10^{14}$
TiN	Rocksalt	0.424	-4.50	9.4	-14.55	3290	Metallic	1.5×10^{-5}
Si	FCC	0.547	23.20	4.2	-62.27	1414	Semiconductor	10
Platinum	FCC	0.392	-11.72	8.9	-19.09	1768	Metal	1.06×10^{-5}
Gold	FCC	0.407	-8.33	14.4	30.90	1064	Metal	2.2×10^{-6}

Table 2.1 Information of the materials used in the MnO thin film study.

2.4 Some fundamental parameters for thin film deposition

The quality of the as-grown films is very sensitive to some physical parameters such as the substrate temperature, the kinetic energy of the deposition flux and the deposition rate. Effects from background gas are also critical in some cases.

2.4.1 Substrate temperature

In the initial stages of the film growth the flux deposited on the substrate might re-evaporate from the surface, nucleate into a cluster, be consumed by existing clusters or be trapped on a surface defect site. All these processes are dependent upon the mobility of the deposited atom on the surface. Natural high mobility occurs at high substrate temperatures.

The microstructure of the deposited films is very often determined by the substrate temperature. Also it is well known that the closer the substrate temperature to the melting temperature of the film, the more film relaxation channels are energetically accessible. Hence, the substrate temperature can be used as a processing parameter to induce different structures.

2.4.2 Energy of the deposition flux

Growing films from species impinging at higher kinetic energies generally improves the film quality [Mattox, 1963]. The effects of high kinetic energy ion bombardment of the substrate include ballistic collision, ion mixing and thermally simulated exchange mixing. These effects help to raise the substrate temperature which in turn governs the film properties like film stress and crystal structure. An important manifestation of depositing high incident kinetic energy species is that quality crystalline films can be obtained at a much lower substrate temperature.

2.4.3 Deposition Rate

The deposition rate can vary over a wide range and is strongly dependent on the nature of the materials to be deposited. It has to be considered on a case by case basis. The influence of the deposition rate on the grown films is complicated. However, there are some useful guidelines to follow. Too high a deposition rate causes film deterioration because of the reduced opportunity for film relaxation. Too small a deposition rate, on the other hand, demands high vacuum. The lower the deposition rate, the more chance the film will incorporate unwanted gaseous impurities. In addition, the deposition rate needs to be higher than the desorption rate in order to lay a material layer.

2.4.4 Vacuum quality and background gas

Two additional effects arise as the result of introducing background gas, namely, chemical reaction and non-reactive thermal collision between the energetic flux and the background gas. Using high kinetic energy deposition fluxes in a background gas can induce gas phase reactions, which might compensate for some loss of a constituent element such as oxygen or nitrogen in the oxide and nitride films, respectively. Numerous such examples are found in PLD. A representative example is the formation of YO from the ablation of Y into O_2 [Lynds et al., 1989; Girault et al., 1989].

Introduction of a background gas is not universally advantageous to all deposition techniques. The kinetic energy and angular distribution of the ablated fluxes can be controlled by the introduction of a background gas. In general, high background gas pressure reduces the kinetic energy of the ablated species. The deposition fluxes are confined in the forwarding direction. As a result, the deposition yield is much higher in the central direction. However, the uniformity of the deposited film thickness is limited to a small region normal to the target surface. Also, the vapor species can undergo enough collisions that nucleation and growth can occur to form particulate before their arrival at the substrate. On the contrary, lower ambient pressure or vacuum produces a uniform film of much bigger area, at the expenses of reduced deposition yield.

2.5 PLD setup

A KrF excimer laser emitting radiation of 248 nm wavelength was used in the present PLD studies. The PLD system (see Fig. 2.3) consisted of a vacuum chamber which was evacuated by a diffusion pump to a base pressure of 8×10^{-6} Torr. Pressure of the chamber was monitored by ionization gauge (ULVAC 122A). Ablation targets of 20 mm diameter were affixed, via a target mount, onto the tip of a rotation axle with 5 RPM rotating speed. The windows of the chamber and the focusing lens were made of UV-grade fused silica that transmits over 90 % of the excimer laser. The laser beam was directed to irradiate the flat surface of the rotating target at an angle of 45°. Laser pulse of energy of 200 mJ was focused to a spot size such that energy density is maintained at 5 J cm^{-2}. The substrates were adhered to the front of the substrate holder/ heater placed at 5 cm away the target.
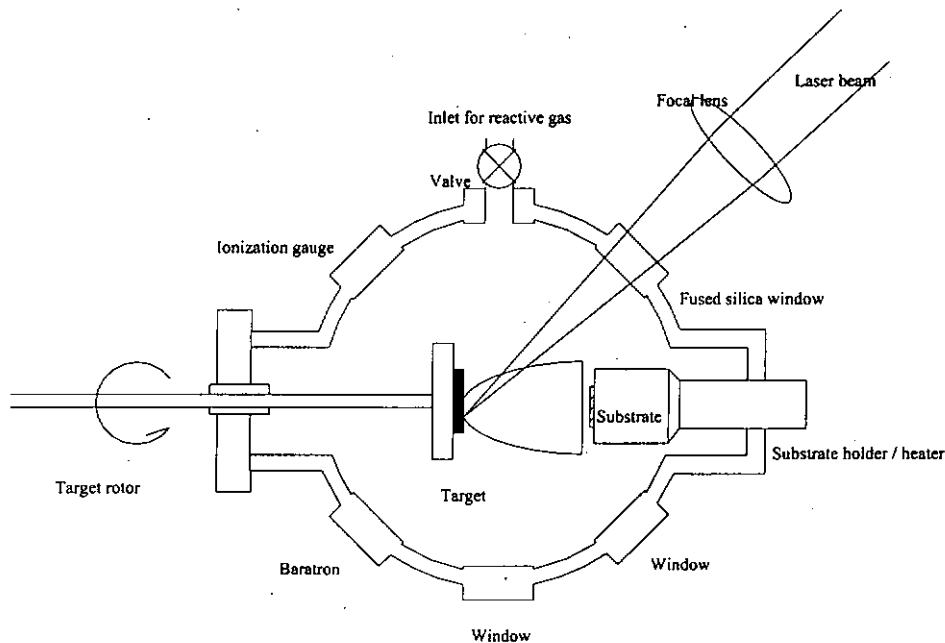
Figure 2.3 The schematic diagram of the pulsed laser deposition setup.

Growth of crystalline films requires careful control of the substrate temperature during film deposition. We have used a homemade 4 cm diameter substrate holder which provides stable temperature that can vary from room temperature to 800 °C. It utilizes halogen quartz lamps (150 W maximum output) enclosed in a cylindrical shaped stainless steel case as the heating element. The temperature of the substrate holder is determined by a type K thermocouple (Nickel-Chromium, Nickel-Aluminum). Heating rate is controlled by a programmable regulator (PAC15-0321E). The substrate holder can operate in UHV conditions as well as in oxygen ambience. The substrate is mounted on the faceplate of substrate holder with high temperature silver paste (G3691). The high thermal conductivity of silver paste can provide a uniform temperature distribution in the substrate and ensure the substrate temperature to be as close to the measured value by the thermocouple as possible.

2.6 Advantage and disadvantage of PLD

The advantage of PLD method over other deposition techniques such as molecular beam epitaxy and metallorganic vapor phase epitaxy includes the unique capability of transferring any source materials to the surface of a substrate. Its pulsed nature which affords high controllability of the deposition thickness, plus the potential of synchronizing the high flux/ short duration pulses with pulsed reactive gas sources makes PLD a desirable film growth technique. The high kinetic energy of the ablation plume which promotes surface mobility adatoms on the grown films helps in crystallization and improving the structural quality.

With respect to other processes such as chemical-vapor deposition or ion beam sputtering, PLD allows for easy handling since the laser source is placed outside the reaction chamber. Furthermore, the emission of energetic ions during laser-target-vapor interaction has an important influence on the layer formation, i.e. it enables growth of adherent and epitaxial films at lower substrate temperature than other methods. A lower deposition temperature reduces the undesirable substrate interdiffusion processes, thermally induced internal stress and the re-evaporation of volatile components. This is especially important for the deposition on impurity doped compound and complex materials having low melting point components.

Comparing with some other film deposition techniques, the vacuum condition of PLD is less stringent and can be achieved by a relatively economical pumping system. It enables us to fabricate films in high partial pressures of reactive gas, such as oxygen. It is crucial to maintain the proper oxygen content in the film during deposition of many oxides. Also, the presence of reactive gas can bind volatile species to the substrate, preserving the film stoichiometry. PLD has a distinct advantage over sputtering in that it does not require a constant glow discharge which can limit independent control of process parameters.

There are certain drawbacks in PLD. One limitation of PLD at the present time is that, as a relatively new film growth process, issues related to industrial scale-up have yet to be demonstrated. In particular, deposition of films on large-area substrates may be difficult. In addition, the presence of particulate is an intrinsic problem adhered to PLD. The undesirable particulates with a diameter of 1-10 μm are mainly produced by splashing effect. They induce defects and inhibit the formation of atomic flat film surface. These are detrimental to device fabrication in microelectronic applications.

CHAPTER 3

Characterization method

3.1 Introduction

It has been realized that the properties of the thin films are extremely sensitive to structural imperfection. Therefore, it is highly desirable to be able to grow epitaxial films with near single crystal quality. In this connection, full characterization of the PLD grown MnO films is needed to gain better understanding of the film grown process.

In this study, the deposited MnO films have been characterized using several techniques to yield information on their structural and electrical properties. The crystalline structures of the deposited films were examined by X-ray diffractometer (XRD) using CuKα radiation. Surface morphology of films was studied by scanning electron microscopy (SEM). The electrical conduction properties were measured by a high input impedance digital electrometer. The dielectric measurement was achieved by an impedance analyzer. The details of the experimental setups and the characterization techniques are discussed the following sections in this chapter.

3.2 Structural characterization

3.2.1 Surface profiling

Thin film properties usually depend on thickness, so the thickness measurement is among the first few quoted attributes of its nature. Especially in microelectronic applications, it generally requires the maintenance of precise and reproducible film metrology. Various types of thin film thickness measurement have been well developed. Surface profiler is one of the convenient techniques which has been categorized as a mechanical method.

Style ▬▶ Scan direction

Step

Film

Substrate
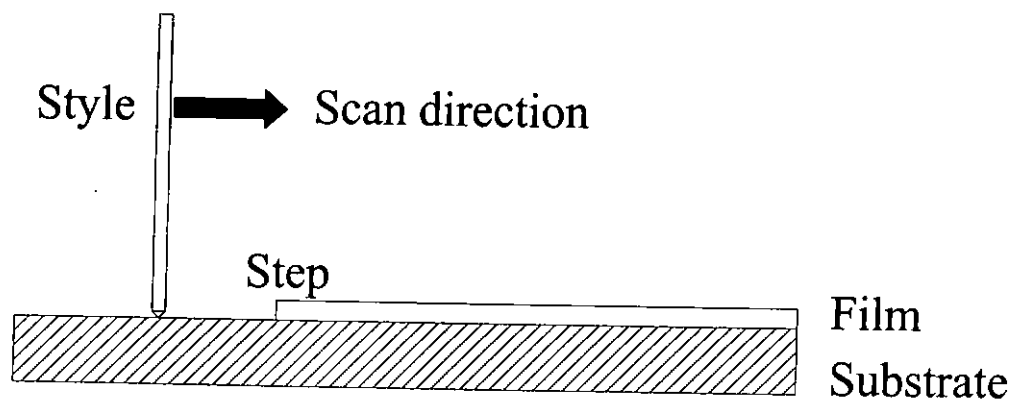
Figure 3.1 Schematic diagram of surface profiler.

The thickness of our PLD films was determined from the surface profiler machine (Alpha step profiler –Tencor Instrument, model P-10). The profiler is composed of electromagnetical sensor that detected the mechanical movement of a stylus as it traces the topography of a film-substrate step – an operation similar to phonograph needle on the track of a record (see Fig. 3.1). The vertical stylus movement is digitized and data can be processed to magnify areas of interest and yield best-profile fits. A step was made by partial masking of the substrate during the deposition process. Film thickness was directly read out as the height of the resulting step-contour trace. A precise measurement of film thickness can be determined due to the vertically height resolution of the alpha step profiler can be as small as 1nm. It should be noted that the accuracy of the profiler measurement may suffer due to:

1.Stylus penetration and scratching of soft films.

2.Excessive noise generated from the surface roughness

3.Vibration of the equipment

3.2.2 X-ray diffractometry

The texture can strongly affect the properties and behavior of materials. Tensor properties of bulk and thin film such as dielectric constant, piezoelectric constants, elastic coefficients and electro-optic coefficient are especially dependent on texture. Indeed, many thin films and bulk materials used in electronic applications have been fabricated to carry preferred crystallographic orientation, or texture. Various analytical methods have been used to fulfill the requirement for the accurate texture characterization. Among them, X-ray diffraction (XRD) is a well-developed and widely used technique.

Conventional XRD methods (Bragg Brentano, grazing incidence) can provide information regarding crystallinity, phase identification, and qualitative assessment of planar orientation. Our XRD instrument (Philips X'pert system) is composed of an X-ray source, giving out K_α radiation of Cu at wavelength of 0.154 nm. The K_β emission was filtered by Ni filter. The crystalline structure of our PLD grown thin films was characterized by XRD operating in four-circle mode.

Now consider an X-ray beam incident on a single crystal, a small fraction of the incident beam will be scattered by the regular arrangement of atoms. To simplify the case, the crystal was treated as a pair of parallel planes, P1 and P2, separated by an interplanar spacing d.
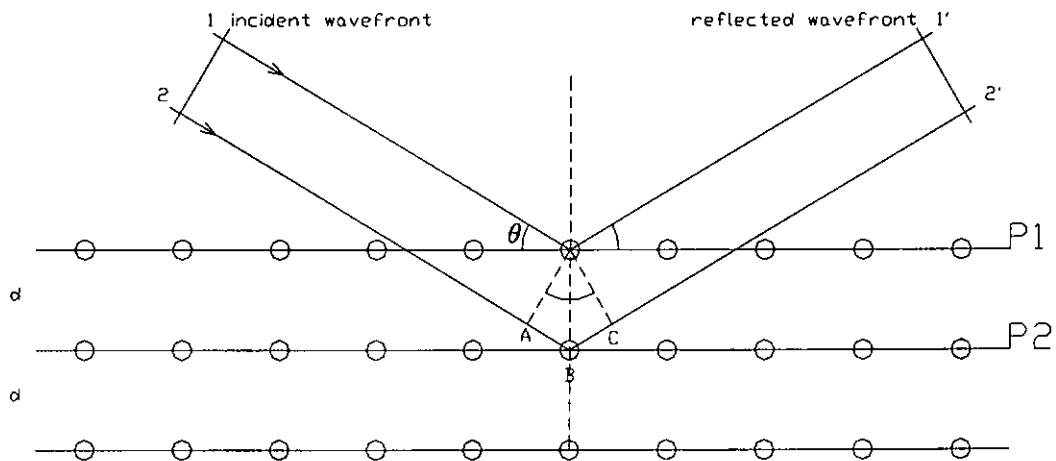
Figure 3.2 Bragg diffraction of X-rays from successive planes of atoms. Constructive interference occurs for ABC equal to an integral number of wavelengths.

In Fig. 3.2, the two parallel incident rays 1 and 2 make an angle θ with these planes. A reflected beam of maximum intensity will results if the waves represented by 1' and 2' are in phase. The path difference between 1 to 1' and 2 to 2' (AB+BC) must be an integral number of wavelengths λ to satisfy the constructive interference. Then we can express this relationship mathematically in Bragg's law:

AB + BC   =   **2 d sin θ = n λ,** ·   where n = 1, 2, 3...

The interplanar spacing d, the distance between adjacent planes in the set (h k l) of a material with a cubic structure and lattice parameter a, can be obtained from the equation:

$$\frac{1}{d^2} = \frac{h^2 + k^2 + l^2}{a^2}$$

Combined this two equations, we yield:

$$\frac{1}{d^2} = \frac{h^2 + k^2 + l^2}{a^2} = \frac{4\sin^2\theta}{n^2\lambda^2}$$

So, $2d\sin\theta = \lambda$
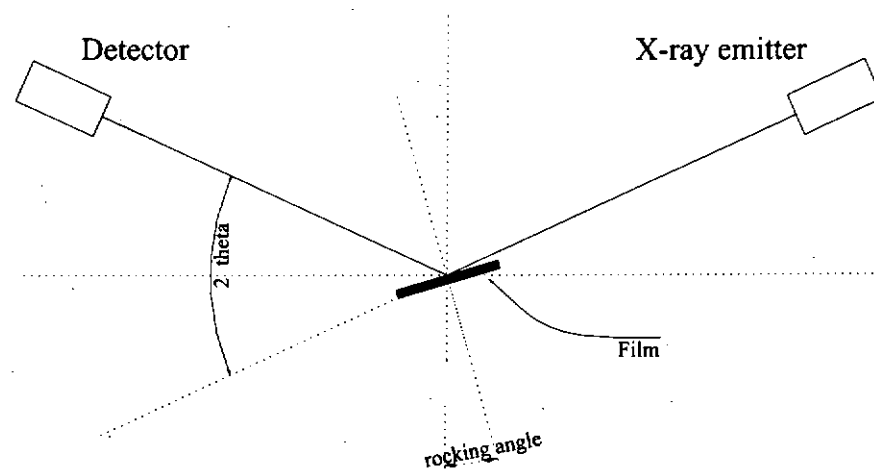
Figure 3.3 The schematic diagram shows the operation of XRD ω-scan.

Even the best crystalline film grown by pulsed laser deposition is not really a perfect single crystal. In fact, it is composed of some mosaic crystal components which have some spread of orientation. The distribution of size and tilts of the components in a layer will exhibit itself as an extended angle of scattering. As we scanned across ω while the detector was held fixed at 2θ, a full width at half maximum (FWHM) of the scan profile can be determined (see Fig. 3.3). We call this profile a rocking curve. This FWHM reflects the degree of the orientation of the thin films. It shows a smaller value when the sample has a better alignment. A film can be considered as highly oriented if the FWHM of the rocking curve is less than 1°.
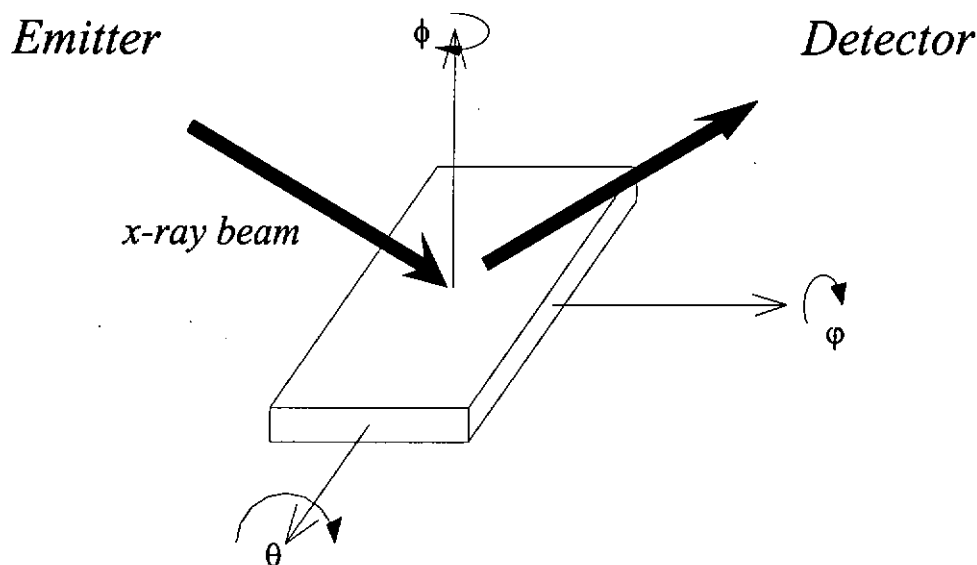
Figure 3.4 The rotation axes of the sample relative to the X-ray emitter and detector.

When thin films are deposited on single-crystal substrates, in-plane crystallite alignment is an important microstructural property. If the thin film in-plane alignment matches the single crystallographic direction of the substrate, it is said to be epitaxially grown.

To evaluate the in-plane alignment of these thin films relative to the substrate, $360°$ Φ-scan is utilized. XRD studies of crystalline thin films depend on the crystal symmetry, lattice constants, and planar orientation of the crystal phase. For a simple cubic structure with (001) normal plane, $360°$ Φ-scan is done by setting $\varphi = 45°$ and fixing θ and 2θ angles corresponding to the (202) substrates (see Fig. 3.4 and Fig. 3.5a). For good epitaxial cubic structure films, four characteristic peaks separated by $90°$ are observed in the $360°$ Φ-scan. They correspond to the (202) family of reflection planes and should coincide with those of the substrates.

(a)   (b)
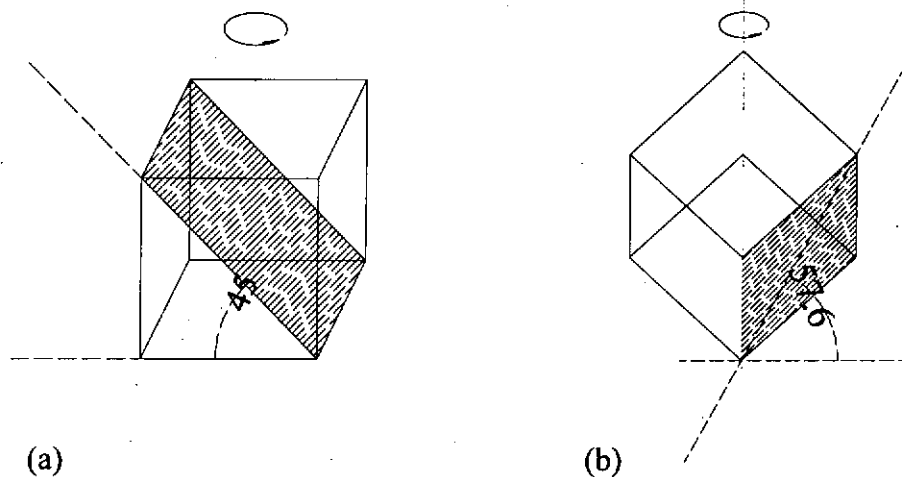
Figure 3.5 The illustrations of tilt angle and the reflecting plane in Φ-scan of (a) 4-folded symmetry along [100]-axis, (b) 3-folded symmetry along [111] axis.

But for a simple cubic structure sample with (111) normal plane, we need to set $\phi = 57.6°$, and the θ and 2θ angle is tuned to angles corresponding to the (200) diffraction (see Fig. 3.5b). In this case three characteristic peaks separated by 120° are observed which corresponding to the (200), (020) and (002) planes, respectively [Blanton et al., 1996].

At the same time, powder XRD method is used to study polycrystalline materials. After the sintering process, PLD targets normally are composed of tightly packed fine grains of single crystalline materials. The term 'powder' really means that the crystalline domains are randomly oriented in the sample. Therefore, when the 2D diffraction pattern is recorded, it shows concentric rings of scattering peaks corresponding to various d spaces in the crystal lattice. The positions and the intensities of the peaks are used for identifying the underlying structure (or phase) of the material. It can be done by comparison of experimental data with standard data in crystallographic databases, such as Powder Diffraction File (PDF).

3.2.3 Scanning Electron Microscopy

Scanning electron microscopy (SEM) is a high-resolution imaging technique. It provides remarkable analytical versatility and a wide magnification range from tens to hundred thousands. It can provide morphology and structural information in plan view or cross section view of the specimen.

In SEM, a focused beam of high-energy electrons is scanned over the surface of specimen. The electron beam interacts with the material causing a variety of signals. It includes secondary electrons, backscattered electrons, x-ray etc., each of which may be used to characterize a material with respect to specific properties.

The high-energy incident electrons interact with the loosely bound conduction band electrons in the sample. The amount of energy given to these secondary electrons as a result of the interactions is small. Because of this, only those secondary electrons that are produced within a very short distance of the surface are able to escape from the sample. This means that this detection mode boasts high-resolution topographical images, making this the most widely used of the SEM modes.

When an electron from the beam encounters a nucleus in the sample, the resultant Columbic attraction results in the deflection of the electron's path, known as Rutherford elastic scattering. A few of these electrons will be completely backscattered, re-emerging from the incident surface of the sample. Since the scattering angle is strongly dependent on the atomic number of the nucleus involved,

the primary electrons arriving at a given detector position can be used to yield images containing both topological and compositional information.

Another possible way in which a beam electron can interact with an atom is by the ionization of an inner shell electron. The resultant vacancy is filled by an outer electron, which can release its energy either via an Auger electron or (more importantly here) by emitting an X-ray. This produces characteristic lines in the X-ray spectrum corresponding to the electronic transitions involved. Since these lines are specific to a given element, the composition of the material can be deduced. This can be used to provide quantitative information about the elements present at a given point on the sample, or alternatively it is possible to map the abundance of a particular element as a function of position.

Not all the specimen can be analyzed by SEM directly, non-conducting material is an example. For the non-conducting sample like our manganese oxide films, a negative charge builds up gradually from bombardment by the high-energy electron beam. An abnormal contrast and splitting of the image result from the uneven distribution of the negative charge on the sample. Most common solution is to coat a very thin (generally 10-20 nm thick) gold layer on the sample's surface. It can enhance the emission of secondary and backscattered electron, reduction of thermal damages as well as the elimination of charging effect.

3.3 Electrical measurement

3.3.1 Temperature dependent resistivity

The resistivity of MnO sample varies by six orders of magnitude over the temperature range from 77 K to 500 K. The measurement was taken by placing two electrodes on the surface of the test sample. Potential difference was applied between the two electrodes and the resulting current was measured. To keep the resistance below 200 $G\Omega$ which is the range of the electrometer (Advantest TR8652) used for the measurement, the samples were modified by an active area of 8 mm by 100 μm. This narrow gap was made by stretching a 100 μm diameter metal wire across the sample, and using it as a mask for the platinum deposition (see Fig. 3.6).
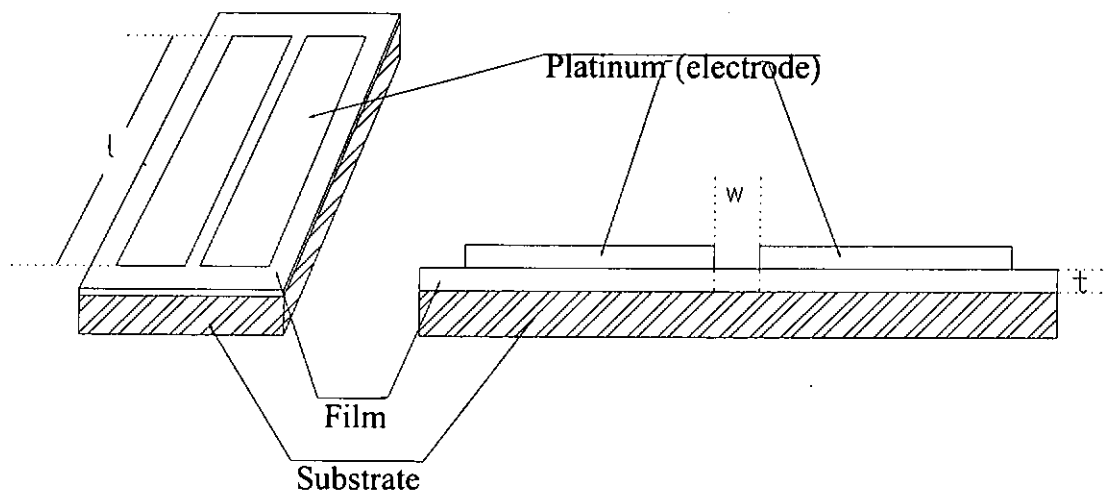
Figure 3.6 Sketch of the heterostructure for DC conduction measurement.

The samples were then mounted on a cold finger in a cryostat. After pouring liquid nitrogen into the cryostat and reaching 77 K, the sample temperature was programmed with a digital temperature controller. Resistance versus temperature data was taken on warming to 500 K over 5 hours period by an automated data acquisition system. The data was taken in a step of 0.5 °C. The measured resistance (R) is converted to resistivity (ρ) by knowing the film thickness and the active area involved. The value of resistivity (ρ) in unit of Ω cm, was calculated by the relation: $\rho = \dfrac{Rlt}{w}$, where l, t and w are as defined in Fig. 3.6.

A stable test environment is essential when making accurate resistivity measurements of a semiconductor. For example, humidity, temperature fluctuation and electromagnetic induction (EMI) can make the results erroneous. Some materials are excellent light detectors too. Consequently, the sample must be kept clean and free of contamination and tested in a light-free environment.

3.3.2 Leakage current measurement

Current-voltage curve of insulating thin film often reveals current leakage mechanism. In general, the leakage current through a metal-insulator-metal system is determined by the bulk of the films and by the electrode interface. In order to measure this electrical properties of the film, 0.2 mm diameter Pt top electrodes were deposited (see Fig. 3.7). The leakage current against voltage was measured by the digital electrometer (Advantest TR8652). By connecting the two terminals of the electrometer across the top and bottom electrodes of the dielectric layer and raising the driving voltage gradually, the leakage current against voltage curve can be obtained.
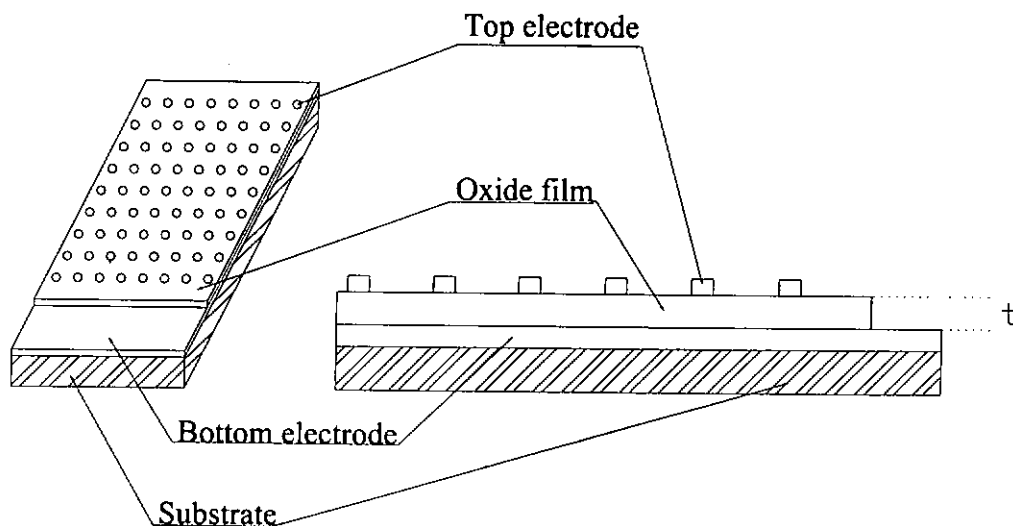
Figure 3.7 Sketch of the heterostructure used for dielectric measurement.

3.3.3 Dielectric measurement

The dielectric properties of the thin film were measured by a HP-4194A impedance analyzer. The dielectric samples can be considered as a capacitance, C_x connected in parallel with a resistance, R_x, where C_x represents the samples ability to store charge and R_x represent its heat loss. These values, C_x and R_x, could be measured using the impedance analyzer and related to the dielectric properties of the sample as

$$\varepsilon' = \frac{C_x d}{A \varepsilon_0}$$

$$\varepsilon'' = \frac{1}{R_x C_x \omega}$$

and $\quad \tan \delta = \dfrac{\varepsilon''}{\varepsilon'}$
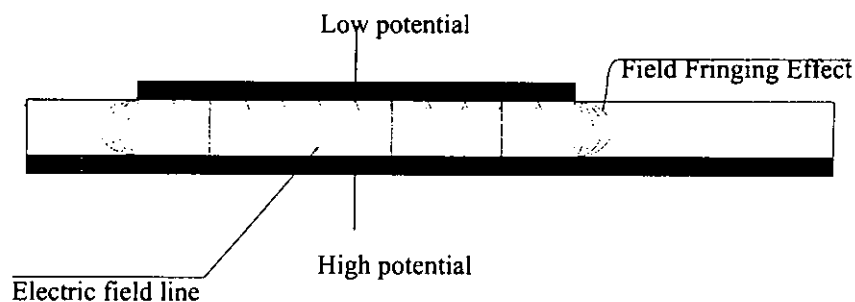
Figure 3.8 A cut-away view of the capacitor structure.

Our test samples had a thickness of about 250 nm and were coated with a top platinum electrode having a spot diameter of 0.2 mm. Due to a large aspect ratio of capacitor (area to thickness ratio) formed by the thin film, it can eliminate the erroneous results caused by fringing effect as shown in Fig. 3.8.

CHAPTER 4

Fabrication and characterization of MnO on TiN buffered silicon substrate

4.1 Introduction

During the last few years, there has been a growing interest in the growth mechanism of thin epitaxial metal oxide/ metal compounds which are becoming more and more important in micro- or nano-electronic devices. Surface and interface effects of transition metal oxide such as spin disorder are relevant to thin film magnetoelectronics devices like spin valves [Bodhisattva Das et al., 1998], spin transistors, or spin dependent tunneling devices – spintronics for short.

Among the transition metal oxide, manganese monoxide (MnO) is a very attractive oxide because of its d shell electronic configuration and strong magnetic properties. However, the surface science of MnO has not been widely explored due to the difficulties in obtaining a reliable method for preparing a clean and stoichiometric surface. Also MnO has been investigated over many years with respect to their electronic structure. In many cases, such investigations are based on experimental technique with very high surface sensitivities, for example, X-ray photoelectron spectroscopy. But the insulating properties of MnO often lead to a strong charging effect, which makes the interpretation of the data more difficult. The

deposition of the insulating MnO thin film on a metallic substrate is useful to avoid such problem [Rain et al., 1998]. Pure cubic MnO films epitaxially grown on Ag(111) [Muller et al., 2002] and MnO nanoparticle grown on Pt(111) [Rizzi et al., 2000] have been reported. However, epitaxial grown of MnO film on metallic layer integrated on silicon substrate has not been reported. In fact, epitaxial growth on semiconductor substrate, such as silicon, is crucial for potential technical applications.

In general metal-insulator-metal (MIM) capacitors are very valuable in many applications. They can be used in radio frequency (RF) circuits, in various configurations in analog ICs, and for decoupling capacitance in high power microprocessor unit (MPUs). In fact, MnO is a typical dielectric material. It is valuable for us to investigate these MnO thin film dielectric properties since no information on this aspect has been reported.

In this chapter, we focus on the epitaxial growth of MnO on TiN buffered silicon substrate by PLD method. The effect of some of the pulsed laser deposition parameters on the quality of the MnO films is investigated systematically. The characterizations of the deposited films in terms of substrate temperature and deposition oxygen pressure are presented. They are then correlated with their structural and dielectric properties.

4.2 Fabrication and characterization of TiN/Si

In order to obtain a good epitaxial film, selection of appropriate substrates plays an important role. TiN[001] and MnO[001] are both of rocksalt structure. The lattice parameters of MnO (0.444 nm) and TiN (0.424 nm) have a lattice mismatch of only 4 % and epitaxial growth is favorable. TiN thin films are widely used in electronic and mechanical industries due to their excellent properties such as high degree of hardness (~2500 kg mm^{-2} Vickers microhardness), high melting point (2930 °C), high electrical conductivity (15 $\mu\Omega$ cm) [Toth, L.E, 1971] and good diffusion barrier characteristics. For instant, TiN thin film is expected to be used as a barrier metal in Si industry that suppresses chemical interdiffusion during the fabrication process [Nicolet, M.A. 1978; Wittmer, M., 1984]. So the TiN buffer layer is not only providing a lattice-matched site for subsequent MnO film growth, but a good chemical diffusion barrier as well as a conducting electrode.

Despite the large lattice mismatch (28 %), epitaxial growth of the TiN(001) films on Si(001) does occur. The cube-on-cube growth can be described in terms of domain matching epitaxy [Narayan et al., 1993]. In the present case of TiN on Si, 5 interplanar distance of TiN matches with 4 interplanar distance of silicon, yielding a lattice mismatch of 4 % only. So, it is possible to prepare epitaxial TiN film on silicon with reasonable quality.

4.2.1 TiN target analyze

Commercial hot-pressed TiN target of 99.95% purity, bought from Electronic Space Products International Company (ESPI), was used in the present studies. The crystalline structure of the target was examined by XRD powder method. From the X-ray diffraction profile (see Fig. 4.1), it indicates that the TiN target is well crystallized and suitable for preparing thin films by PLD method. According to the extrapolation function shown in Fig. 4.2, the precise lattice constant of the TiN target was found to be 0.424 nm. This value agrees with a stoichiometric bulk of TiN. It will be used to compare with the out-of-plane lattice constant of the TiN film deposited by PLD.
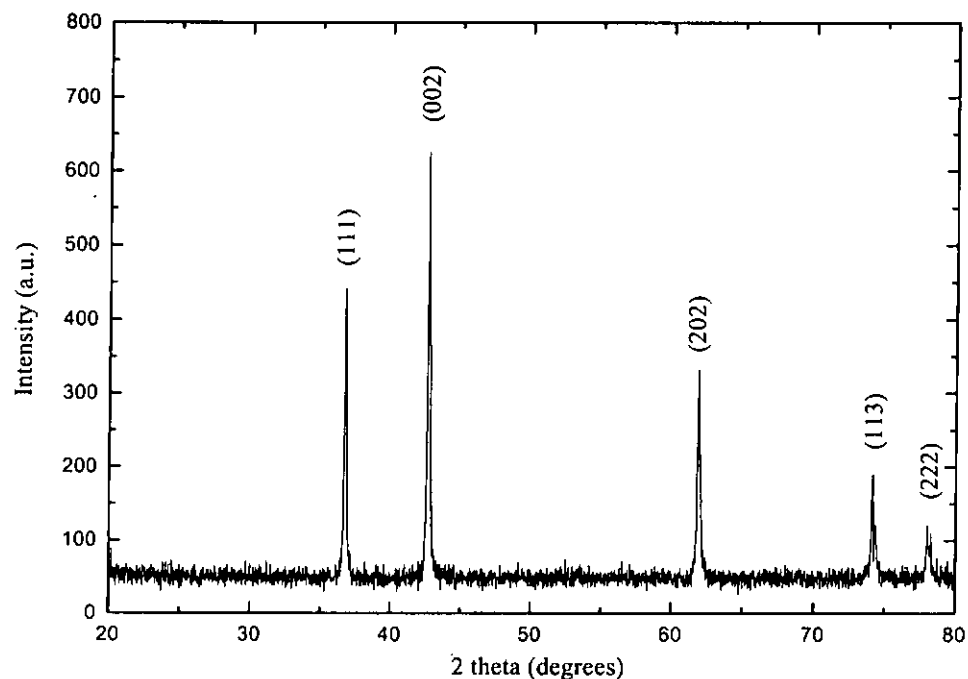
Figure 4.1 The XRD pattern of hot pressed TiN target.
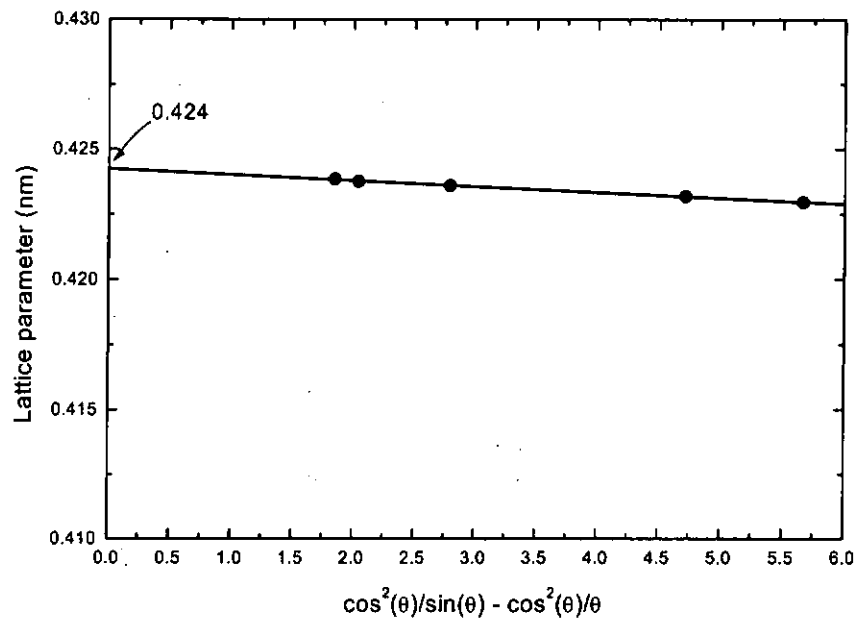
Figure 4.2 Extrapolation of the calculated lattice parameter of stoichiometric TiN target against $(\cos^2\theta)/(\sin\theta)-(\cos^2\theta)/\theta$.

4.2.2   Deposition of TiN layer

The TiN thin films were grown on Si(001) substrates using the high purity TiN target. The surfaces of the silicon were terminated with hydrogen by dipping them into a 10 % HF acid solution after ultrasonically cleaning in acetone. Then, the substrate was placed on the substrate holder at 5 cm from the target in the vacuum chamber. The substrate temperature during the growth was 650 °C. The chamber was evacuated to 2×10^{-5} Torr by a diffusion pump. The target was ablated by a KrF excimer with laser fluence of 5 J cm^{-2}. Uses of a low laser fluence and a long target-substrate distance are effective ways to reduce the formation of particulates on the film. In the present case the thin film growth rate was kept at about 0.1 nm s^{-1}. Film thickness was set to a constant (200 nm) by controlling the growth time. In order to

improve the crystallinity of the deposited films, subsequent annealing treatment was generally performed for 10 minutes at 650 °C substrate temperature.

4.2.3 Structural characterization of TiN/Si(001)

Excellent structural quality and sharp interface boundary of TiN/Si(001) are revealed by plan-view and cross-sectional electron microscopy analysis. From the surface morphology profile of the film shown in Fig. 4.5, an extremely clean and crack-free surface can be obtained. The smoothness of the TiN surface can be observed from this figure. Fig. 4.6 shows the SEM image of fractured cross-section of the film. According to this figure, a sharp interface boundary is clearly shown with wide columnar grains. The thickness of the TiN film is about 200 nm in the SEM image. This agrees well with the results from surface profiler.

In Fig. 4.3, the XRD pattern indicates a sharp peak at 43.09° corresponding to the TiN(002) orientation. It reveals that the TiN films are oriented with TiN(001) parallel to the Si(001) substrate. The out of plane lattice constant of TiN is 0.419 nm, which is slightly smaller than the normal relaxed value of 0.424 nm. It might be the results of the nitrogen deficient caused by the high vacuum deposition process. In Fig. 4.4, the FWHM from ω-scan rocking curve is about 1.83°. It suggests that well-oriented TiN films are formed on Si substrates. In summary, it has been demonstrated that TiN is successfully grown on Si(001) substrate with a good epitaxy crystalline structure.
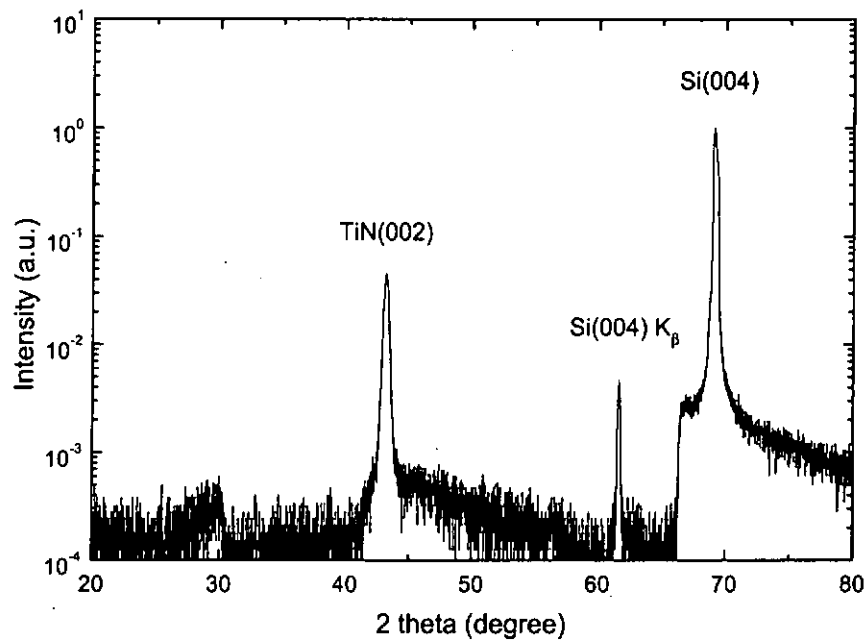
Figure 4.3 XRD pattern of a 200 nm thick TiN film deposited on Si(001) at 650 °C under a pressure of 2x10⁻⁵ Torr.
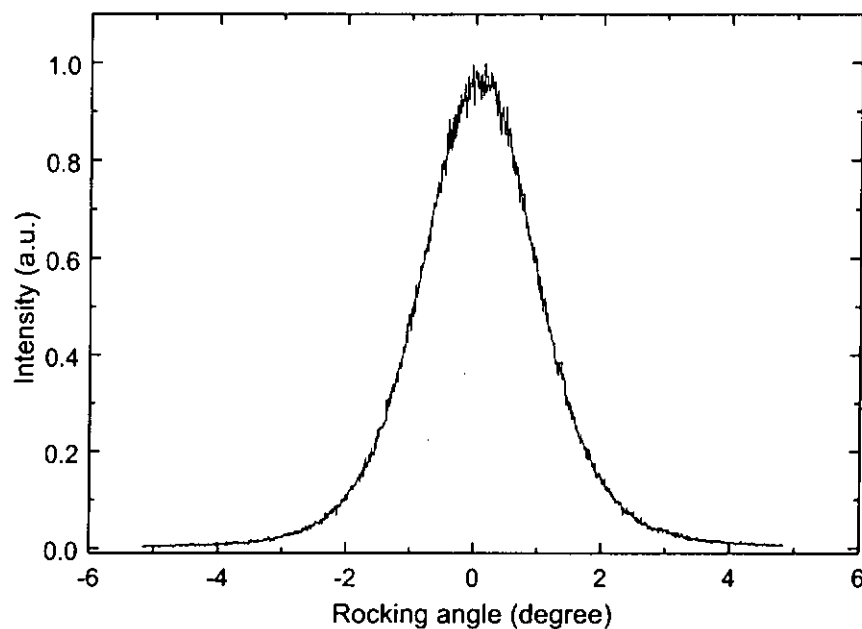
Figure 4.4 XRD rocking curve of TiN(002) peak exhibiting a FWHM of 1.83°.

```
EHT=20.00 kV          WD=   8 mm          Mag=100.00 K X
100nm  |—|             Photo No.=1707    Detector= SE1
```
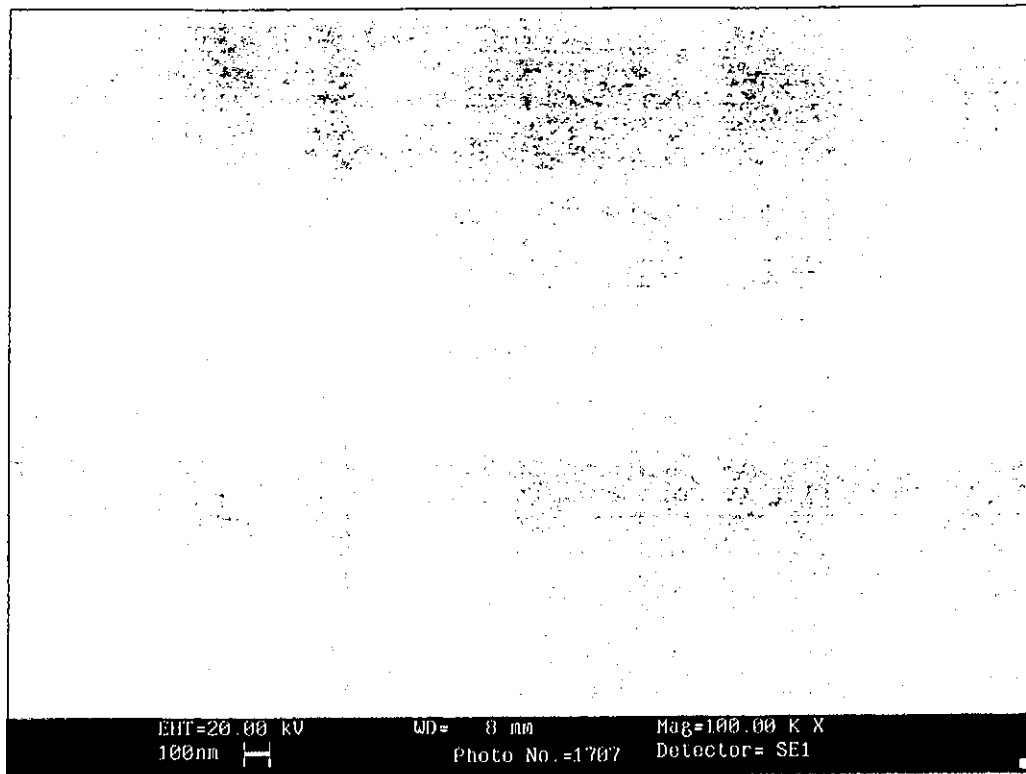
Figure 4.5 SEM image of surface morphology of TiN thin film shows a crack free surface.


```
TiN

Si

EHT=20.00 kV          WD=   7 mm          Mag=100.00 K X
100nm  |—|             Photo No.=1728    Detector= SE1
```
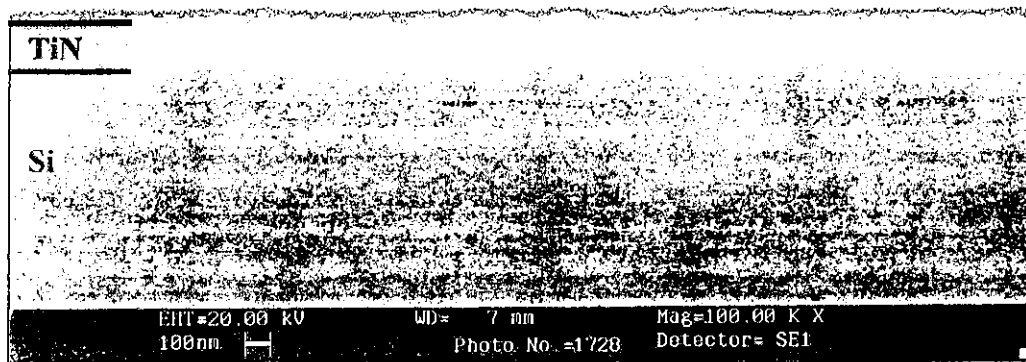
Figure 4.6 SEM cross sectional image shows 200 nm thick TiN film deposited on Si(001) substrate.

4.3 Fabrication of MnO/TiN/Si

4.3.1 Manganese oxide target fabrication and analyze

Manganese oxide target was fabricated by the standard solid-state reaction method. The target was obtained by decomposing high purity MnO_2 powder (99.99 %) at 900 °C for 5 hours. They were grounded into fine powder and compressed to pellet which was then sintered at 1100 °C for 15 hours.
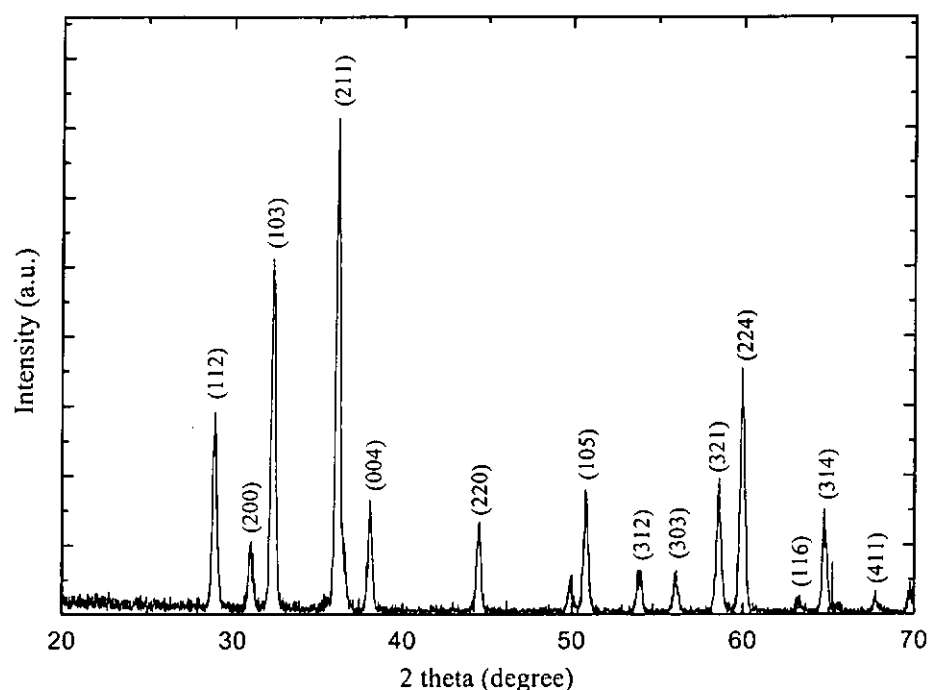
Figure 4.7 The powder XRD pattern of hot pressed manganese oxide target.

The XRD diffraction lines verify that manganese oxide target is a single phase Mn_3O_4. Such oxide is in spinel structure. The chemical formula can be represented by $A^{+2}B^{+3}_2O_4$ where A represents one or more divalent metals which form oxides of

the type AO (MnO) and B represents one or more trivalent metals that form oxides of the type B_2O_3 (Mn_2O_3).

In a spinel crystallographic structure shown in Fig. 4.8, each unit cell contains 32 oxygen ions (anions) forming a cubic close-packed structure. There are 64 tetrahedral interstices and 32 octahedral interstices; of these 8 tetrahedral and 16 octahedral interstices are occupied by the metal ions (cations). These cation sites are referred to as A- and B- sites respectively. The general formula of oxide compounds which possess the spinel structure is $A(B_2)O_4$ so that the unit cell contains eight formula units. A represents a cation tetrahedrally surrounded by four oxygen anions and B represents a cation octahedrally surrounded by six oxygen anions.
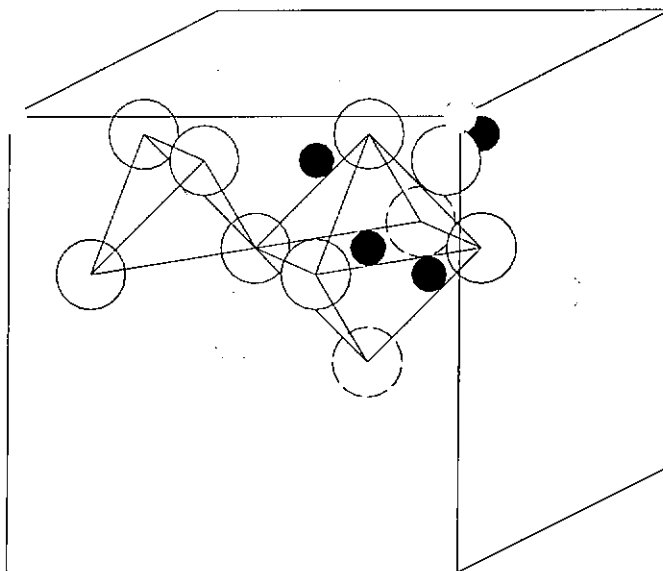
Figure 4.8 Arrangement of cations in the spinel lattice. Only two octants of the spinel structure are represented. The large spheres represent the oxygen ions. The small white and black spheres represent the cations on tetrahedral and octahedral sites, respectively.

For the growing of many oxide films, such as PZT and $LiMn_2O_4$, it is necessary to maintain an oxidizing environment during the deposition process in order to help to form and stabilize the desired crystal phase. However, some oxide such as rocksalt MnO is highly stable at high temperature. Indeed, MnO films can be fabricated by PLD in an oxygen free environment. Our manganese oxide target fabricated from the sintering process was verified by XRD to be Mn_3O_4 spinel. During the deposition process, the Mn_3O_4 was evaporated and dissociated into simpler species by the UV pulsed laser. Under a careful control of ambient pressure and substrate temperature, the excess of oxygen can escape from the laser plume. As a result, the deposited film can maintain a stoichiometric MnO formation.

4.3.2 Deposition of MnO on TiN buffered Si(100)

The MnO thin films were grown on TiN buffered Si(001) substrates by using the sintered Mn_3O_4 target. The preparation of TiN buffered Si(001) substrate has been mentioned in Section 4.2. Then, this TiN/Si substrate was placed on the substrate holder positioned at 5 cm away from the target in the vacuum chamber. The substrate temperature during the growth was set at 600 °C. The chamber was evacuated to 2×10^{-5} Torr using a diffusion pump. The target was ablated by a KrF excimer with laser fluence of 4 J cm^{-2}. No additional post-annealing was made.

4.3.3 Structural characterization of MnO/TiN/Si(001)

The MnO film was found to be 250 nm thick. The structure of the films was characterized by XRD. The XRD θ-2θ scan profile of MnO is shown in Fig. 4.9. Highly oriented single rocksalt phase of MnO film was observed. The lattice constant was found to be 0.441 nm, which was slightly smaller than the value in bulk sample (a=0.444 nm). The decrease in the lattice parameter suggests the possible presence of strain in the film. The out-of-plane orientation of the MnO(002) peak was examined by ω-scan. A good orientation of film was obtained because the FWHM of the rocking curve was only $0.61°$. The XRD Φ-scan of MnO(202), TiN(202) and Si(202) were performed to confirm epitaxial growth nature of the films. The results are shown in Fig. 4.11. The sets of four characteristic peaks of a cubic structure of the three layers show diffractions at the same Φ-angle. This suggests that the MnO films are cube-on-cube grown on the TiN buffered Si(001) substrate.
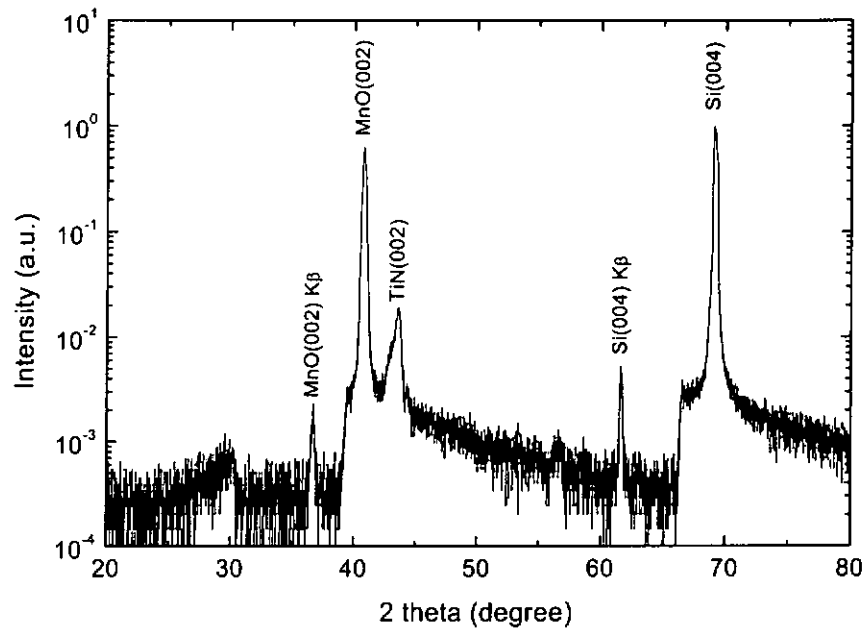
Figure 4.9 XRD pattern of the MnO/TiN/Si(001) heterostructure.
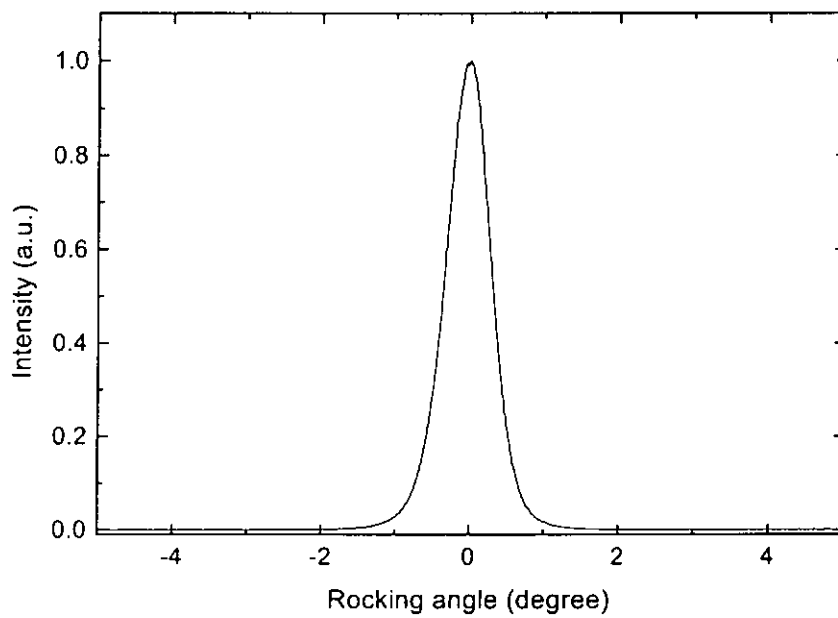
Figure 4.10 XRD rocking curve of MnO(002) showing a FWHM of 0.61°.
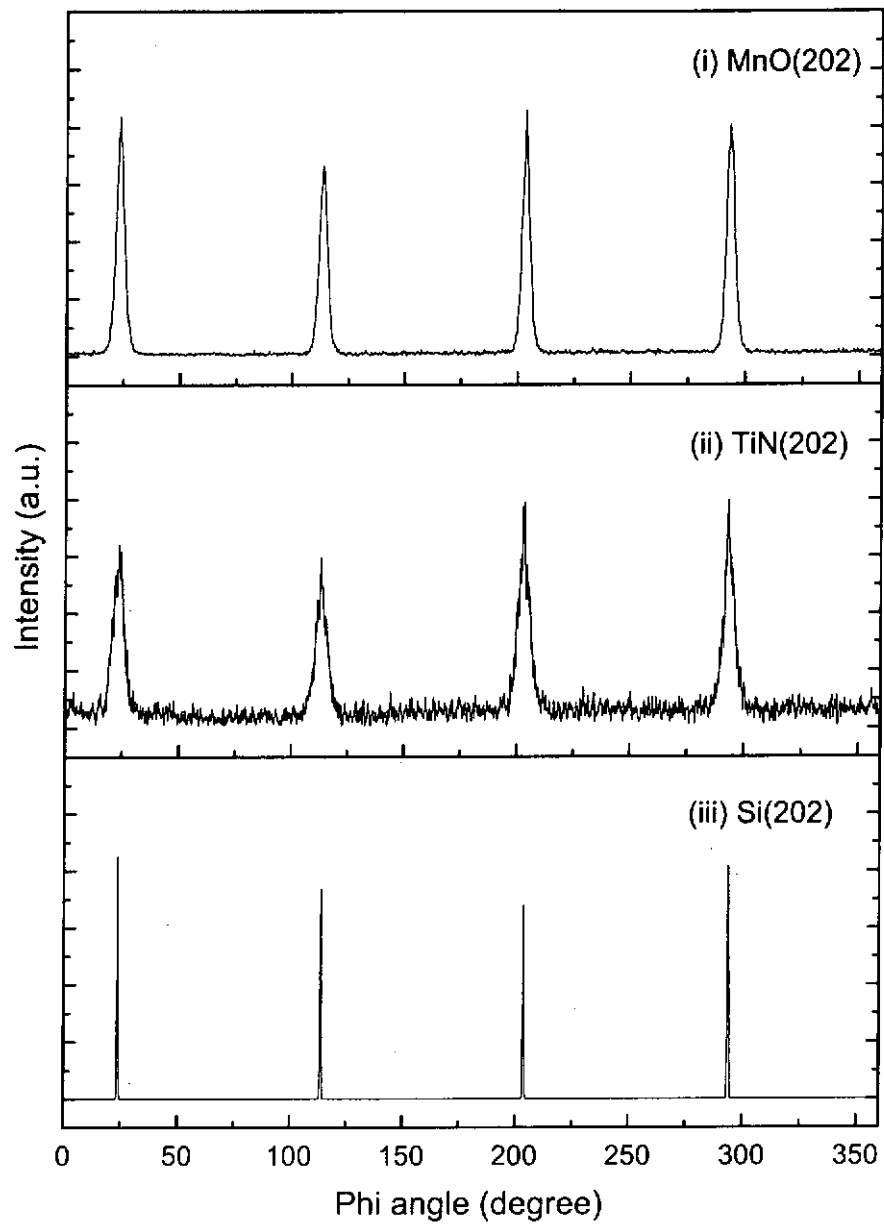
Figure 4.11 The Φ-scan of the (i) MnO(202), (ii) TiN(202) and (iii) Si(202).

4.4 Optimization of deposition condition

There are a few parameters that can be varied in PLD: the substrate temperature T_s, the ambient pressure, the target–substrate distance and the laser fluence. Among them, the substrate temperature and the ambient pressure are the most important parameters in the control of the structure and quality of PLD-produced films. In the following experimental investigations, the deposition pressure and substrate temperature were varied systematically.

4.4.1 Substrate temperature dependence

This set of experiment was performed with a base pressure of 2×10^{-5} Torr. Apart from the substrate temperature, all the other parameters were the same as mentioned in the pervious section. The manganese oxide layers were prepared in this series of experiments at substrate temperatures varying from 200 °C to 800 °C.

The structure of the films was characterized by XRD and SEM. The XRD profiles of the MnO films grown on TiN/Si substrates at different temperatures are shown in Fig. 4.12. For films prepared at 200 °C, a weak and broad peak is observed at 40.33°, corresponding to diffraction from MnO(002) plane. It also means that the MnO films start to crystallize at this low substrate temperature. The residue impurity phase of Mn_3O_4 is seen in sample deposited at 300 °C. In the range of 400 °C to 700 °C, only single phase of MnO is observed.

When the substrate temperature is increased to 800 °C, an additional peak at 42.1° is observed. This peak originates from the presence of $TiSi_2$. At high temperature $TiSi_2$ is formed at the interface between the Ti-rich of TiN layer and silicon substrate [Fujimura et al., 1989].

In Fig. 4.13, it indicates the FWHM of the rocking curve of MnO film grown at different substrate temperatures. When the substrate temperature is increased from 200 °C to 400 °C, it shows a sharp decrease in FWHM from 3.6° to 0.9°. Thereafter, the FWHM keeps a constant value when the substrate temperature is further increased.

The results in Fig. 4.14 show that the out-of-plane lattice constant parameter decreased with increasing substrate temperature. It decreases from 0.445 nm at 200 °C to 0.442 nm at 500 °C. The small change of lattice parameter may be the results of stress relaxation.
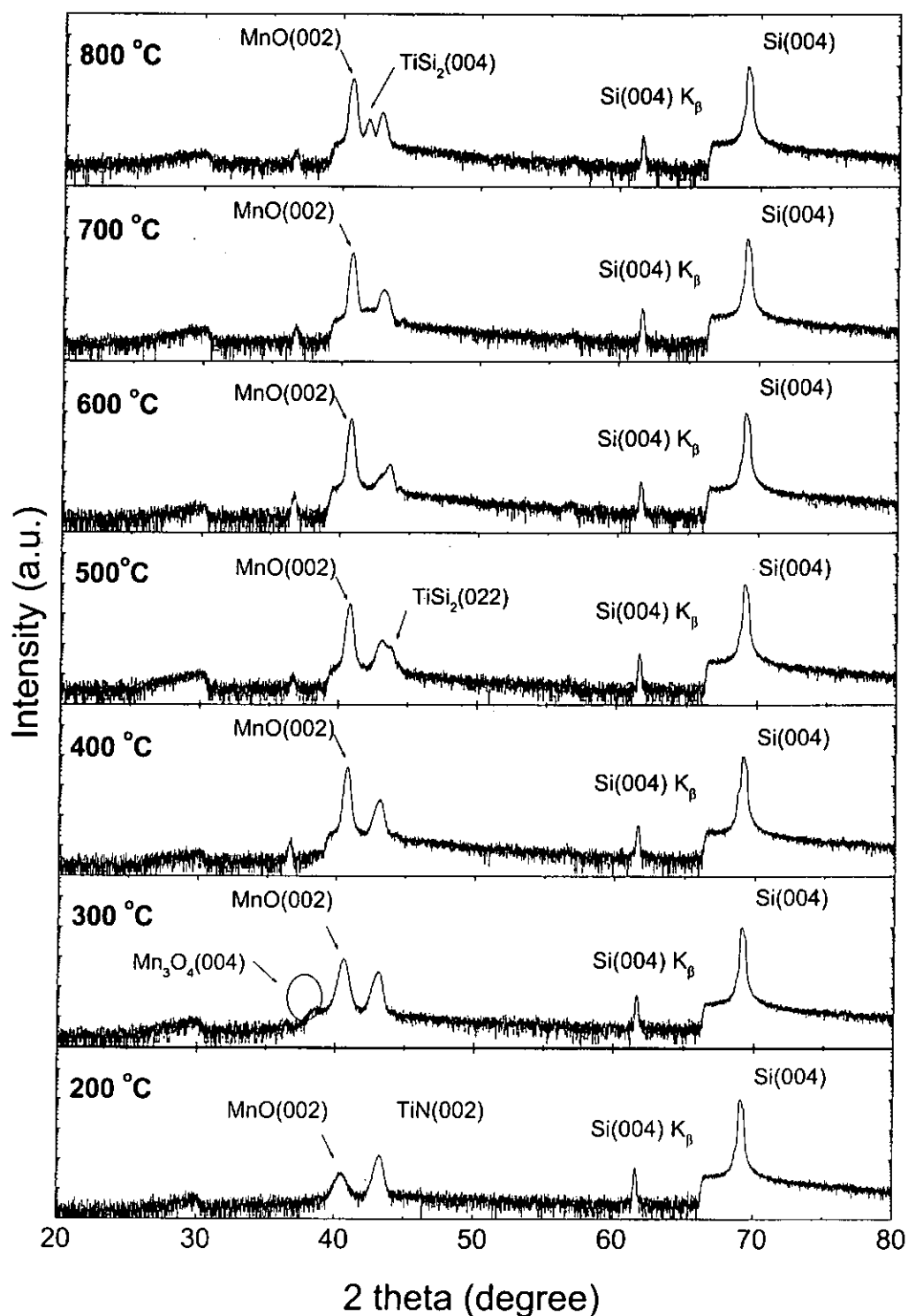
Figure 4.12 XRD patterns for MnO deposited on TiN buffered Si(001) at different temperatures from 200 °C to 800 °C under high vacuum with the same thickness of about 250 nm.
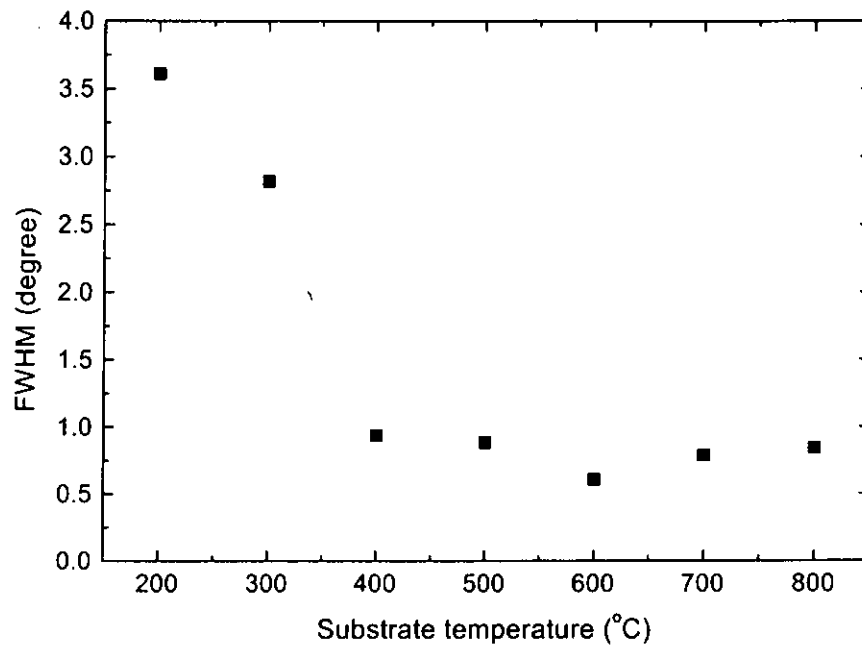
Figure 4.13 Plot of variation of MnO(002) peak intensity with substrate temperature.
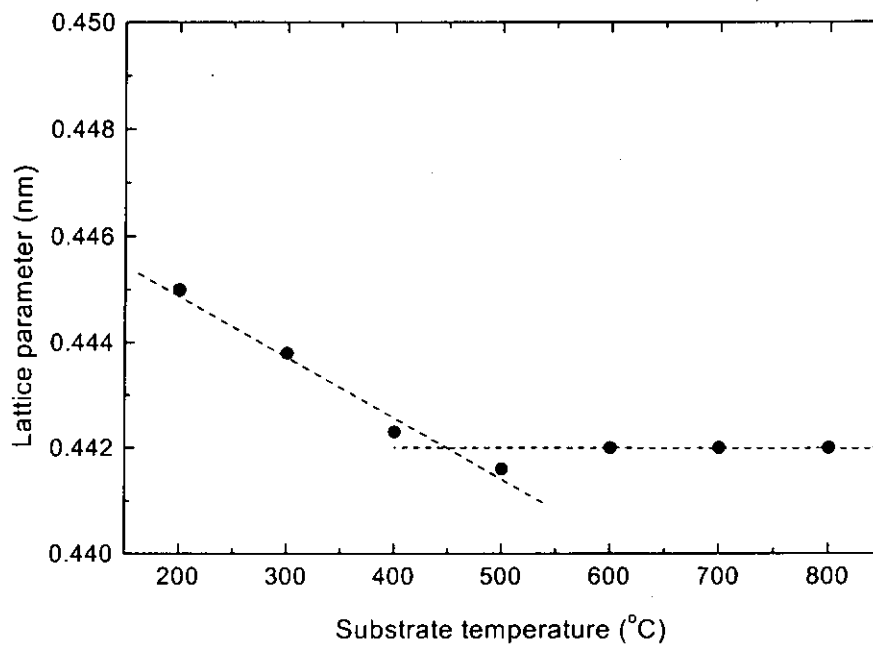
Figure 4.14 Plot of variation of lattice constant of MnO with substrate temperature.

Fig. 4.15(c), 4.16(c) and 4.17(c) show the cross-sectional images of MnO/TiN/Si structure along the <001> direction of silicon. The effect of the film surface morphology to the substrate temperature matches with the structure-zone model (SZMs) [Grovenor et al., 1984], which describes the change of microstructure as a function of the homogeneous temperature, $T_h = T_s/T_m$ (where T_s is substrate temperature, T_m is the melting point). At 200 °C substrate temperature ($T_h = 0.22$), a sharp interface boundary with small grains of manganese oxide is observed. When the substrate temperature is increased to 500 °C ($T_h = 0.42$), columnar grains with tight boundaries appear, as shown in Fig. 4.16(c). At this substrate temperature, grain boundaries within the film become mobile and surface diffusion and recrystallization occur. When the substrate temperature is further increased to 800 °C ($T_h = 0.59$), it favors the lateral growth with grain sizes larger than the film thickness. Surface and bulk diffusion and recrystallization occur, yielding larger crystallites. This is reflected by the increased roughness as seen in the SEM cross-section micrograph in Fig. 4.15(c).

The XRD and SEM studies have shown that the substrate temperature is an important process parameter that influences the film's crystallinity and surface morphology. In fact, the substrate temperature plays important roles in different aspects of PLD of MnO films. Firstly, in the deposition process, the MnO film is fabricated from a higher oxidation state of target Mn_3O_4. More oxide species other than MnO are expected to reach the substrate or the film surface. At lower substrate temperature, the fast cooling rate of the oxide species rapidly reduces their kinetic energy before they are being desorbed. The oxygen-enriched surface therefore favors

to form impurity phases of Mn_2O_3 and Mn_3O_4. Thus, it is expected that a high substrate temperature could reduce such kind of contamination. Secondly, the higher kinetic energy of the ablated species also enhances the surface diffusion of the atoms. The mobile atoms are able to move to their most stable positions which are created by the potential field of the substrate. So, at high enough substrate temperature, the cooling rate decreases and the conditions exist for complete crystallization of the adatoms, leading to better crystallinity.
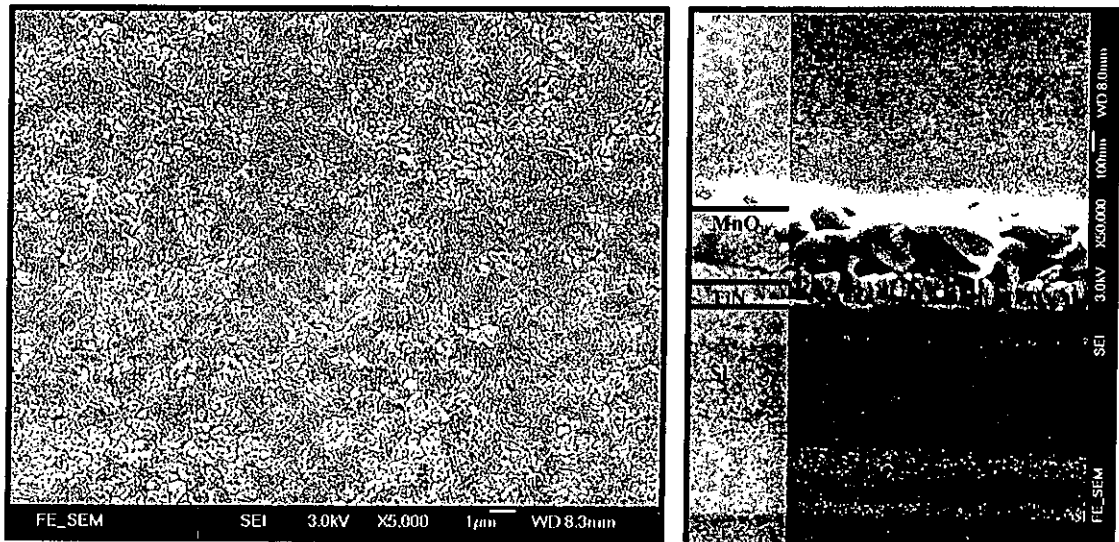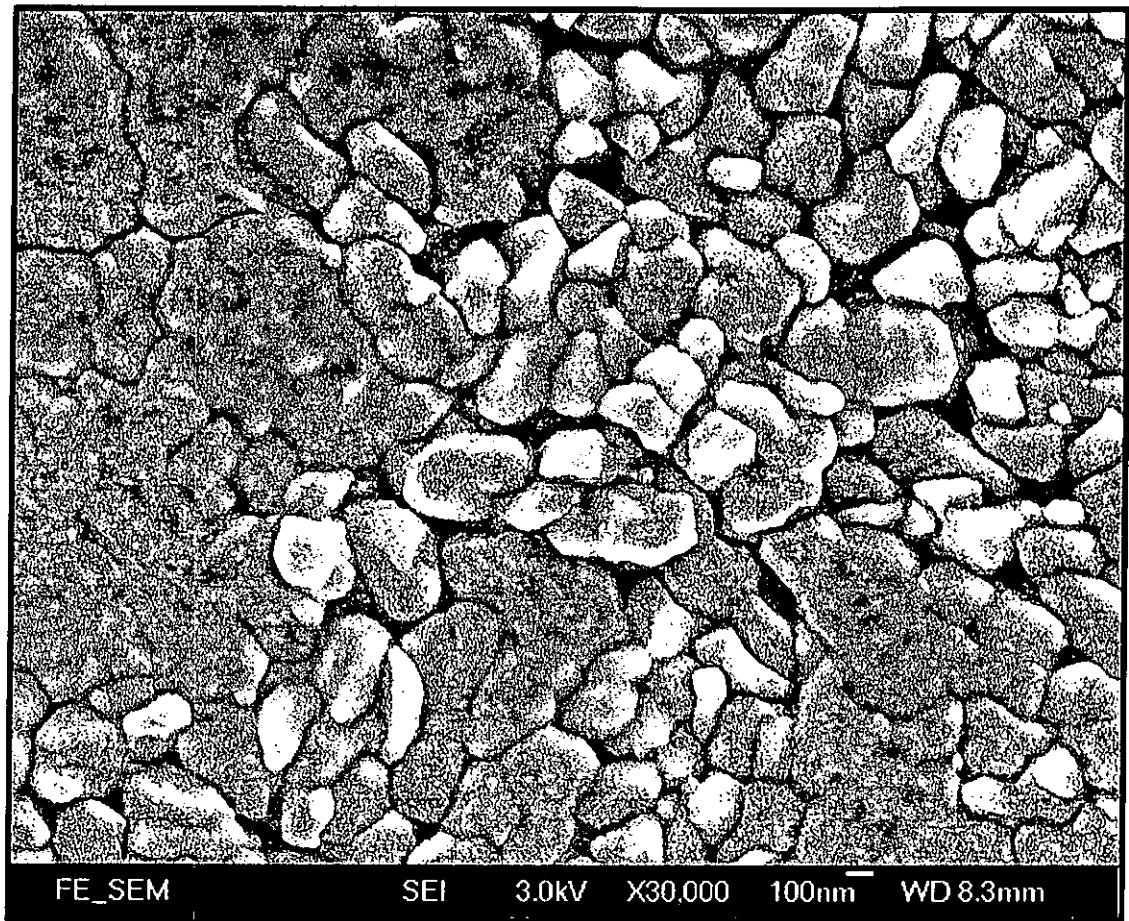
Figure 4.15 SEM images of MnO film deposited on TiN buffered Si at 800 °C (a) surface morphology showing the large grain size, (b) densely packed grains and crack free surface and (c) the cross section of MnO (400 nm)/ TiN (150 nm)/Si.
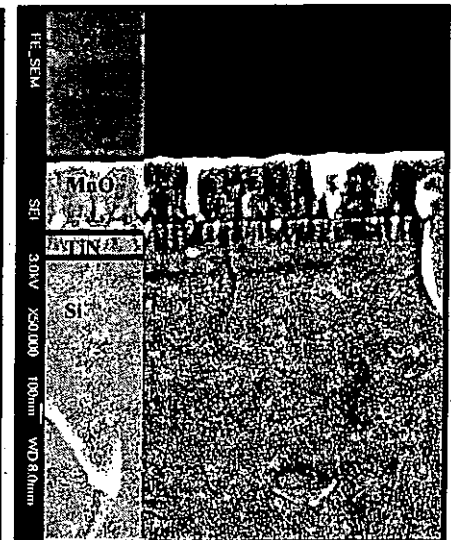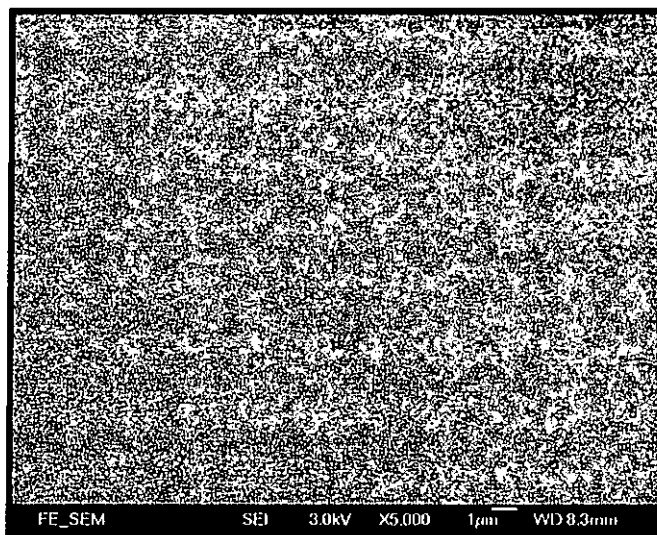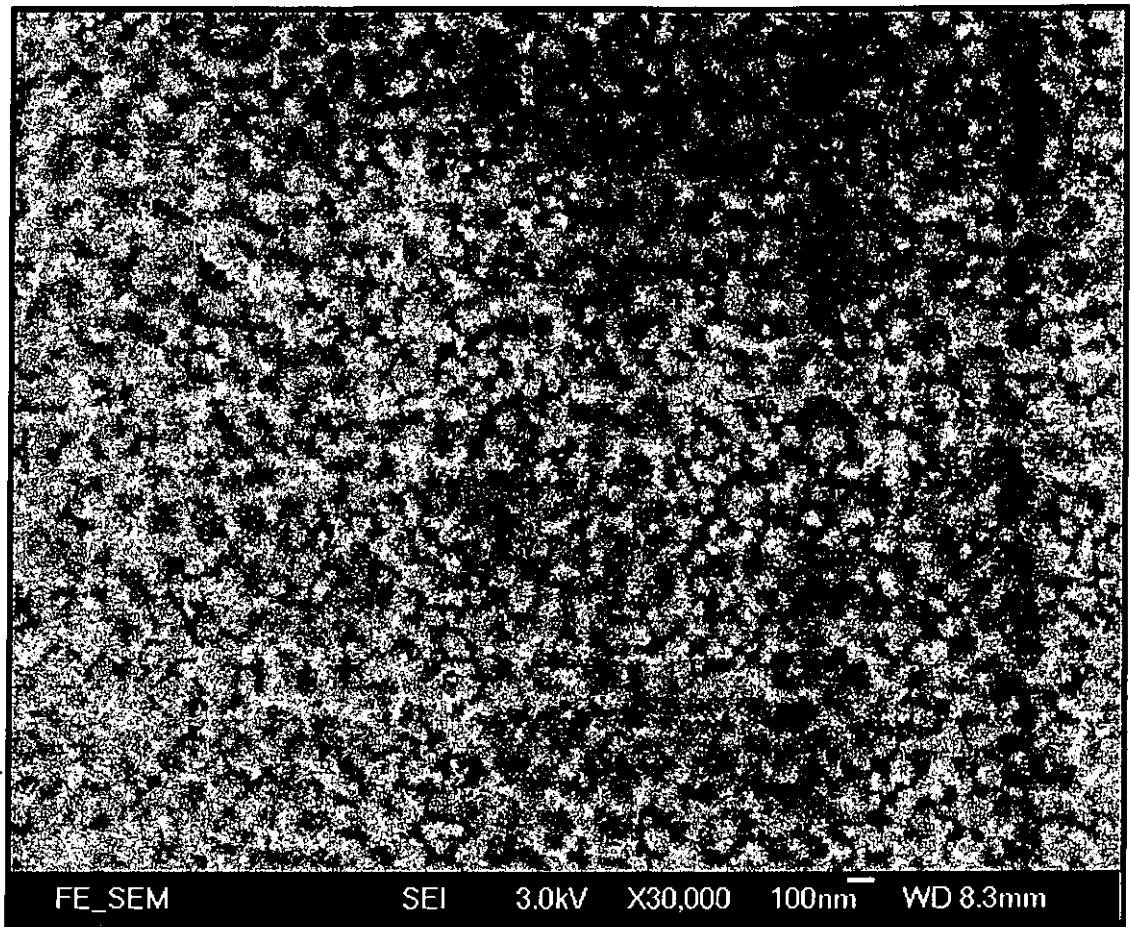
Figure 4.16 SEM images of MnO film deposited on TiN buffered at 500 °C (a) surface morphology showing a relatively smaller grain size, (b) densely packed grains and crack free surface and (c) the cross section of MnO (400 nm)/ TiN (150 nm)/Si showing a sharp interface and columnar grains.
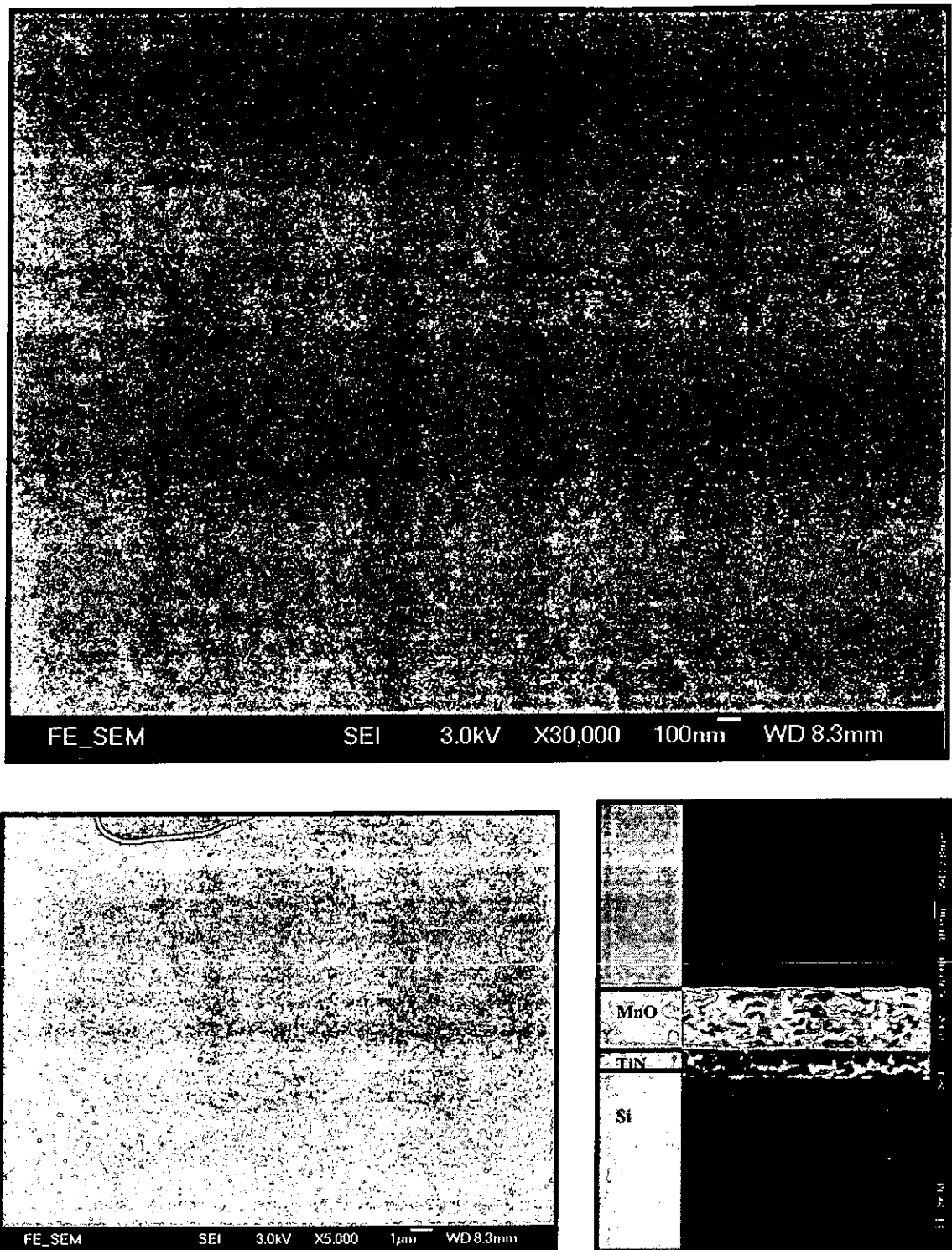
Figure 4.17 SEM images of MnO film deposited on TiN buffered Si at 200 °C (a) smooth surface of MnO, (b) crack free surface without particulates and (c) a sharp interface and smooth film surface indicated in the cross section of MnO (400 nm)/ TiN (150 nm)/Si.

4.4.2 Deposition pressure dependence

In this section, we describe results of studies of the effects of ambient pressure on the structural and electrical properties of the MnO films. Fig. 4.18 shows the XRD pattern obtained from MnO films deposited on TiN/Si(001) at 600 °C in different ambient pressures ranging from 2×10^{-5} Torr to 1×10^{-2} Torr.

These XRD patterns indicate sharp peaks at near 40.7° which correspond to the MnO(002) orientation. The MnO phase exists in all cases when the deposition pressure is below 10^{-2} Torr. No other MnO orientation diffraction peaks are observed. Therefore, the grown films have a preferred MnO(001) orientation parallel to the TiN/Si(001) substrate. The small variation of lattice constants due to the deposition pressure are found and shown in Fig. 4.19. Apparently the lattice constant does not show any obvious trends which could be associated with the oxygen partial pressure during deposition. As such, the variation in lattice constant cannot be used as a diagnostic method to determine the oxygen content in the films.

Fig. 4.20 shows the normalized peak intensity of the MnO(002) diffraction with respect to the peak of Si(004) peak as a function of the ambient pressure. It clearly indicates a drastic increment of peak intensity with decrease of deposition pressure. In Fig. 4.21, the rocking curve measurement on the (002) diffraction reveals that the full width at half maximum (FWHM) for the MnO films decreases from 4.60° to 1.33° as the deposition pressure changes from 1×10^{-2} Torr to 2×10^{-5} Torr. Thus, these trends strongly imply that the orientation and crystallinity quality of the MnO films improve with decreasing deposition pressure.

The origin of the drastic change in the MnO thin film structure in the intermediate pressure range is not yet explained. It is not possible to correlate this change solely with a change in the energy of the incident species in the laser plume. Actually, the expansion velocity of the species ejected from a target during laser ablation remains roughly constant from vacuum up to an ambient pressure on the 10^{-2} to 10^{-1} Torr range.
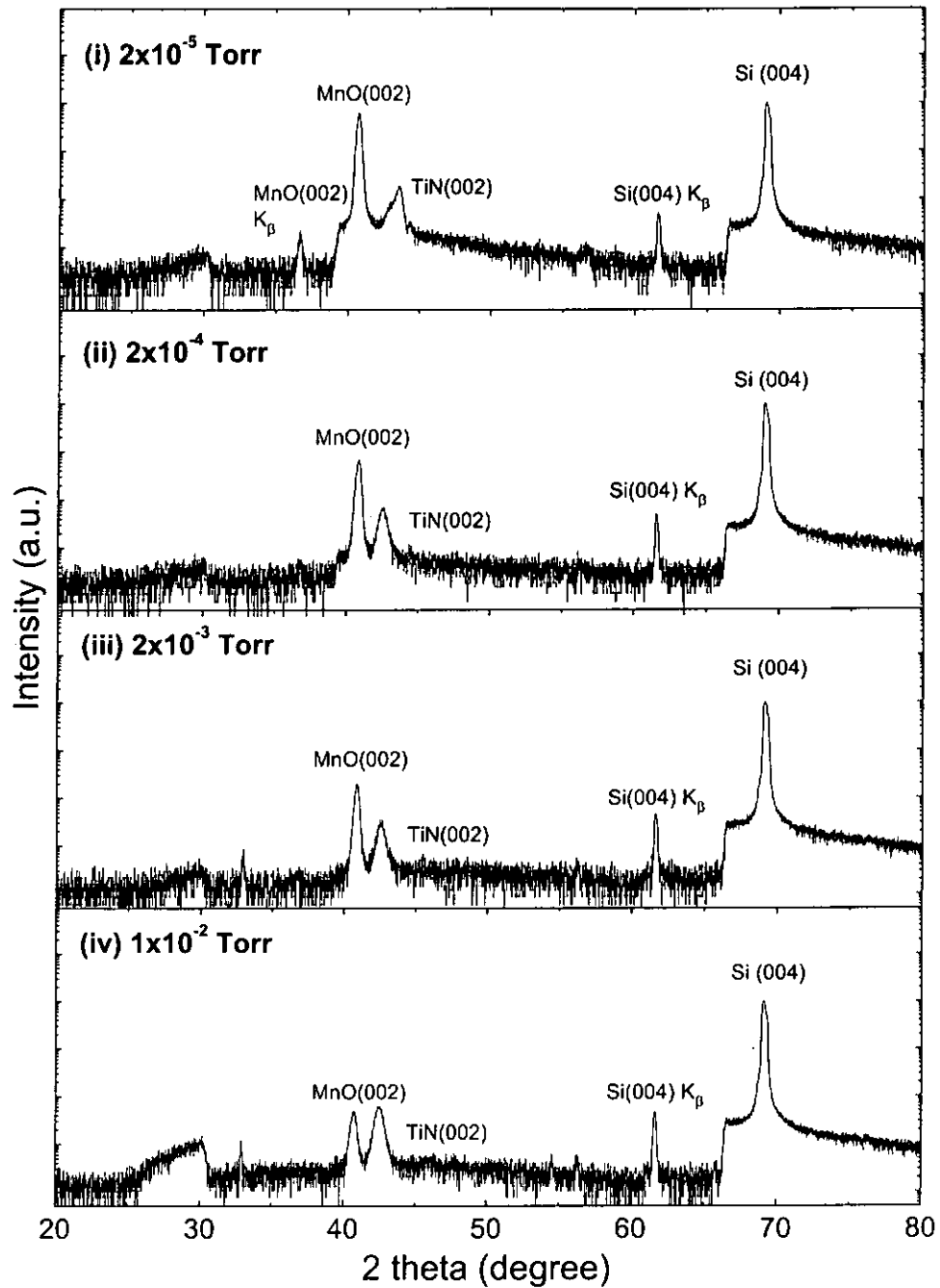
Figure 4.18 XRD patterns for MnO films prepared on TiN buffered Si(001) substrate at 600°C under different ambient pressures (i) 2x10^{-5} Torr, (ii) 2x10^{-4} Torr, (iii) 2x10^{-3} Torr and (iv) 1x10^{-2} Torr.
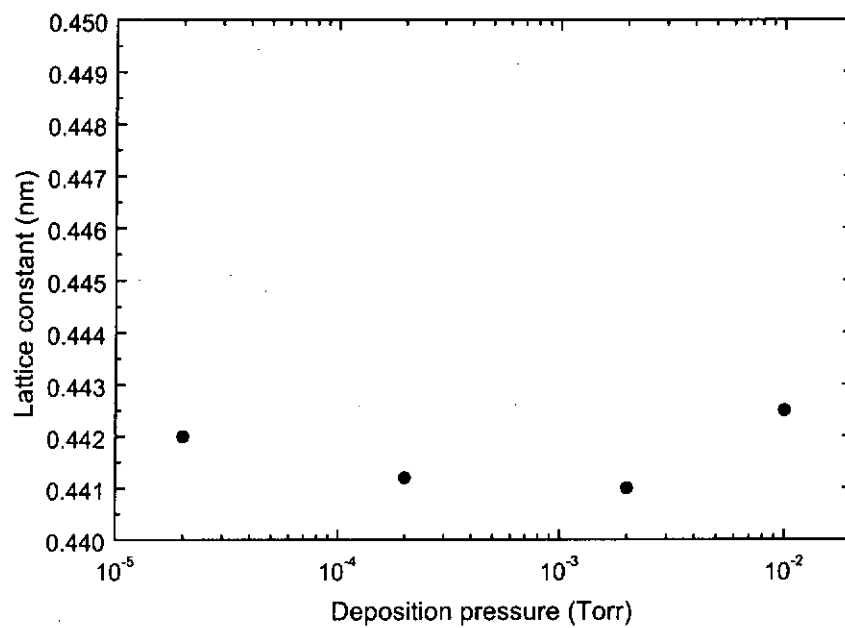
Figure 4.19 Plot of variation of out-of-plane lattice constant of MnO films with substrate temperature.
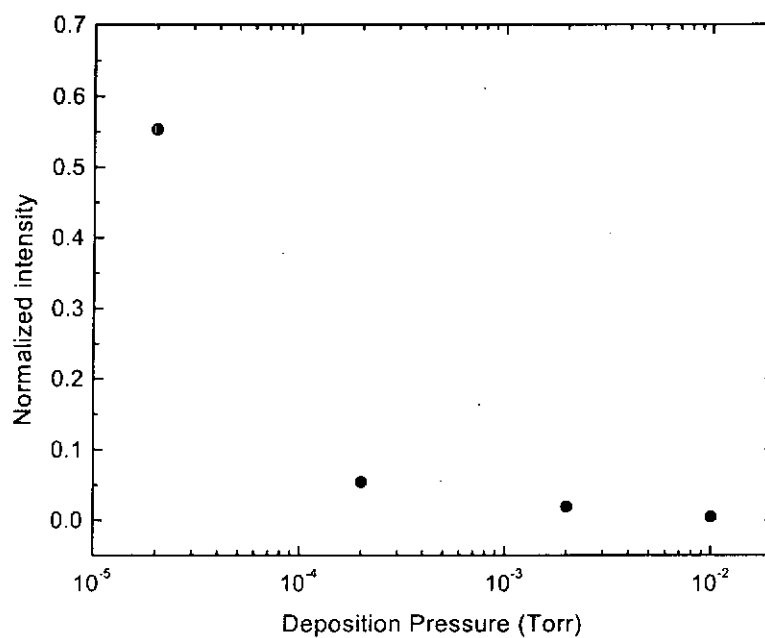
Figure 4.20 Peak intensity of the MnO(002) diffraction as a function of the deposition pressure for the MnO film prepared on TiN buffered Si(001) substrates.
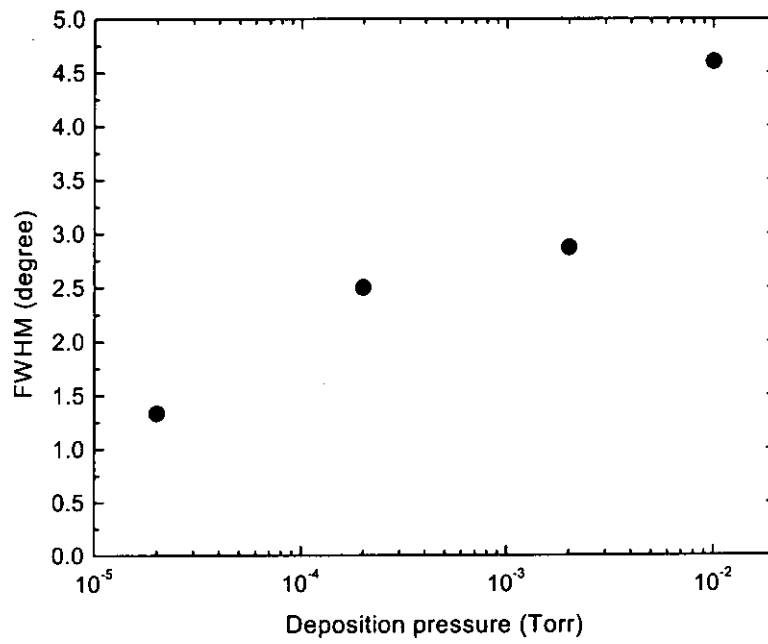
Figure 4.21 Rocking curve FWHM of the MnO(002) diffraction as a function of the deposition pressure for the MnO film prepared on TiN buffered Si (001) substrates.

4.5 Electrical characterization

4.5.1 Leakage current measurement

MnO is a well-known dielectric material. As mentioned before, the difficulty of surface analysis such as X-ray photoelectron spectroscopy (XPS) on MnO surface is due to this dielectric nature. Strong charging effect of the sample surface makes the interpretation of data inaccurate. Such kind of problems can be avoided by epitaxial growth of MnO oxide on metallic material, such as Pt. Thus, removals of charge from MnO surface to the substrate are achieved through some leakage mechanisms like tunneling.

On the other hand, insulation resistance is a primary factor to determine the merit of performance of this material in capacitor application. It is a measure of the capability of a material to withstand leakage of current under a DC voltage. Small leakage current enables high capacitor density. For example, the leakage current density should be as low as 10^{-7} A cm^{-2} at 1 V for a DRAM application.

Before studying the dielectric properties of MnO, the transport properties of the Pt and TiN thin films were measured by resistivity measurements as a function of temperature by a standard DC four-point probe method. A metallic behavior was observed in the films. The room temperature resistivities of these Pt films and TiN films are comparable to the bulk resistivities. Such films can be used as a perfect electrode in the multilayered system.
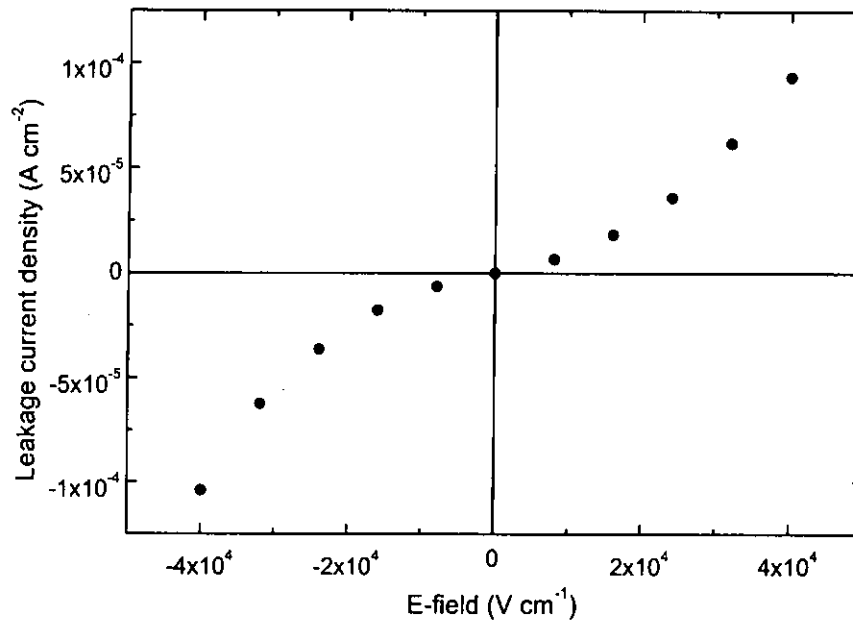
Figure 4.22 Plot of leak current density versus E-field for the Pt/MnO/TiN heterostructure.

Electrical properties of the MnO films were studied by fabricating multilayer capacitor structures using platinum and TiN electrodes. About 250 nm thick oxide layer was deposited at 600 °C in 2×10^{-5} Torr ambient. Characteristic leakage current as a function of electric field for the Pt/MnO/TiN capacitor structure grown on Si(001) substrate is shown in Fig. 4.22. The measurements were performed under room temperature.

The current response of the Pt/MnO/TiN structure on the external electric field possesses a typical behavior of metal-insulator-metal capacitor. From the linear part of the curves, low field resistivity of 18.58 Ω cm is obtained. It also indicates that the leakage current density - electric field is quite symmetric although the two electrodes were made from two different materials.

4.5.1(a) Thickness dependence of leakage current

Fig. 4.23 illustrates the leakage current density versus applied E-field for the capacitors of different MnO layer thickness. The MnO layers were prepared at 600 °C. The obtained results imply that the leakage current density of MnO films increases with decreasing film thickness. Example of this are the values from 7.86 A cm^{-2} to 1.17 x 10^{-8} A cm^{-2} obtained with increasing film thickness from 34 to 450 nm at an E-field of 10^5 V cm^{-1} (see Fig. 4.24.). These data reveal that the leakage current is highly sensitive to the MnO film thickness.
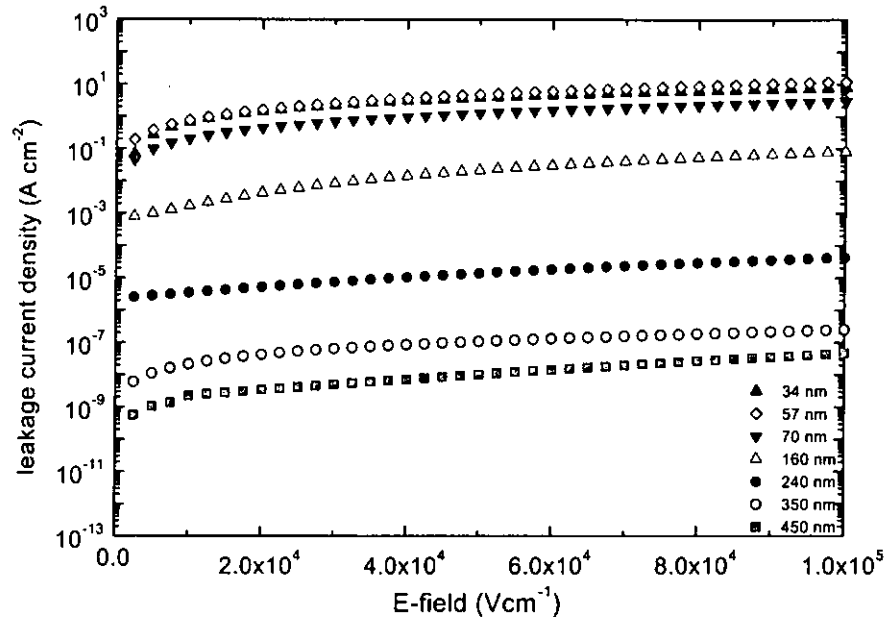
Figure 4.23 The thickness dependence of DC conduction for the heterostructure of Pt/MnO/TiN/Si.
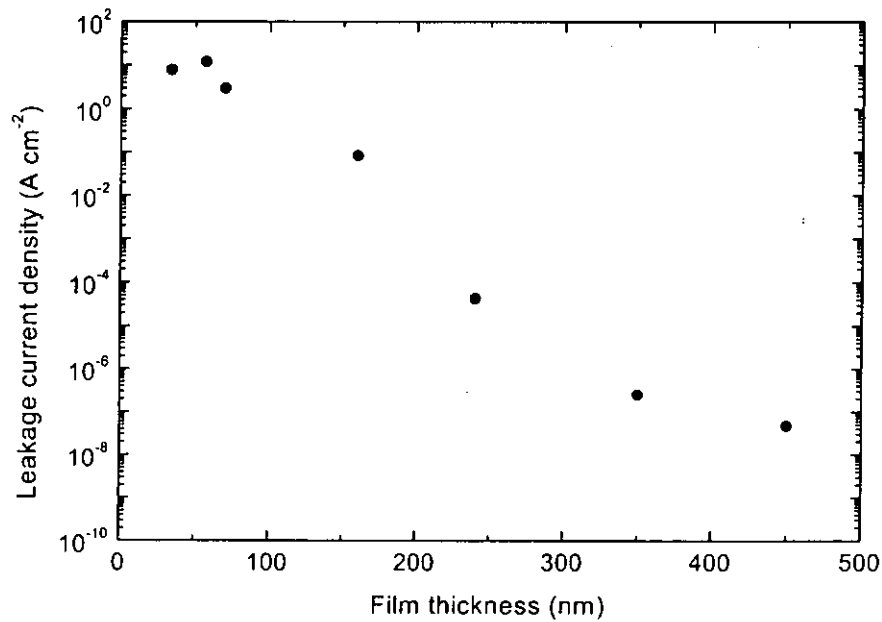
Figure 4.24 Plot of leakage current density versus the thickness of MnO at 1×10^5 V cm^{-1}.

4.5.1(b) Substrate temperature dependence

The effects of substrate temperature on the leakage current of MnO films were studied also. MnO films were deposited on TiN buffered silicon substrate to form a heterostructure of Pt/MnO/TiN/Si(001). The deposition took place at substrate temperature ranging from 200 °C to 700 °C in an ambient of 2×10^{-5} Torr air. Film thickness of the grown films was set to a constant (250 nm) by controlling deposition duration.

The leakage current density versus applied electric field for the MnO film is shown in Fig. 4.25. A relation of substrate temperature and leakage current density was also obtained and is shown in Fig. 4.26. A continuous improvement in leakage current with increasing substrate temperature is apparent. A substantial decrease in leakage current is found for films deposited at higher than 500 °C. In such cases, the resulting structure is highly oriented columnar crystalline with grain size close to the film thickness. Films grown at lower temperatures have smaller grains. There are, therefore, a large number of grain boundaries and possibly impurity phases between grains. All these favor charge carrier conduction and hence lower resistivity in the films.
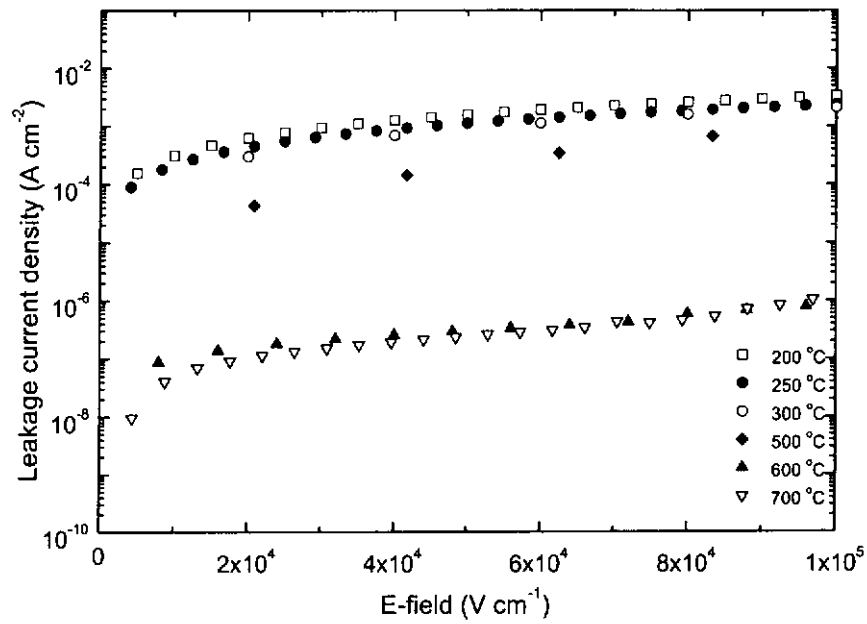
Figure 4.25 The substrate temperature dependence of leakage current density against applied E-field for the heterostructure of Pt/MnO/TiN/Si.
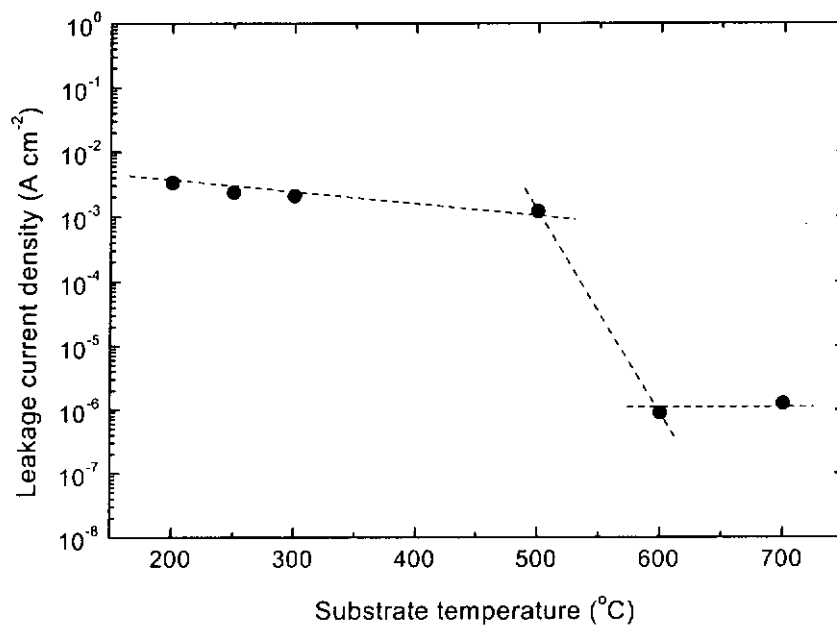
Figure 4.26 J-Ts plot for applied an E-field of 1x10^5 V cm^{-1} in Pt/MnO/TiN capacitor.

4.5.1(c) Deposition pressure dependence

Results of the structural characterization of MnO films reveal that the crystallinity can be improved by lowering the deposition pressure. It is also believed that the deposition pressure can alter the oxygen content in the MnO films. In the present studies the dielectric properties and leakage current of the MnO films are examined for deposition pressure from 2×10^{-5} Torr to 1×10^{-2} Torr. The films were grown at 600 °C and the measurements were carried out at room temperature in air.

Fig. 4.27 shows the J-E relationship of the Pt/MnO/TiN capacitor. The leakage current density is low for MnO films deposited at low deposition pressure. Typical leakage current density of the samples at 1×10^5 V cm^{-1} are summarized into Fig. 4.28. It shows values of 2.9×10^{-6} to 0.87 A cm^{-2} for deposition pressure from 2×10^{-5} Torr to 1×10^{-2} Torr. This clearly indicates a substantial improvement in leakage current for the MnO film deposited at lower deposition pressure.

In fact, the MnO thin films may be further oxidized as the deposition pressure is increased. With increasing deposition pressure Mn^{2+} content decreases while Mn^{3+} increases. The increased leakage current density in MnO films grown at high oxygen pressure is probably attributed to the enhanced electron hopping conduction between Mn^{2+} and Mn^{3+}. Finally it may lead to degradation of the insulating properties of MnO film.
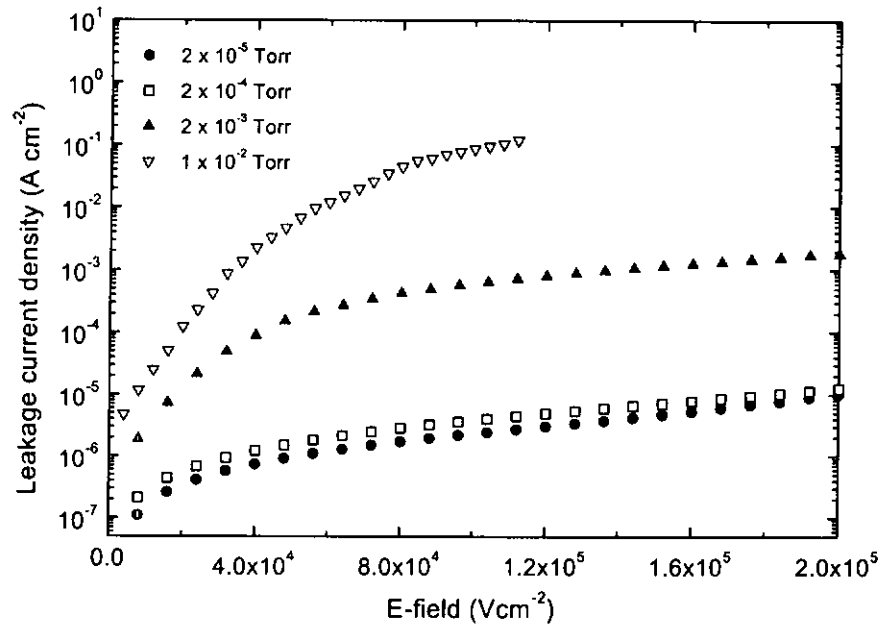
Figure 4.27 The deposition pressure dependence of leakage current density for the heterostructures of Pt/MnO/TiN/Si(001).
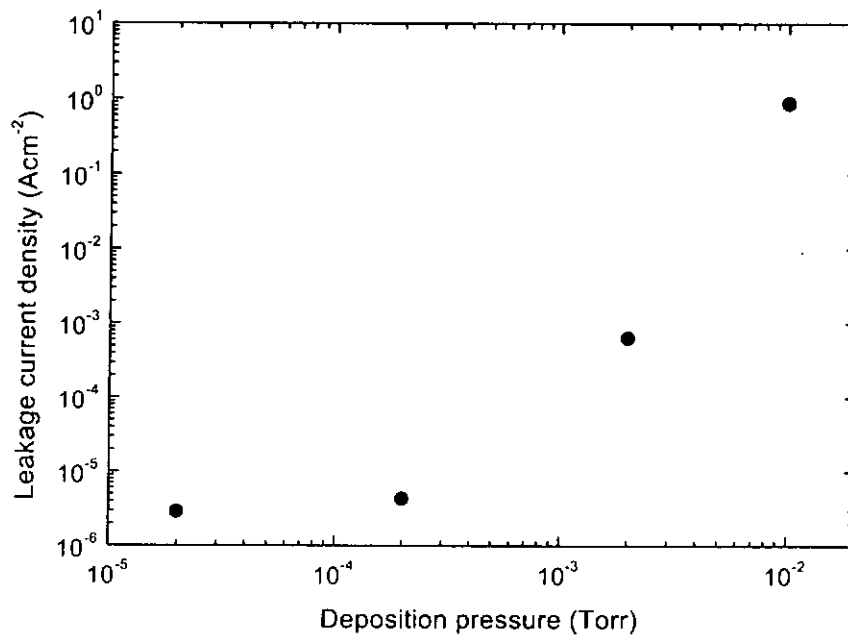
Figure 4.28 J-P plot of an electric field of 1×10^5 Vcm^{-1} in Pt/MnO/TiN capacitor.

4.5 Dielectric Measurement

The static or low frequency dielectric constant of an ionic solid usually has two contributions, given by:

$$\varepsilon = \varepsilon_\infty' + \frac{(ze*)^2 N}{\pi \mu v_T^2} \left(\frac{\varepsilon_\infty' + 2}{3} \right)^2$$

where ε_∞' is the high frequency or electronic part and the second term is due to the lattice polarizability in which z is the valence, e* is the Szigeti effective ionic charge, μ is the reduced mass of the two ions, N is the number of ion pair per unit volume, and v_T is the frequency of the appropriate transverse optical mode. The lattice contribution is affected by the electronic polarizability in two ways: a short-range effect covered by e* and a contribution due to long-range interactions results in the enhancement factor $\left[\frac{1}{3}(\varepsilon_\infty' + 2) \right]^2$. Thus the study of the dielectric response of a solid provides valuable information about its electronic properties and lattice dynamics.

In this section, the dielectric properties of MnO films are typically found to be somewhat moderate as compared with the properties of bulk sample. The 250 nm thick MnO sample was deposited at 600 °C in 2×10^{-5} Torr ambient pressure by PLD. The effect of frequency on the dielectric properties of Pt/MnO/TiN capacitor was measured from 1 kHz to 10 MHz. All measurements were performed at room temperature.

The dielectric properties of the sample are presented in Fig. 4.29. They reveal dispersion in the dielectric properties, largest at low frequencies. The dispersion found is shown to be well accounted for by an electrode polarization effect. At high frequency range (10 MHz), the dielectric constant approaches a value of 16.4 and the dissipation factor is 0.049. The room temperature value of dielectric constant of 17.4 at frequency of 0.1 MHz is slightly smaller than that of 18.8 reported by others [Kinney et al., 1969 and Chandhury et al., 1969].
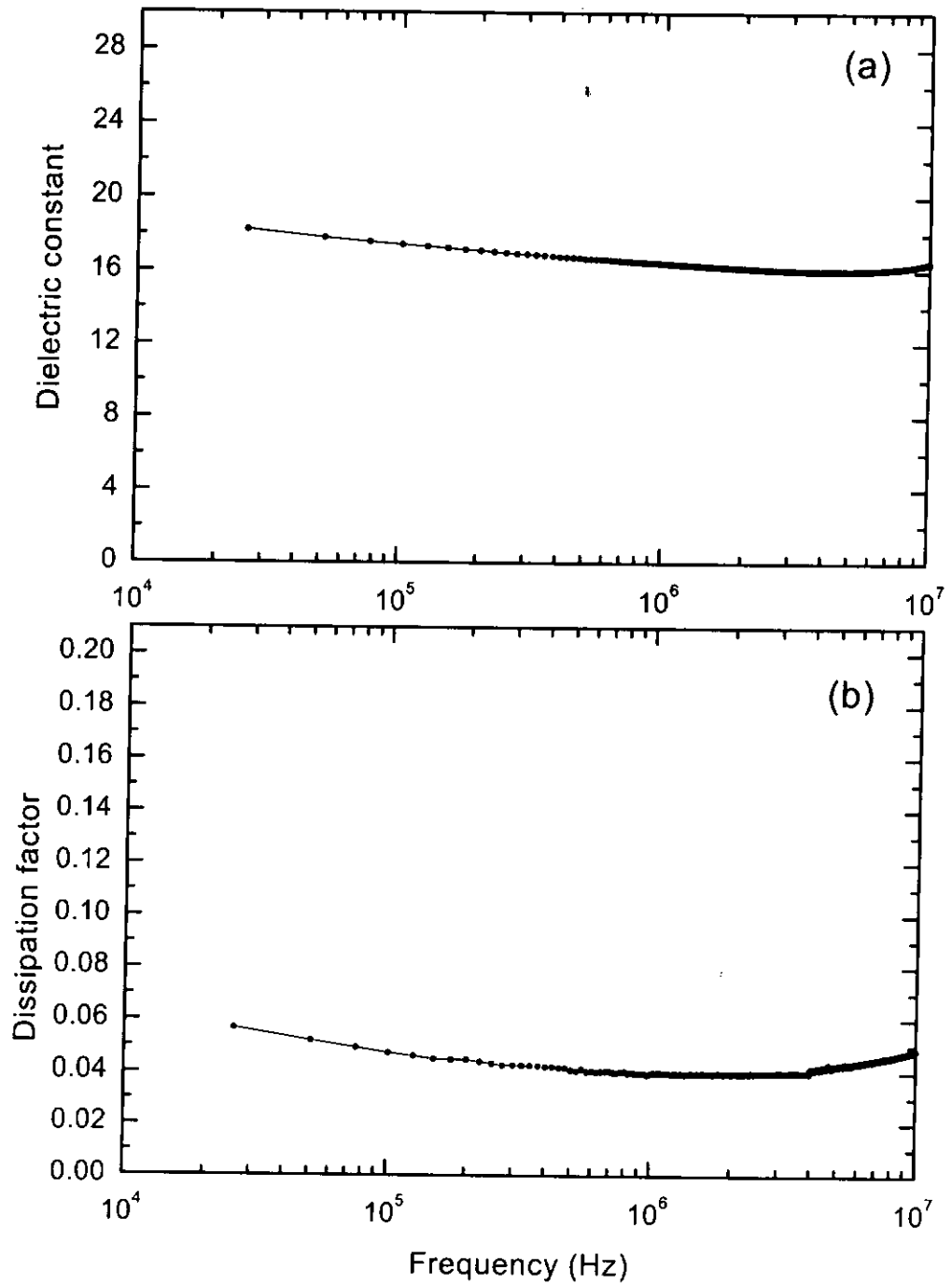
Figure 4.29 The (a) dielectric constant and (b) dissipation factor for the heterostructure of Pt/MnO/TiN/Si.

CHAPTER 5

Fabrication and characterization of MnO thin film on MgO substrate

5.1 Introduction

In the last chapter, we have made an integrated MIM capacitor structure based of MnO insulating layer. The correlation of the dielectric properties and deposition parameters has been identified. Now we turn our attention to the electrical transport properties of MnO thin films grown by pulsed laser deposition.

The rapid development of semiconductor industry demands an ever greater application of materials of varying physical and chemical properties. This demand cannot be fully met by a handful of elements having semiconducting properties, nor by the few relevant chemical compounds, which are already understood. Therefore increasing attention is being paid to studies of other chemical compounds that can act as semiconductors. In this respect, doped transition metal oxides, such as MnO become important.

In the early studies, measurements on MnO were performed mainly on sintered materials, or on single crystals of not too high purity. The data obtained were not that reliable and in some cases difficult to interpret. The mastering of MnO thin film

growth technique thus allows a better understanding of their basic properties, in particular of their defect structure and transport properties. In the following sections we report on the electrical transport properties in MnO thin films.

5.2 Deposition of MnO on MgO(001) substrate

In order to eliminate the substrate effect on the electrical properties of MnO, MgO single crystal substrate was selected. As described in pervious chapters, we have studied and obtained epitaxial growth of the MnO films on MgO single crystal substrate.

In fact, by comparing with the metal or semiconducting substrates, MnO films grown on insulating substrates of MgO are easiest to prepare. MgO has a band gap of 7.8 eV and cannot be made conducting by doping. Also, MgO is highly inert, allowing deposition temperature up to the melting point of the overlayer. MgO has the same structure as MnO with a lattice constant of 0.421 nm. The lattice mismatch between MnO and MgO is as small as 5 %. Also, the thermal expansion coefficients of MnO ($11.0 \times 10^{-6} K^{-1}$) and MgO ($10.8 \times 10^{-6} K^{-1}$) are quite similar. All of these point to the possibility that very high quality epitaxial MnO thin films may be achieved.

5.2.1 Deposition of MnO layer

The MnO thin films were grown on MgO(001) substrates using a homemade high purity Mn_3O_4 target. The surfaces of the MgO substrates were ultrasonically cleaned in acetone. The substrates were placed on the substrate holder positioned at 5 cm from the target in the vacuum chamber. The chamber was evacuated to the desired pressure by using a diffusion pump. The target was ablated by a KrF excimer with laser fluence of 5 J cm^{-2}. Thickness of grown films was fixed to about 250 nm.

5.2.2 Structural characterization of MnO/MgO(001)

Fig. 5.1 shows the XRD pattern of the MnO film grown on MgO(001) substrate at 600 °C under 2×10^{-5} Torr ambient pressure. It is clear from the figure that the film has preferential orientation (001) parallel to the substrate surface. From the XRD data we estimated the out-of-plane lattice constant to be 0.443 nm, which is similar to the bulk sample value. As shown in Fig. 5.2, the XRD rocking curve for the MnO(002) diffraction peak is 0.39°. The crystal orientation of the MnO film deposited on MgO(001) is better than on TiN buffered Si(001) substrate with the same deposition condition. Fig. 5.3 illustrates the Φ-scan of MnO/MgO(001) heterostructures. The four-fold symmetric diffraction peaks of a typical cubic structure of the two layers are found to be located at the same angular position. This indicates that the films grown under the deposition condition have good crystallinity and an in-plane epitaxial relationship.

Fig. 5.4 shows the SEM image of the surface of the MnO film fabricated on MgO(001) substrate. The MnO surface appears crack-free, particulate-free and absolutely clean. This featureless and smooth MnO surface may be due to the very small difference in thermal expansion coefficient between MnO and MgO as mentioned before.
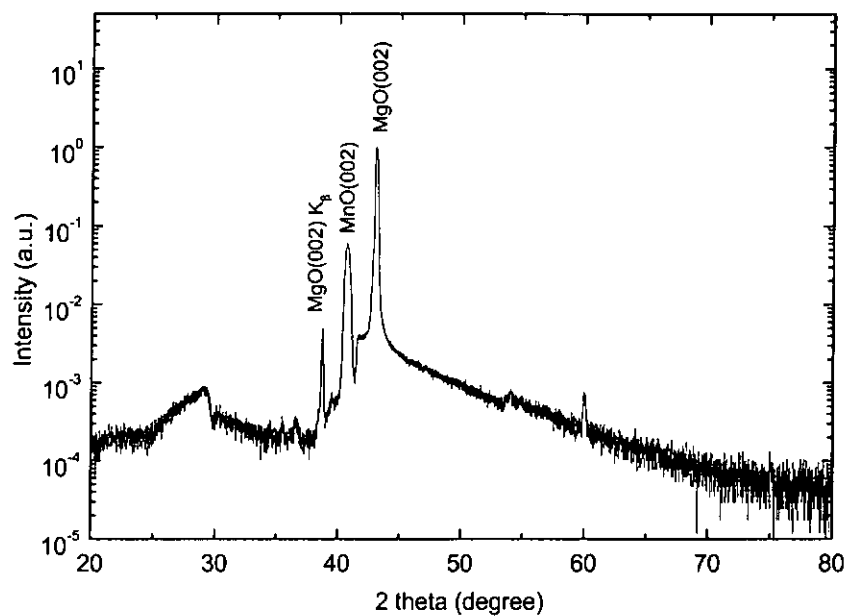
Figure 5.1 XRD pattern of 250 nm MnO thin film deposited on MgO(001) at 600 °C under high vacuum of 2x10⁻⁵ Torr.
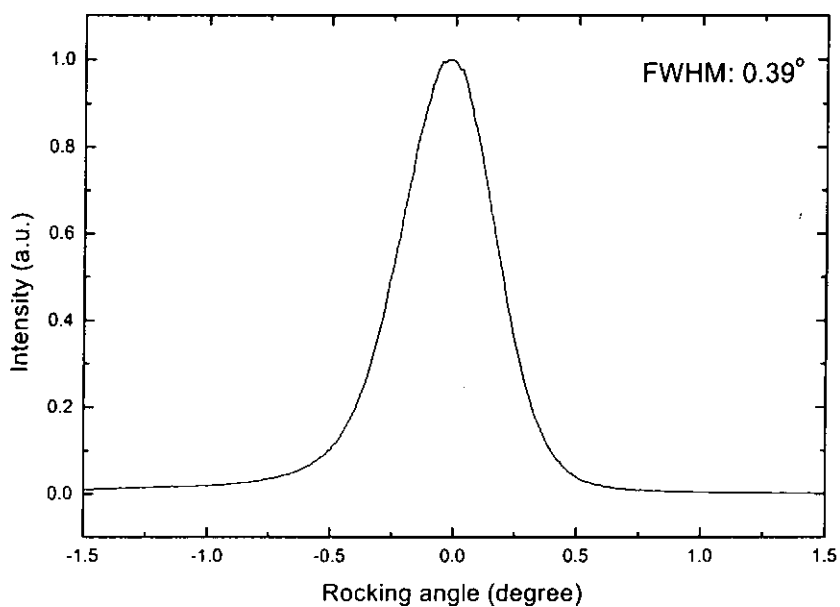
Figure 5.2 XRD rocking curve of MnO(002) exhibiting a FWHM of 0.39°.
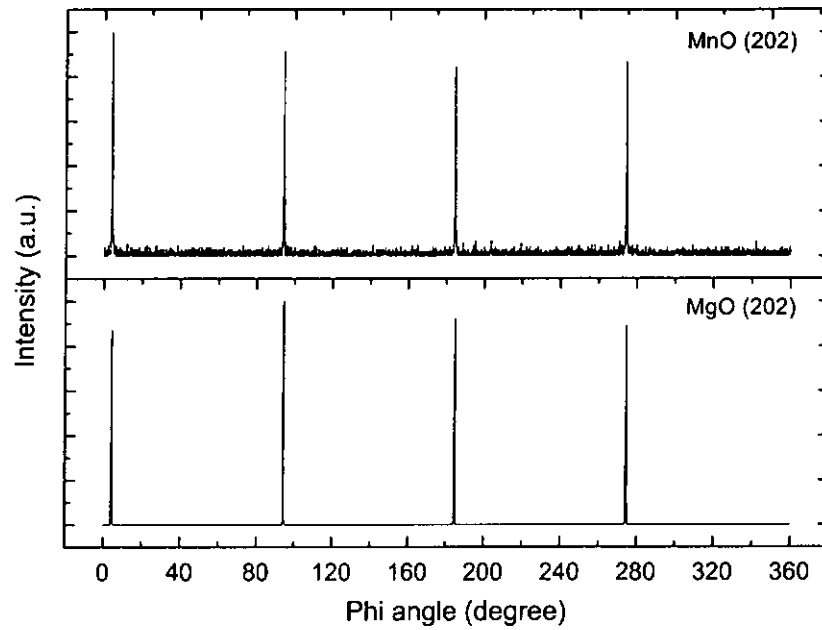
Figure 5.3 XRD Φ-scans from MnO(202) and MgO(202) family reflections.
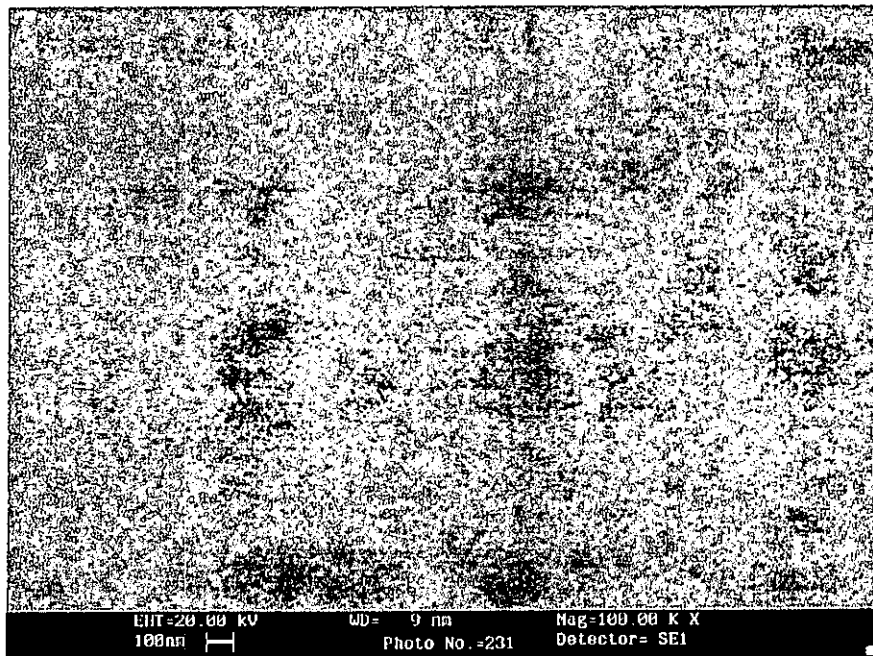
Figure 5.4 SEM image of surface morphology of MnO thin film deposited at 600 °C showing a crack free surface.

5.3 Optimization of deposition condition

5.3.1 Substrate Temperature dependence

We have reported in Section 4.4.1 that the crystal structure of the MnO films is quite sensitive to the substrate temperature during deposition on TiN buffered Si(001). In this section the effect of substrate temperature on the MnO film deposited on MgO(001) substrate are described.

MnO films were grown on MgO(001) substrates by pulsed laser deposition using KrF excimer laser with a repetition rate of 10 Hz. The laser energy density irradiated on the Mn_3O_4 target was 4 J cm^{-2} with a substrate–target distance of 5 cm. The chamber was evacuated by a diffusion pump to a base pressure of 2×10^{-5} Torr. The substrate temperature was held at a fixed temperature from 200 °C to 800 °C. The crystal structure of the MnO films was characterized using X-ray diffractometer.

Fig. 5.5 shows the XRD pattern of MnO/MgO(001) grown at different substrate temperatures. It is clear from this figure that the films are all cube-on-cube grown on the MgO(001) substrates. The relation between the out-of-plane lattice constant and the substrate temperature of the MnO films is obtained (see Fig 5.6). It also shows the intensity of MnO(002) plane reflection increases with the substrate temperature. In Fig. 5.7, the FWHM of the MnO(002) shows a relative large value of 2.6° when the substrate temperature is at or below 300 °C. A significant narrowing is observed when the substrate temperature is increased to 400 °C. The FWHM shows a value of about 0.4° in the range of 500 °C to 800 °C substrate temperature.
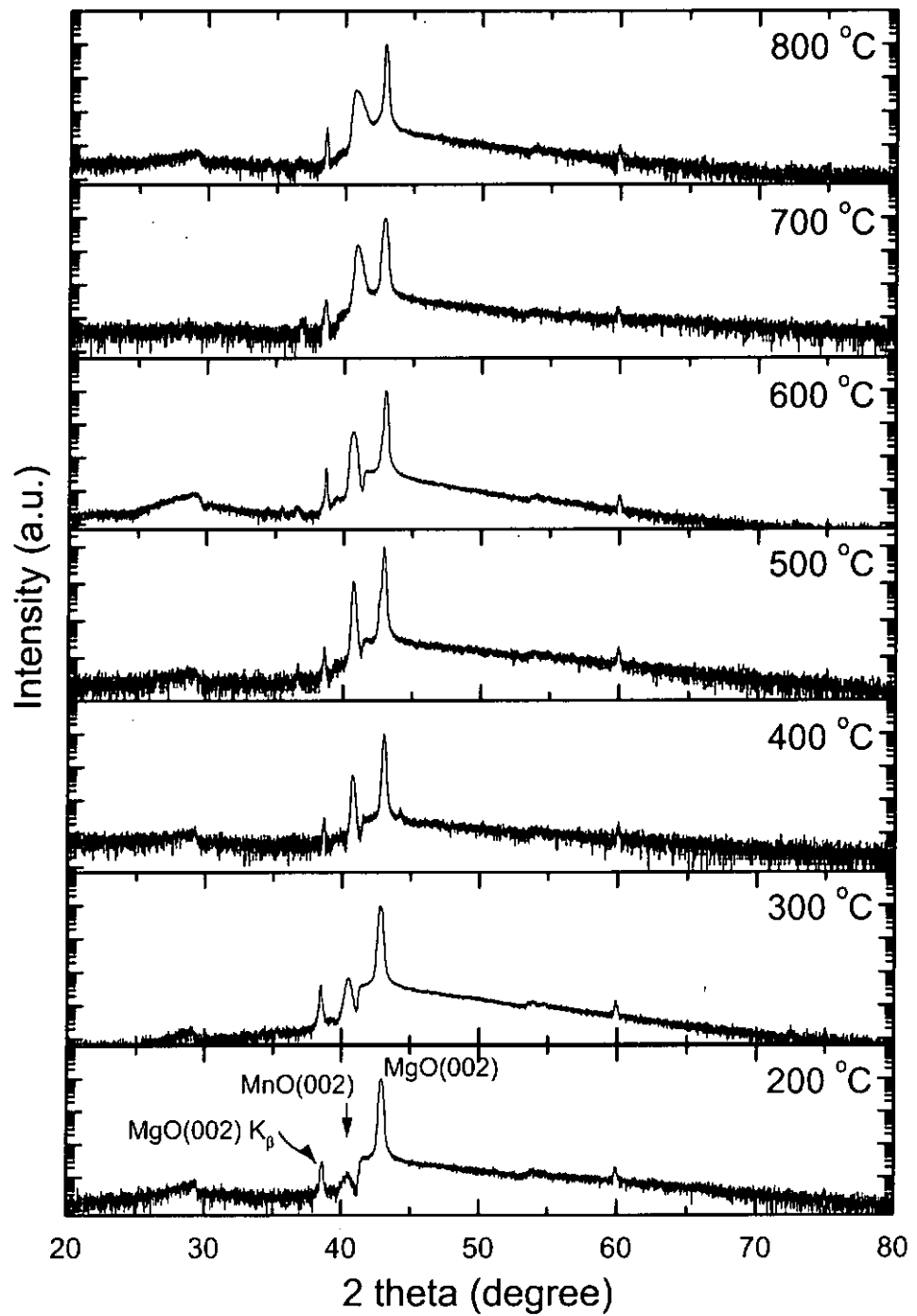
Figure 5.5 XRD patterns for MnO/MgO(001) deposited at different temperatures from 200 °C to 800 °C under high vacuum with the same thickness of about 250 nm MnO film.
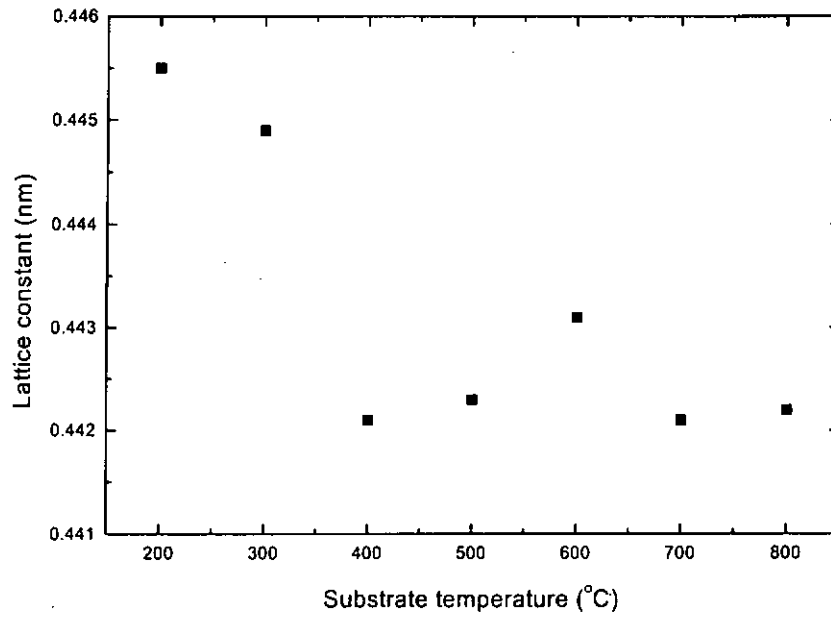
Figure 5.6 The out-of-plane lattice constant of MnO film deposited at different substrate temperatures.
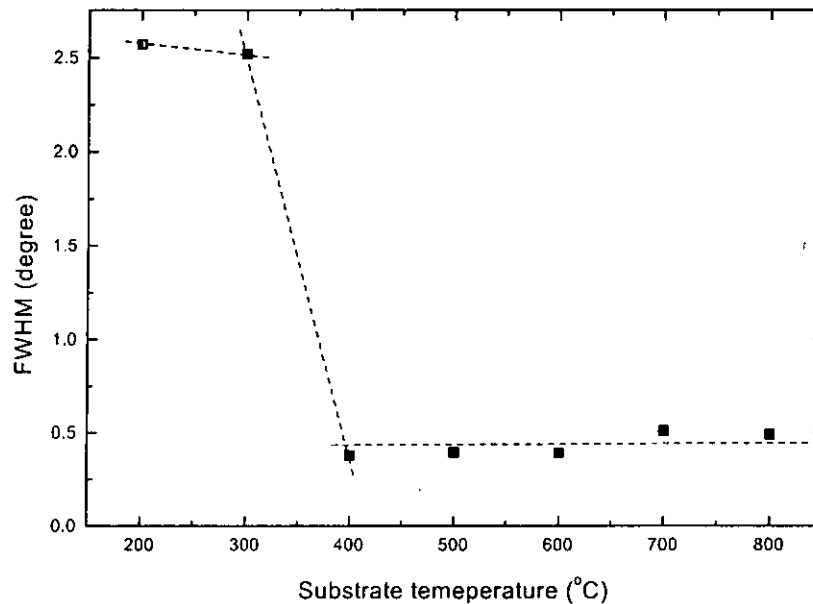
Figure 5.7 The FWHM of rocking curve on the MnO(002) reflection measured for the MnO layer deposited on MgO(001) substrate at different substrate temperature.

5.3.2 Deposition pressure dependence

In this section, a systematic study of the effects of ambient deposition pressure on the structures of MnO is presented. Fig. 5.8 shows the XRD patterns obtained from films deposited on MgO(001) at 600 °C under different ambient pressures from 2×10^{-5} Torr to 1×10^{-2} Torr. These XRD patterns have sharp peaks at about 40.67° of only MnO(002) orientation. Therefore, the grown films have a preferred orientation of MnO(001) parallel to the MgO substrate surfaces. The small variation of the lattice constants of MnO are found and shown in Fig. 5.9. Fig. 5.10 shows the normalized peak intensity of the (002) diffraction as a function of the ambient pressure. It is seen that the crystal growth is enhanced by decreasing the ambient pressure. The rocking curve measurement on the (002) diffraction reveals that the full width at half maximum (FWHM) for the MnO films is decreased from 0.75° to 0.39° by decreasing the deposition pressure from 1×10^{-2} Torr to 2×10^{-5} Torr. Thus, the improvement is similar to the MnO film deposited on TiN buffered Si substrate. But it is worth to note that the degradation of the orientation of the MnO film grown on TiN buffered silicon is more noticeable. It may be due to the high sensitivity of TiN surface on ambient pressure such as the TiN oxidation. Nevertheless, these trends strongly imply that the orientation and crystallinity of the MnO films improve with decreasing the deposition pressure.
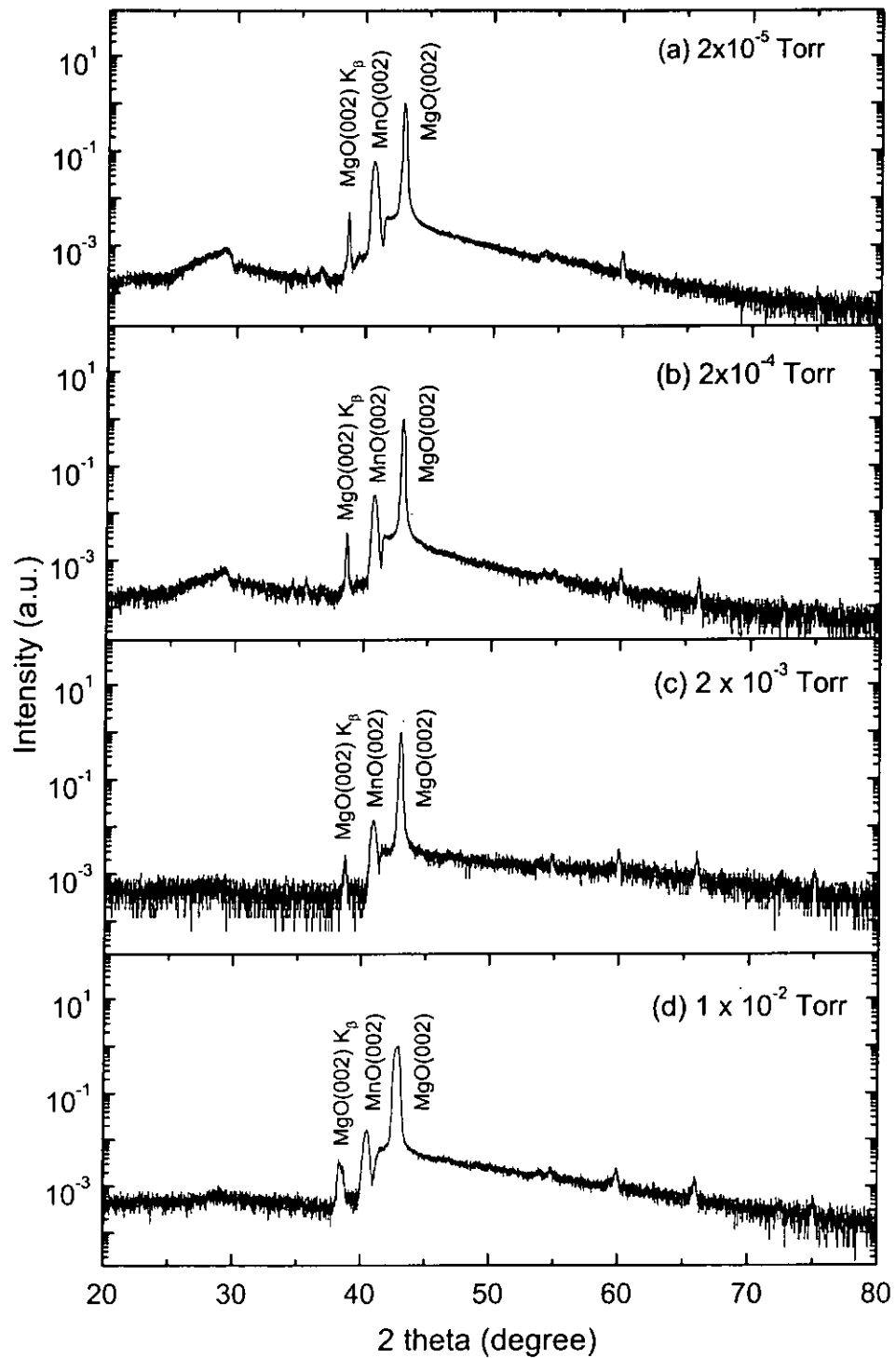
Figure 5.8 XRD patterns of MnO/MgO(001) with MnO deposited at (a) 2×10^{-5} Torr, (b) 2×10^{-4} Torr, (c) 2×10^{-3} Torr and (d) 1×10^{-2} Torr respectively.
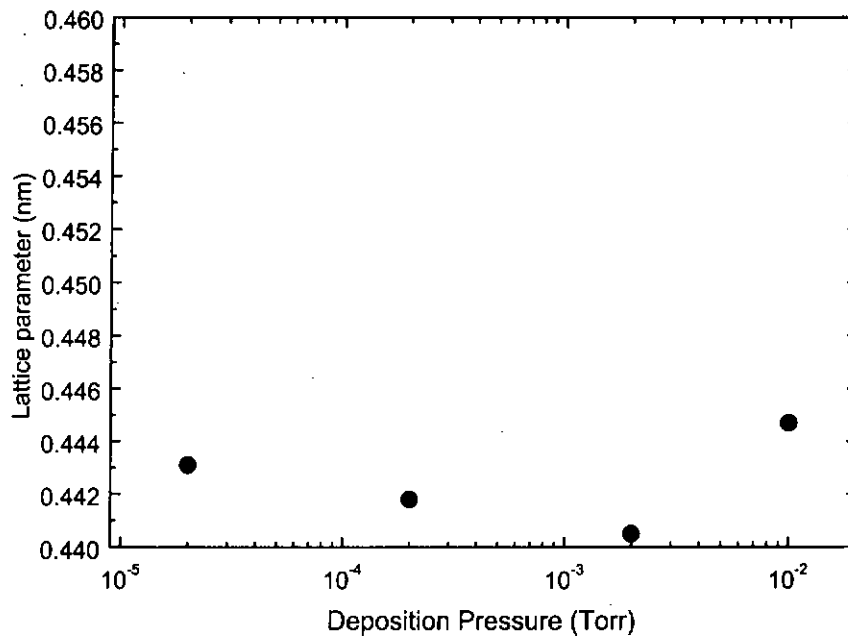
Figure 5.9 XRD peak intensity for MnO films deposited on MgO(001) substrate at 600 °C in different ambient pressures.
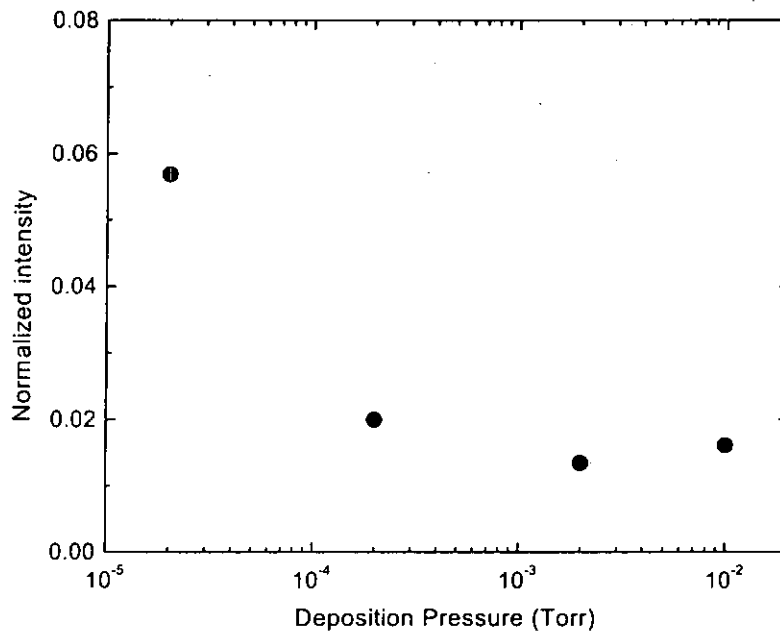
Figure 5.10 The out-of-plane lattice constant of MnO films deposited in different ambient pressures.
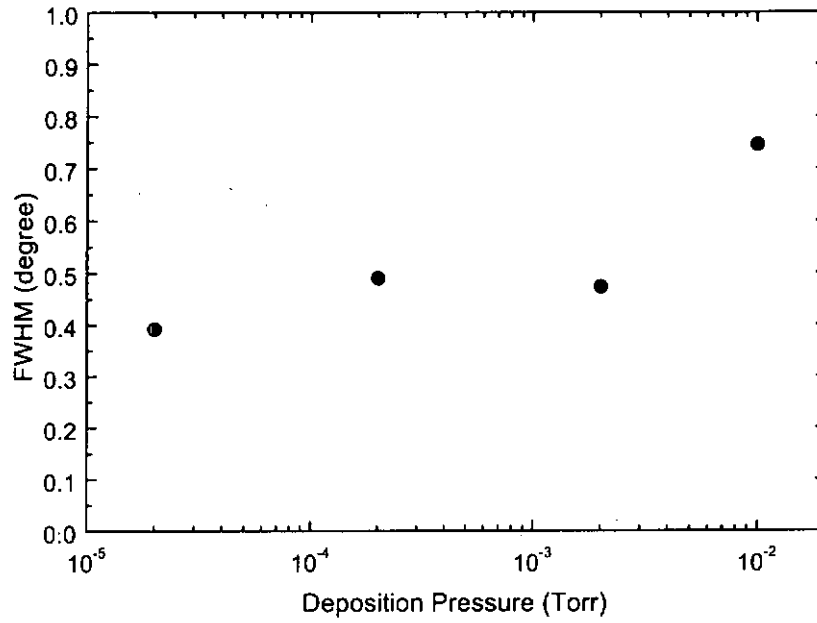
Figure 5.11The FWHM of rocking curve on the MnO(002) reflection measured for the MnO layers deposited on MgO(001) substrates in different ambient pressures.

## 5.4 Electrical characterization

5.4.1 Resistance-Temperature measurement

In general, metal oxides are bonded by ionic interactions between the metal and oxygen atoms and are expected to be insulators. The presence of defects, such as oxygen vacancies or impurity atoms, can substantially affect the electric properties, especially in MnO.

MnO is a highly non-stoichiometric oxide. It is agreed that MnO always contains an excess of oxygen, the predominate defects being the doubly ionized manganese vacancies with oxygen ambient. So in the lattice, both Mn^{2+} ions and Mn^{3+} ions can be found. The motion of electron takes place by discrete jumps between these localized states (see Fig. 5.12). So, MnO is defined as a hopping semiconductor [Goodenough et al., 1971]. Although the defects concentration is high, the mobility is found to be very low. It may be influenced by the strong interactions with lattice phonons and with the magnetic moments of the other ions present. Such hopping process, however, is thermally activated so that the mobility increases exponentially with temperature. The characteristic of the small polaron carrier can be described by a linear plot of $\ln(\rho/T)$ against $1/T$ where this slope indicates the activation energy of hopping (E_H). Pai and Honig [Pai et al., 1981] made an attempt to obtain single crystals of high purity and perfection of MnO. They implied that the carrier form polarons with the very high hopping energy of 0.44 eV.

Equation for small polaron hopping is as follows,

Hopping conductivity: $\sigma = \dfrac{A}{T}\exp\left(-\dfrac{E_H}{kT}\right)$

where A is constant, E_H is hopping energy
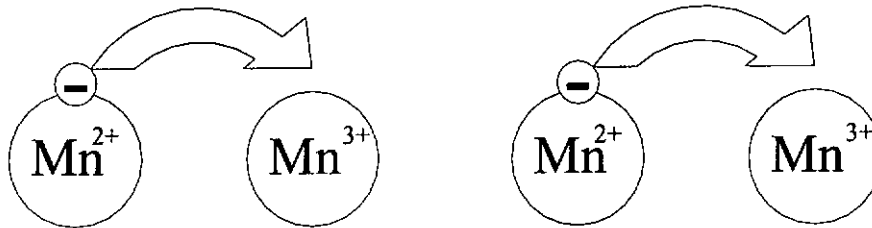
Figure 5.12 Schematic diagram of electron hopping in MnO.

The strong temperature dependent of resistivity of MnO enables it to be used as temperature sensors (thermistor). In this section, we show results of DC conduction measurements of the MnO thin film.

In order to measure the conduction properties, MnO film was deposited on the insulating substrate, MgO, which has resistivity of several orders of magnitude higher than MnO. The resistivity-temperature profiles in the range from room temperature to 500 K are presented in various plots. In general, the MnO films display semiconducting behavior (Fig. 5.13). The resistivity at room temperature is found to be 70 MΩ cm, which is much smaller than bulk samples of 1000 MΩ cm. In Fig. 5.14, it shows a linear relation of ln(ρ/T) against 1/T. The conduction of MnO is therefore agreed with the small polaron hopping model. From the slope of this curve, it indicates an activation energy for electron hopping of 0.51 eV. This is significantly larger than the value of 0.44 eV reported by Pai [Pai et al., 1981].
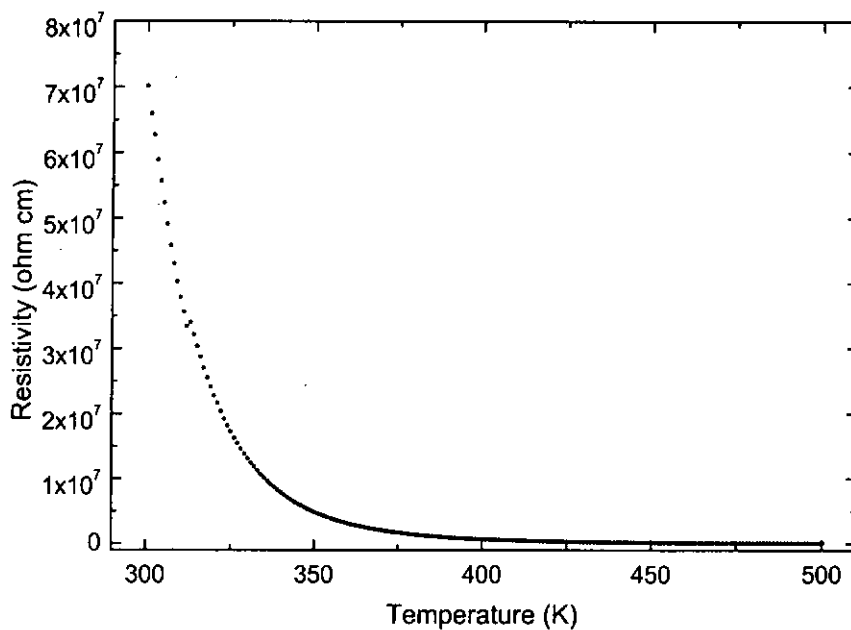
Figure 5.13 Resistivity against temperature of the MnO films grown at 600 °C under high vacuum of 2×10^{-5} Torr.
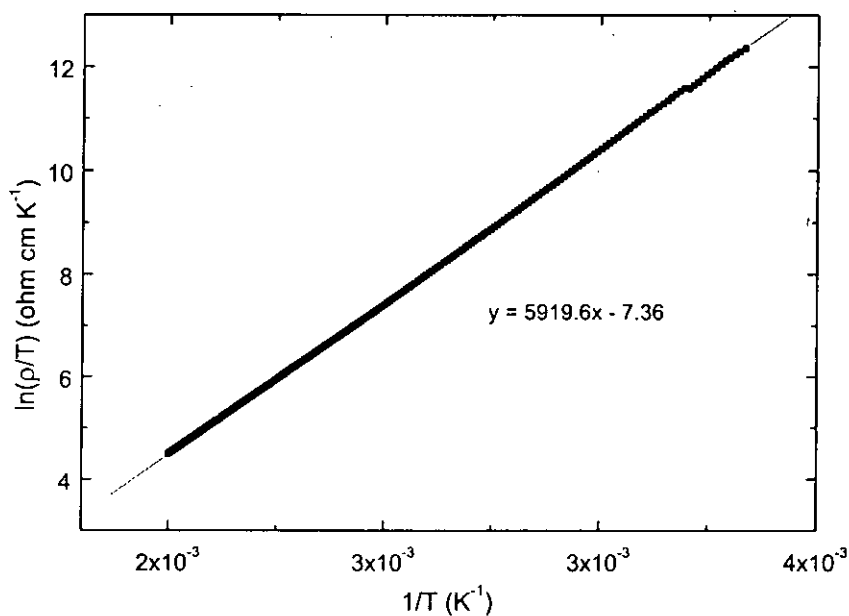
Figure 5.14 The $\ln(\rho/T)$ against $1/T$ plots of high precision resistivity-temperature data between 300 K and 500 K.

5.4.1(b) Deposition pressure dependence

In the present work, the effect of deposition pressure of MnO films on the electrical conduction properties was studied. The samples were deposited at 600 °C substrate temperature with a film thickness of about 250 nm.

The surface resistivity of the MnO thin films are quite sensitive to the deposition pressure. In Fig. 5.15, it shows room temperature resistivities of 5.4 MΩ cm, 30.0 MΩ cm, 51.7 MΩ cm and 67.8 MΩ cm for films prepared in 1×10^{-2} Torr, 1×10^{-3} Torr, 1×10^{-4} Torr and 2×10^{-5} Torr, respectively. Apparently, the room temperature resistivity decreases monotonously with increasing deposition pressure. A change of more than one order of magnitude in resistivity is observed over this deposition pressure range.
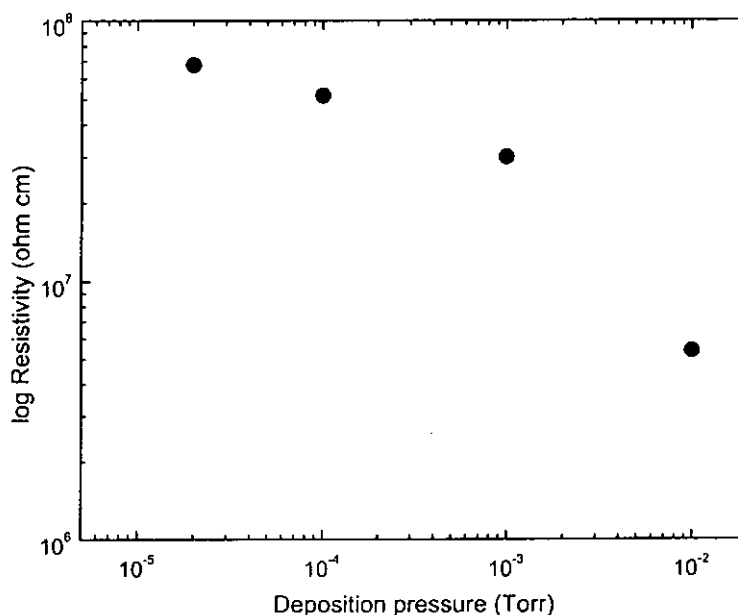
Figure 5.15 The room temperature-resistivity measured for the MnO films deposited at 600 °C with different deposition pressures.
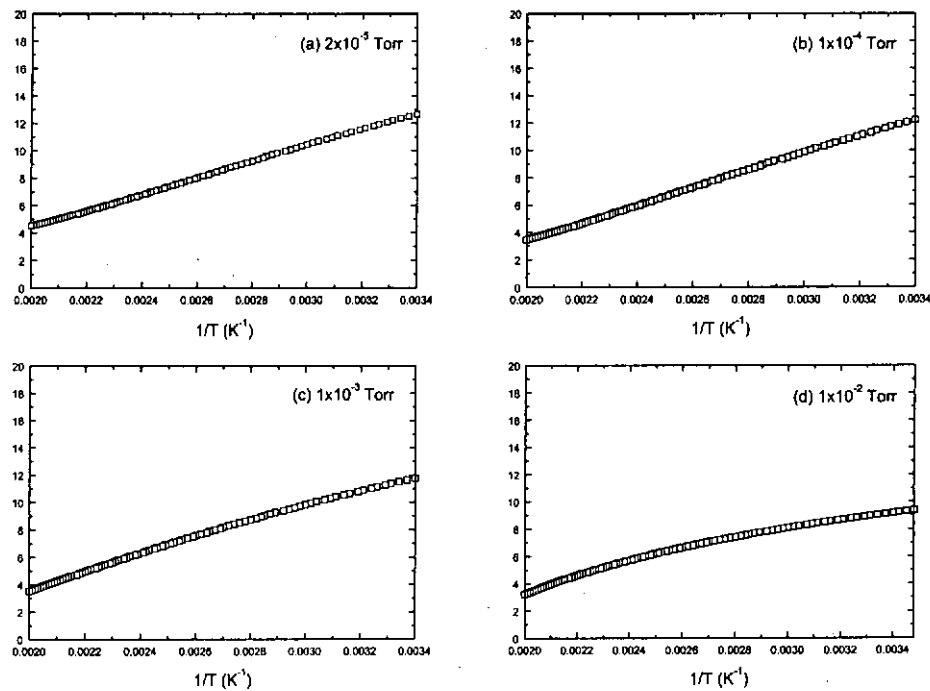
Figure 5.16 The ln(ρ/T) against 1/T plots of resistivity-temperature data between 300 K and 500 K, for the MnO films deposited on MgO substrate at 600 °C with different deposition pressures (a) 2x10⁻⁵ Torr, (b) 1x10⁻⁴ Torr, (c) 1x10⁻³ Torr and (d) 1x10⁻² Torr.

Fig. 5.16 shows the temperature dependence of resistivity for epitaxial MnO films grown at 600 °C with different deposition pressures. All samples show semiconducting transport behavior over the whole range of 300 K to 500 K. The non-linear lines appear in the Arrhenius plot of Fig. 5.16(c) and Fig. 5.16(d) indicate that the MnO films no longer obey the small polaron-hopping model when the deposition pressure is higher than 1×10^{-4} Torr. It also shows that the activation energy is lower at the low temperature region for samples grown at higher deposition pressure.
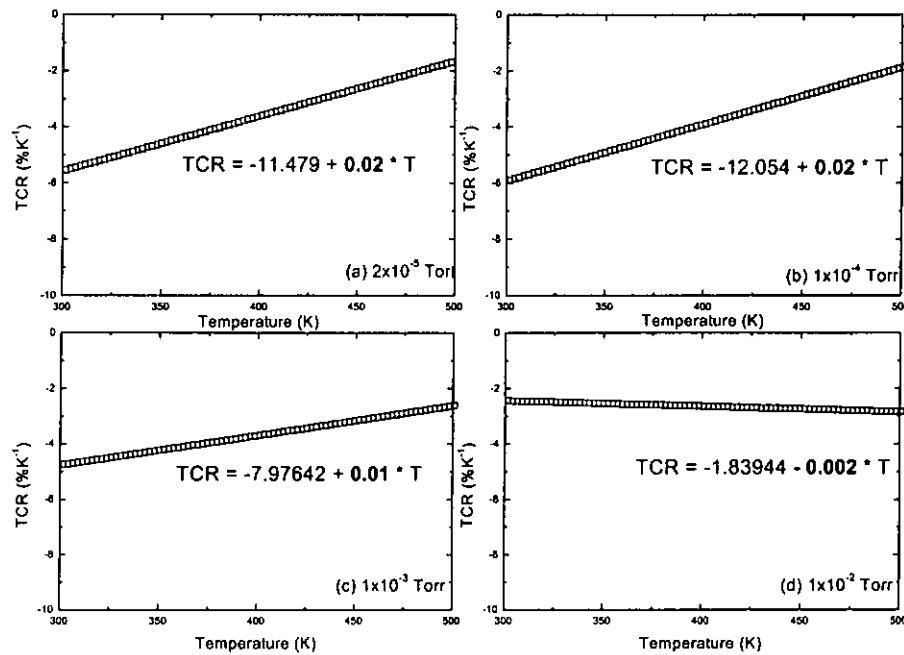
Figure 5.17 Plots of temperature coefficient of resistance with temperature at different deposition pressures (a) 2×10^{-5} Torr, (b) 1×10^{-4} Torr, (c) 1×10^{-3} Torr and (d) 1×10^{-2} Torr.

To qualify the temperature response of MnO thin film resistivity to be useful for temperature sensors, we have to consider its temperature coefficient of resistance. The temperature coefficient of resistance (TCR), α, is defined as the ratio of the rate of change of resistance with temperature to the resistance at a specified temperature. It is expressed mathematically as:

$$\alpha = \frac{1}{R} \times \frac{dR}{dT}$$

The results of our measurement are summarized in Fig. 5.17. The TCR at room temperature are -5.5, -5.9, -4.7 and -2.4 % K^{-1} for the MnO films deposited in 2×10^{-5}, 1×10^{-4}, 1×10^{-3} and 1×10^{-2} Torr, respectively. The temperature dependence of the TCR parameter is different from the case with different deposition pressures also.

5.4.2 Antiferromagnetic transition

In Chapter 4, the dielectric properties of MnO have been determined from the heterostructures of Pt/MnO/TiN/Si(001). But now we put some effort on studying the dielectric abnormally effect of MnO magnetic transition.

Electron- correlation effects in systems with thin film geometry have gained increasing interest in condensed matter physics. In particular, there has been intense research effort on studying the thermodynamic phase transition to a symmetry-broken state below a critical temperature. Magnetic transition of MnO is one of the typical examples. MnO bulk samples have been reported to undergo a first order paramagnetic to antiferromagnetic phase transition as it cooled through the Néel temperature (118K). This transition is accompanied by a trigonal distortion which contracts along the [111] axis, thus distorting the high temperature rocksalt structure. Anomalous dielectric properties of MnO at near the magnetic ordering temperature was perhaps first indicated in the work by Seehra [Seehra et al., 1981] where a significant decrease in the dielectric constant of MnO was recorded as the sample was cooled through its Néel temperature.

In our studies, we have performed a similar measurement but on MnO in thin film form. Generally, below the Néel temperature, MnO will have two kinds of domain (see Fig. 5.18): T domains, resulting from twinning of the crystal since there are four equivalent [111] contraction axes, and S domains because of the threefold degeneracy of the easy axes in the [111] planes. Recent studies of the magnetic susceptibility of bulk MnO have shown that a small stress applied along a [111] axis, as MnO is cooling through Néel temperature, is enough to completely inhibit twinning and remove the T domains [Seehra et al., 1981]. So, the [111] MnO film epitaxial growth may have similar effect by applying symmetry breaking field from the substrate effect.
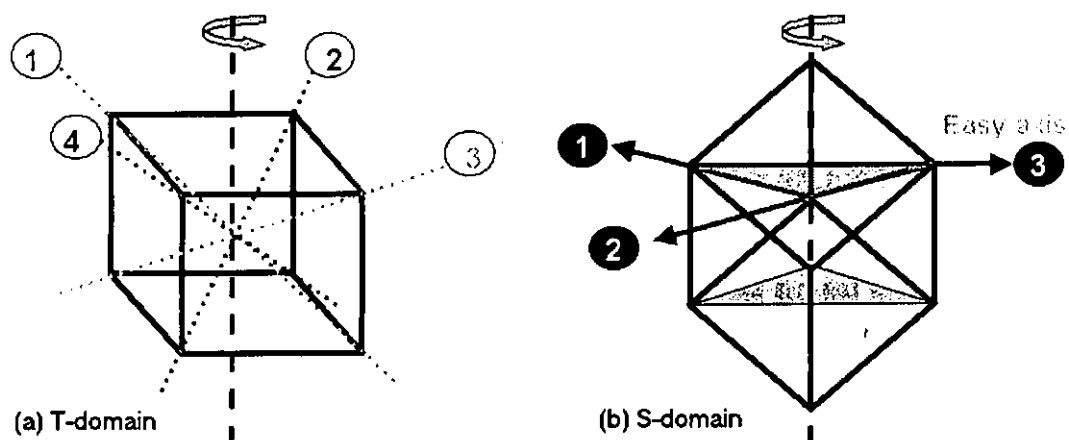
(a) T-domain   (b) S-domain

Figure 5.18 (a) T-domain and (b) S-domain of MnO below Néel temperature.

Experiment was done by depositing MnO film on TiN buffered MgO(111) substrate. MgO and TiN have rocksalt structures. The lattice parameters of MgO (0.421 nm) and TiN (0.425 nm) have a lattice mismatch of only 0.7 %, so epitaxial growth is favored.

5.4.2(a) Fabrication of Au/MnO/TiN/MgO(111) heterostructure

MgO substrate was ultrasonically cleaned in acetone solution. A KrF excimer laser was used to ablate stoichiometric hot pressed TiN target at an energy density of 5 J cm^{-2}. The deposition was carried out at 650 °C under 2×10^{-5} Torr ambient pressure. MnO was subsequently deposited for 20 minutes at 600 °C. The pressure of 2×10^{-5} Torr was maintained during the whole deposition process. MnO films of thickness of 170 nm were grown. They were then coated with top gold electrodes of an area of 0.01 mm^2. The films were structurally characterized using X-ray diffraction (XRD).

5.4.2(b) Structural characterization of Au/MnO/TiN/MgO(111)

The XRD θ-2θ profile of the Au/MnO/TiN/MgO(111) heterostructure for the MnO grown at 600 °C is shown in Fig. 5.19. Diffraction peaks of MnO(111) and TiN(111) are identified. No trace of other peaks is present. Fig. 5.20 and Fig. 5.21 show the ω-scan rocking curves of MnO(111) and TiN(111) peaks, respectively. The full width at half maximum (FWHM) corresponding to TiN and MnO are 0.79° and 0.70°, respectively. This indicates the films are highly oriented. The (111) plane separation of MnO was found to be 0.253 nm. This value is similar to that of MnO film grown on MgO(001). The characteristics of in-plane alignment were obtained by 360° Φ-scan and the result is shown in Fig. 5.22. Three sharp peaks are obtained at 120° interval, showing a clear 3-fold symmetry of a cubic structure in [111] direction. It suggests that the heterostructure is epitaxially grown on the MgO(111) substrate with an excellent crystalline structure.
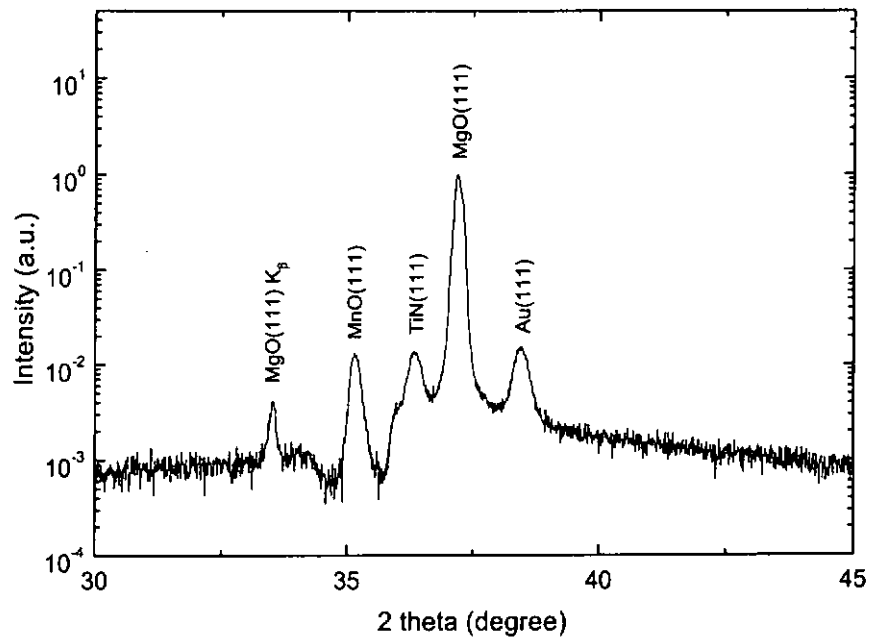
Figure 5.19 XRD pattern of Au/MnO/TiN/MgO(111) heterostructure.
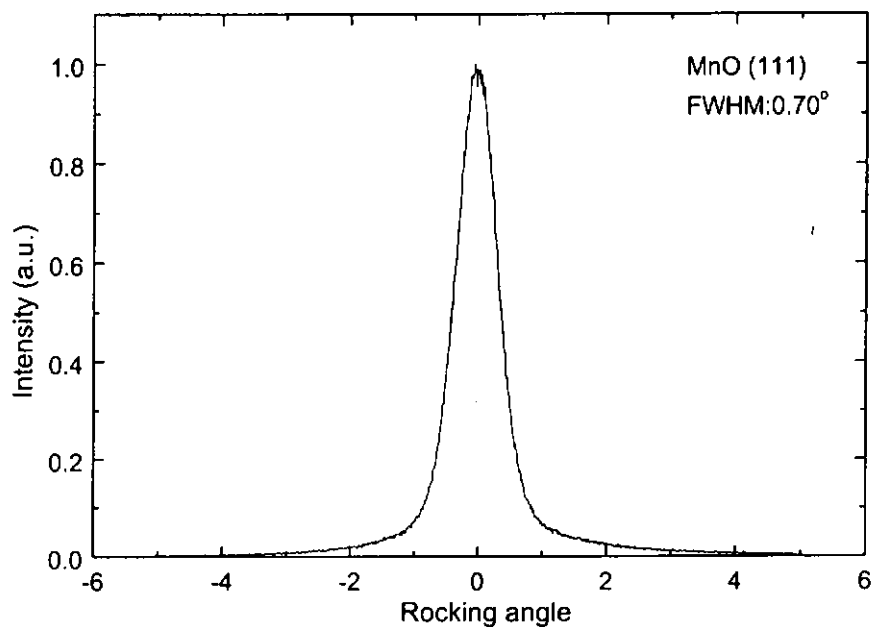
Figure 5.20 XRD rocking curve of MnO(111) peak exhibiting a FWHM of 0.70°.
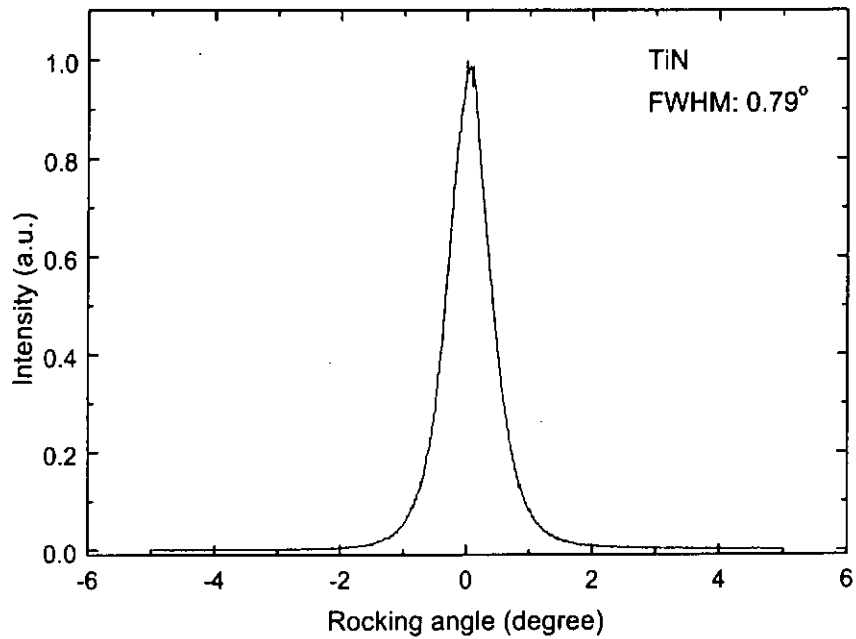
Figure 5.21 XRD rocking curve of TiN(111) showing a FWHM of 0.79°.
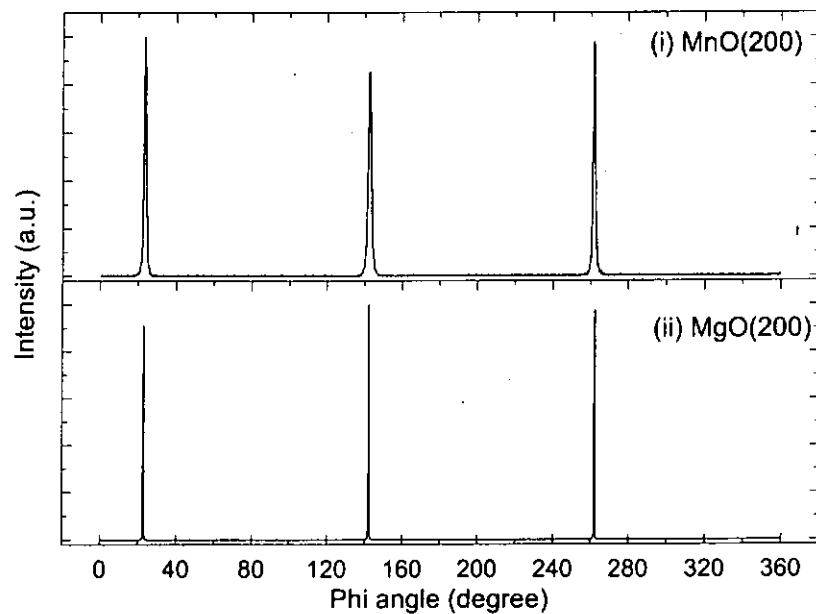
Figure 5.22 The Φ-scan of the (i) MnO(200) and (ii) MgO(200).

5.4.2(c) Dielectric Measurement

Regarding to dielectric–temperature measurement, 1 mm x 1 mm top Au electrodes were deposited on the MnO layer by PLD via a patterned mask. Thickness of the MnO layer was determined as 170 nm. In the temperature range between 78 K and 310 K, both the dielectric constant and dielectric loss are frequency independent at up to the maximum available frequency of 10 MHz. This is indicated by measurements at several representative temperatures. Therefore the detailed temperature–dependent data within the range of 78 K to 310 K was taken at one fixed frequency of 2 MHz. The room temperature dielectric constant of 19.2 (dissipation factor ~0.17) at 2 MHz is larger than the 16.19 (dissipation factor ~0.04) measured from Pt/MnO/TiN/Si(001) heterostructure. The temperature dependent dielectric constant for a [111] orientated MnO film over the temperature range of 78 K to 310 K is shown in Fig. 5.23. No noticeable drop in the dielectric constant within this temperature range is observed.

The absence of the magnetic transition in the [111] orientated MnO film may be induced by several factors. For example, internal strain caused by substrate mismatch and the precise stoichiometry of the films could play an important role. The XRD measurement of out-of-plane lattice constant of MnO and TiN gives 0.442 nm and 0.428 nm, respectively. It implies that the lattice mismatch of MnO and TiN is about 3 % with MnO being larger. The MnO crystal will expand in out-of-plane direction while the in-plane lattice is under contraction.
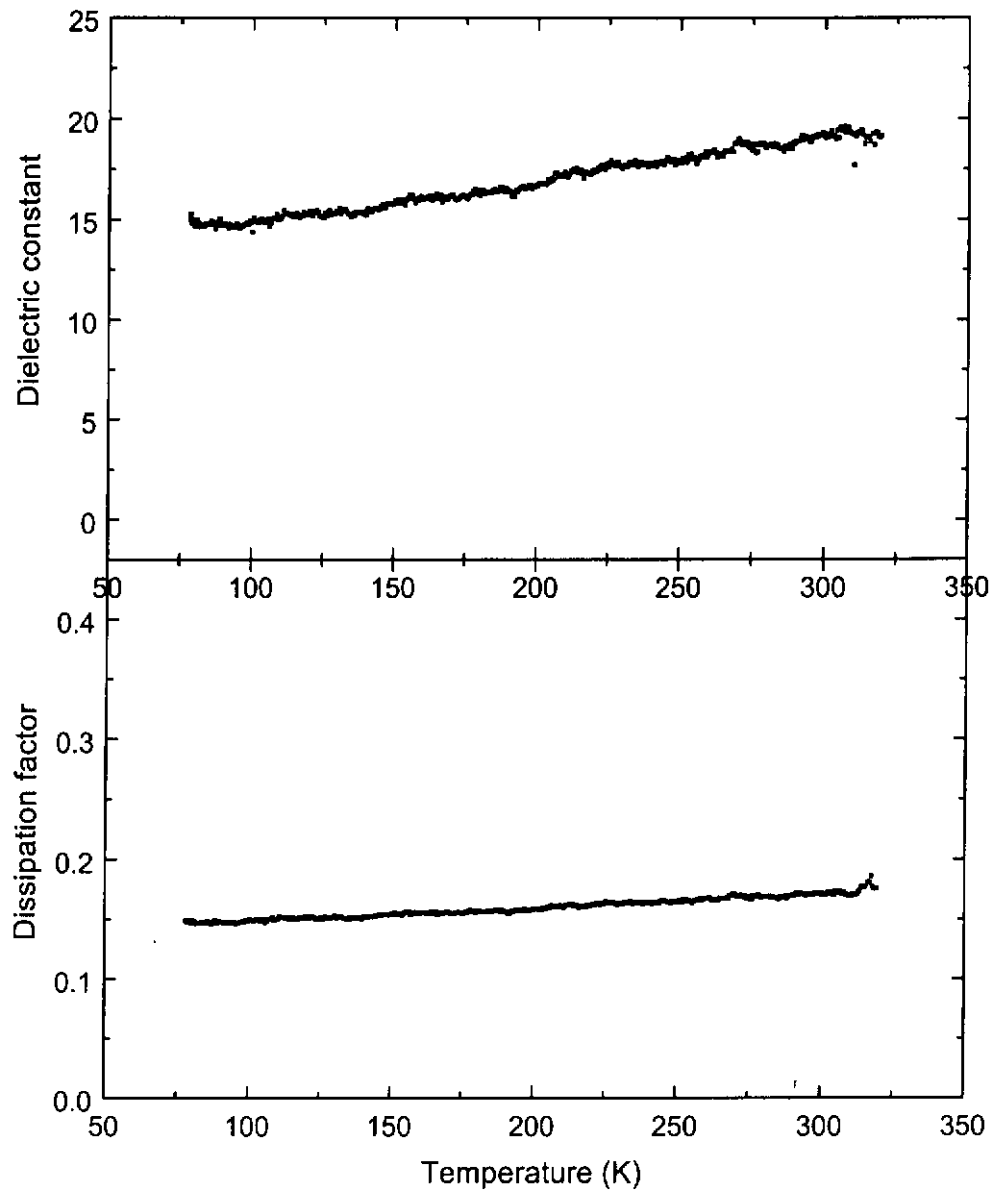
Figure 5.23 The dielectric constant and dissipation factor of MnO film for the heterostructure of Pt/MnO/TiN/MgO(111).

CHAPTER 6

Fabrication and characterization of $Mn_xCo_{1-x}O$ layer

6.1 Introduction

In the pervious two chapters, we have shown the fabrication of pure rocksalt MnO films on different substrates by PLD method. We have also demonstrated some structural and electrical measurements of these films. In this chapter, we describe work on the fabrication of cobalt doped MnO thin films. In the case of Mn^{2+} ion replaced by the Co^{2+} ion in the rocksalt monoxide lattice, a complete miscible solid solution can be formed [Passerini et al., 1929 and Hotzl et al., 1958]. The ease of miscibility of the MnO/CoO solid solution is greatly aided by their (1) small difference in atomic size, (2) same crystal structure, (3) similar electronegativities and (4) same valency. Such system of mixed monoxide is called isomorph. Isomorphous systems showing a linear relation of lattice parameter with their composition ratio is known as Vegard's law [Sury et al.,1998] (see Fig.6.1).

The mixed metal monoxide of composition $Mn_xCo_{1-x}O$ exists over the whole range of x from 0 to 1. This allows the material properties to be easily tailored to the task at hand. For example, an entire class of Fischer-Tropsch and oxidative-coupling catalysts relies on the chemical properties of $Mn_xCo_{1-x}O$ system [Keyser et al., 1998]. But in fact, more complex effects must be expected in this multicomponent system.

For example, their spin state polarization and potential applications in spintronics are

of major importance.
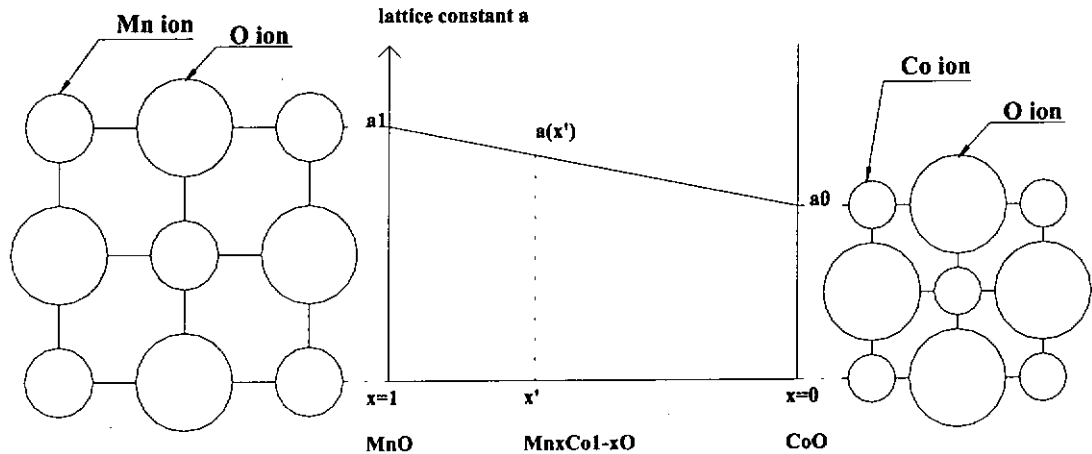
Figure 6.1 Schematic diagram shows the structural change of $Mn_xCo_{1-x}O$ according to the composition (x).

From a practical point of view, the MnO and CoO are defined as low mobility

hopping semiconductor. They exhibit negative temperature coefficient (NTC) of

electrical resistance over an extended temperature range. These two oxides and their

mixed metal oxide have been studied for uses as NTC thermistor. In addition, a

commercial infrared-sensitive thermistor, composed of MnO, CoO together with

NiO, was found to be a candidate for use as an atomic beam detector [Harvey et al.,

1983]. The thermistor is sensitive to atomic hydrogen, deuterium and nitrogen

without any reactivation treatment. It has been revealed that the sensitivity to atomic

species correlates to the oxide's electrical resistance and temperature coefficient

[Fujimori et al., 1993]. The related researches are mainly based on the sintered bulk

oxide samples. However, the change of electrical resistance in the sensing process only takes place at the surface, so that devices for atomic-beam detection should have a large surface-to-volume ratio. Therefore the metal oxides in thin film form, especially with a good crystalline structure, are preferable in such devices.

In previous chapters, we have mentioned that pulsed laser deposition (PLD) is a versatile method for the fabrication of mixed metal oxide with good stoichiometry. The present study is aimed at using PLD method to fabricate epitaxial rocksalt $Mn_xCo_{1-x}O$ thin films on TiN buffered silicon and on MgO substrates. The structural and electrical properties of the as-grown films are also presented.

6.2 Brief description of atomic beam detector

The mechanism of atomic beam detector is quite simple. It is related to the atom-surface reaction. An incident beam of atom is adsorbed on the surface of the metal oxide surface. The adsorbed atoms then move around on the surface. They incidentally collide with one another and recombine to form a molecule. At the same moment excess energy is released. When being desorbed, the molecule donates the energy surplus to the oxide. The temperature of the surface region of the metal oxide will increase slightly. Then, the temperature increase near the surface will cause the increase of surface electric conduction. Therefore, if a sample has a high electric resistivity, this change in surface conduction can give rise to a rather considerable change in the electron conductivity of the specimen as a whole. This implies a high sensitivity detection ability. Therefore a sample having a large thermal coefficient and a high electric resistance should exhibit a large sensitivity to atomic beams.

6.3 Preparation of $Mn_xCo_{1-x}O$ target

The ceramic targets of mixed metal oxide ($Mn_xCo_{1-x}O$) were prepared by standard solid-state reaction from high purity powders of constituent oxides (MnO_2 – 99.9 % purity, Co_3O_4 –99.99 % purity). The correct composition of the powders was weighted and mixed together. They were then grounded by ball-milling machine. The final mixture of powder was calcined at 900 °C for 5 hours in air. Afterward it was pressed into pellets. The pellets were sintered at 1100 °C for 15 hours. The final targets were analyzed by a standard X-ray powder diffractometer. The composition of mixed metal oxide targets $Mn_xCo_{1-x}O$ was determined by EDX and summarized in Table 6.1.

Target Set	Mn atomic ratio	Co atomic ratio
1	100 %	0 %
2	77.26 %	22.74 %
3	57.35 %	42.65 %
4	43.47 %	56.53 %
5	31.47 %	68.53 %
6	18.65 %	81.35 %
7	0 %	100%

Table 6.1 The composition of $Mn_xCo_{1-x}O$ targets verified by EDX.

From the XRD profile shown in Fig. 6.2, the pure manganese oxide target and pure cobalt oxide target were identified in the phase of Mn_3O_4 and Co_3O_4, respectively. Both targets were found to be in spinel structure. The mixed metal oxide targets were also well crystallized and suitable for preparing thin films by PLD.
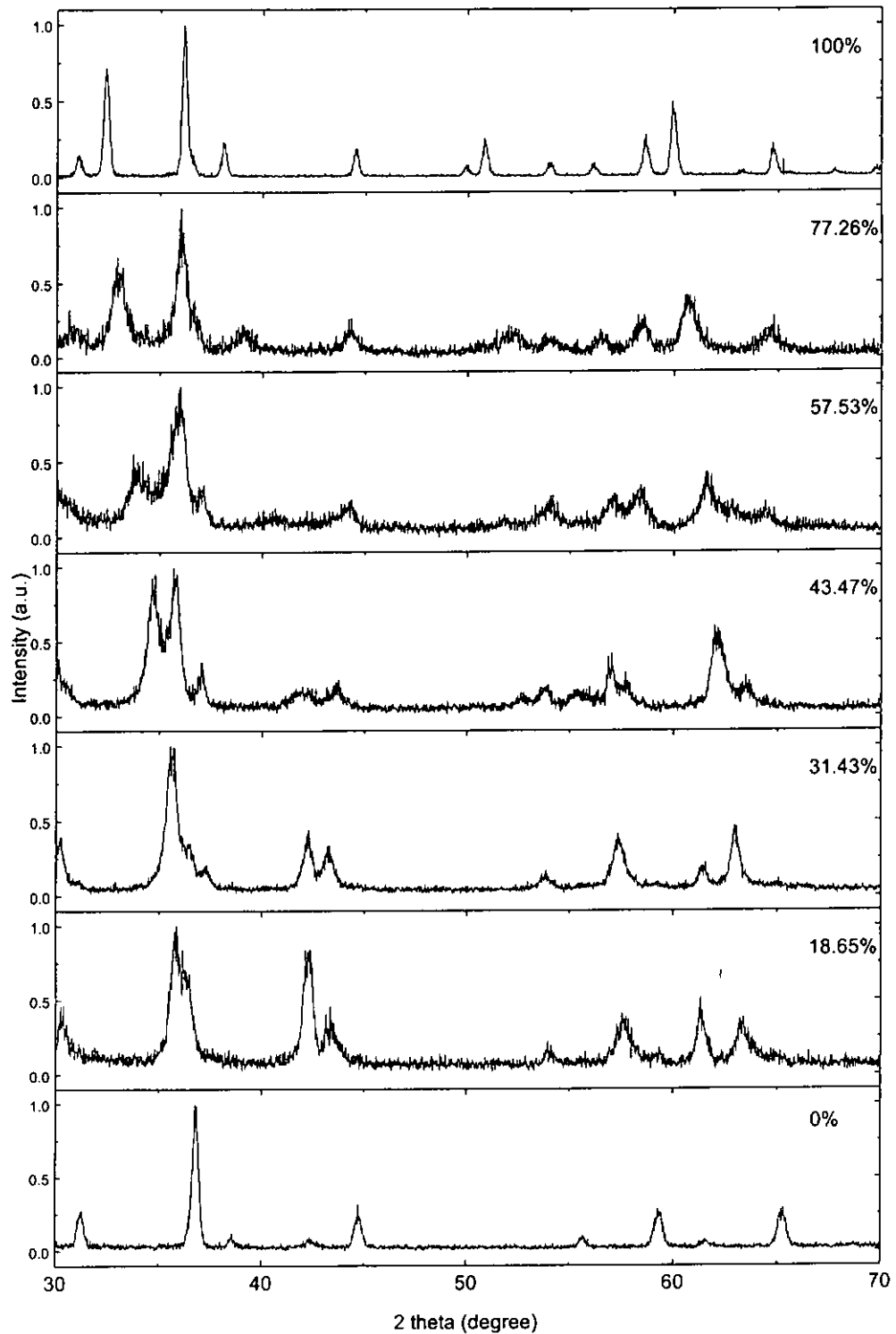
Figure 6.2 XRD patterns for the mixed metal oxide ($Mn_xCo_{1-x}O$) targets with different composition x.

6.4 Fabrication of $Mn_xCo_{1-x}O/TiN/Si(100)$ heterostructure

6.4.1 Deposition of $Mn_xCo_{1-x}O$ on TiN buffered Si(001)

The TiN buffered Si(001) substrates were prepared by the same method as mentioned in Section 4.2. The mixed metal oxide ($Mn_xCo_{1-x}O$, x range from 0.1865 to 1) targets were irradiated with KrF excimer laser, which provides 200 mJ pulses of 25 ns at a 10 Hz repetition rate. The laser beam was focused through a window to give an on-target laser energy density of 4 J cm^{-2}. The emitted material was deposited onto TiN buffered Si(001) substrate located at 5 cm away from the target. The substrate temperature was held at 600 °C, and the depositions were carried out at 2×10^{-5} Torr ambient pressure. A 30 minutes of deposition time produced an oxide film of about 250 nm thick.

6.4.2 Structural characterization by XRD

Detailed XRD studies were used to examine the alignment of the films in the direction normal to the film and the in-plane mosaicity. Fig. 6.3 shows θ-2θ scans of the $Mn_xCo_{1-x}O$ films deposited on epitaxial TiN/Si(001) substrate. It can be seen that the (002) peaks of all $Mn_xCo_{1-x}O$ films are clearly discernable. The lattice constants of these films vary from 0.426 nm to 0.444 nm. Thin films of solid solution of CoO in MnO follow the Vegard's law of linear dependence of the lattice parameter on concentration. Results are shown in Fig. 6.4.

Rocking curve measurements were performed to evaluate the mosaic spread of the crystalline in the films. The corresponding full width at half maximum (FWHM) values are summarized in Fig. 6.5. In general, good alignment of the crystallites for the $Mn_xCo_{1-x}O$ films are obtained. Nevertheless, it shows deterioration in the crystal orientation at high cobalt content in the films. It is somewhat unexpected as the lattice mismatch between $Mn_xCo_{1-x}O$ and TiN is less for small x.
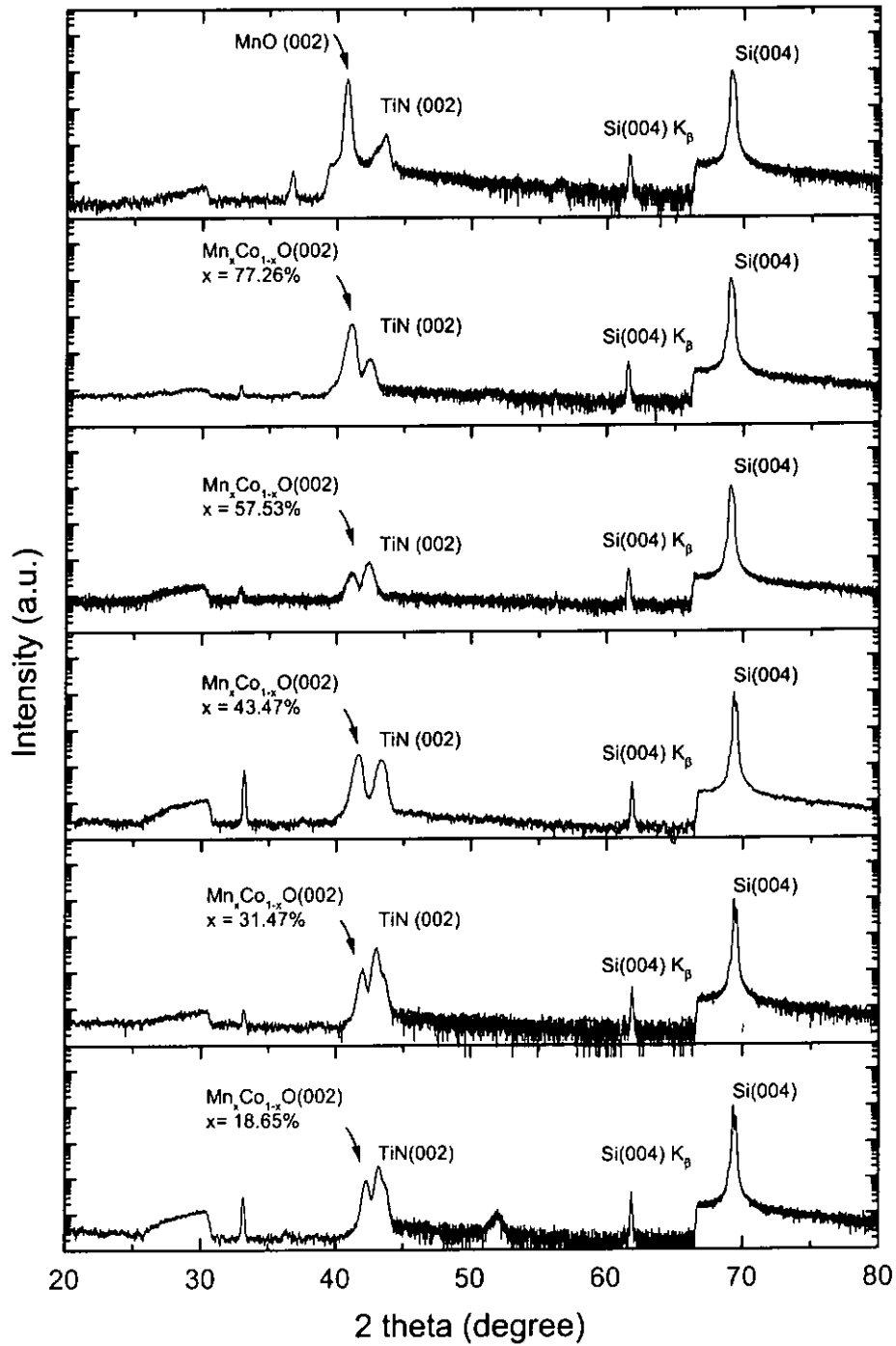
Figure 6.3 XRD patterns for $Mn_xCo_{1-x}O/TiN/Si(001)$ deposited with different compositions from x=0.1865 to x=1.
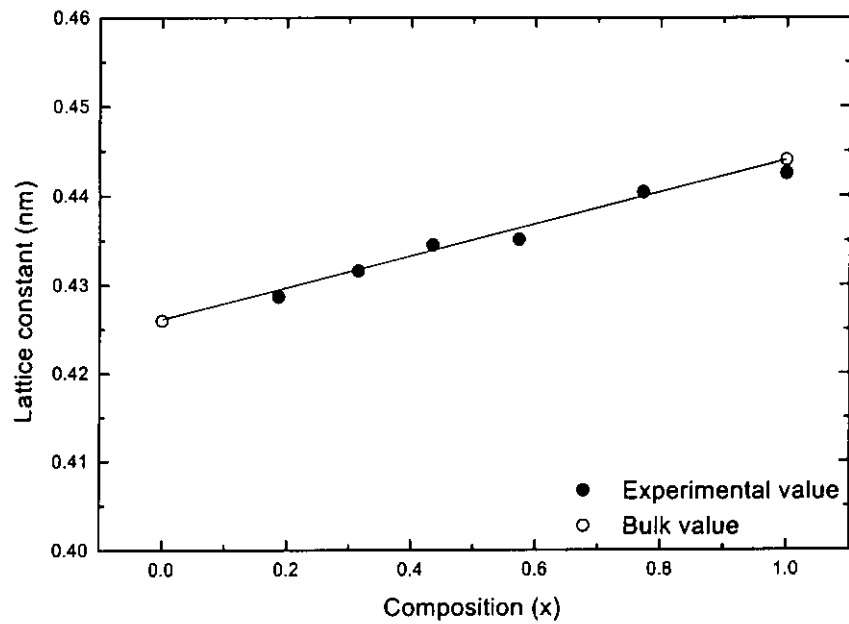
Figure 6.4 Variation of lattice parameter of $Mn_xCo_{1-x}O$ thin films grown on TiN/Si(001) substrates with MnO content.
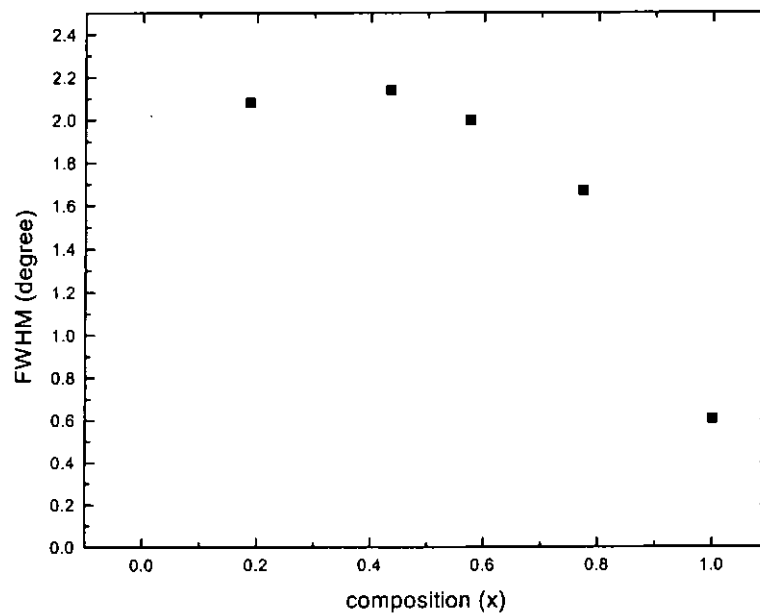
Figure 6.5 The FWHM of $Mn_xCo_{1-x}O$ films deposited on TiN buffered Si(001) substrates at 600 °C in $2x10^{-5}$ Torr.

6.4.3 Surface morphology

Although the XRD data shows a generally good crystalline structure, the film morphology and texture also need to be evaluated. The as-grown $Mn_xCo_{1-x}O$ films are optically clear with a greyish-green tint that darkened slightly as x decreases. Fig. 6.6 shows the SEM micrographs of the mixed metal oxide $(Mn_xCo_{1-x}O)$ films prepared on TiN buffered silicon. All the samples were prepared at 600 °C in $2x10^{-5}$ Torr of air ambient.

From the surface morphology profile of the $Mn_xCo_{1-x}O$ films, crack-free surfaces can be seen. However, from Fig. 6.7 to Fig. 6.10, the prominent presence of small particles is observed. The size of these particles increases with cobalt content. The particles range from about 20 nm (x = 77.26%) to 200 nm (x = 18.65%). The occurrence of these particles may due to phase segregation at high Co content. Indeed their presence is the cause of degradation in crystallinity of $Mn_xCo_{1-x}O$ as mentioned before.
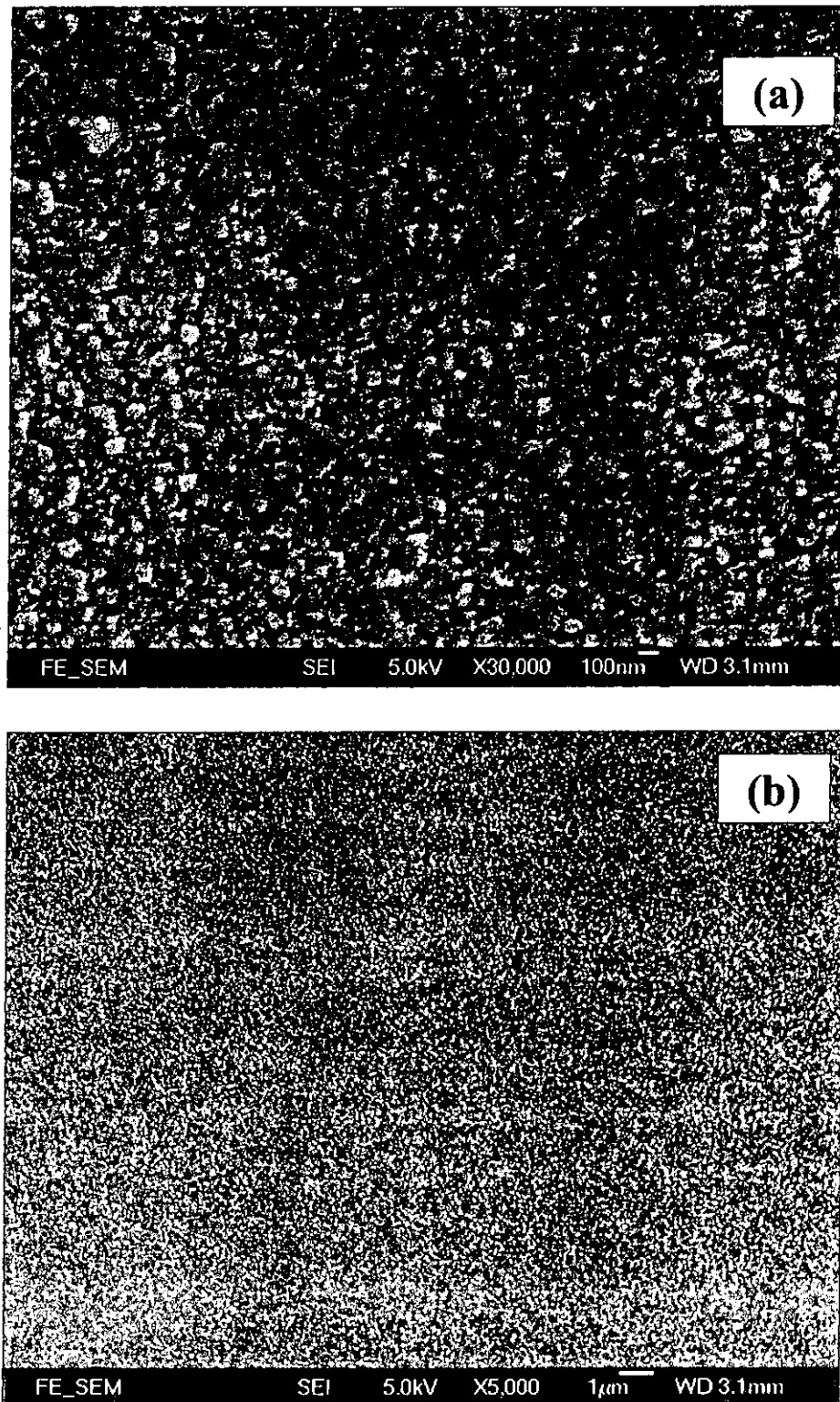
Figure 6.6 SEM images of surface morphology of MnO thin film deposited at 600 °C in 2×10^{-5} Torr.

Figure 6.7 SEM images of surface morphology of $Mn_xCo_{1-x}O$ thin film (x = 77.26 %) deposited at 600 °C in $2x10^{-5}$ Torr.
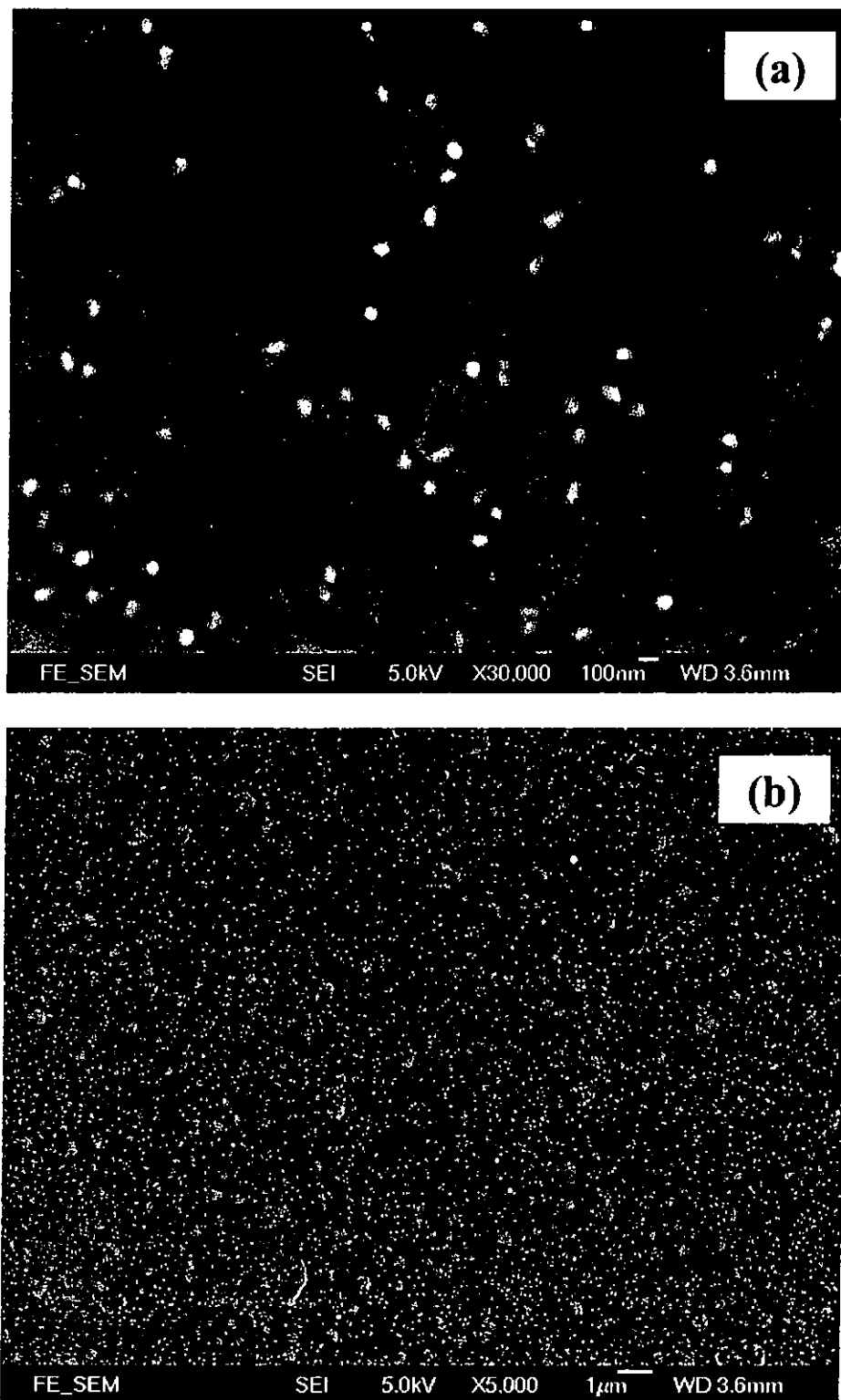
Figure 6.8 SEM images of surface morphology of $Mn_xCo_{1-x}O$ thin film (x = 43.47 %) deposited at 600 °C in $2x10^{-5}$ Torr.
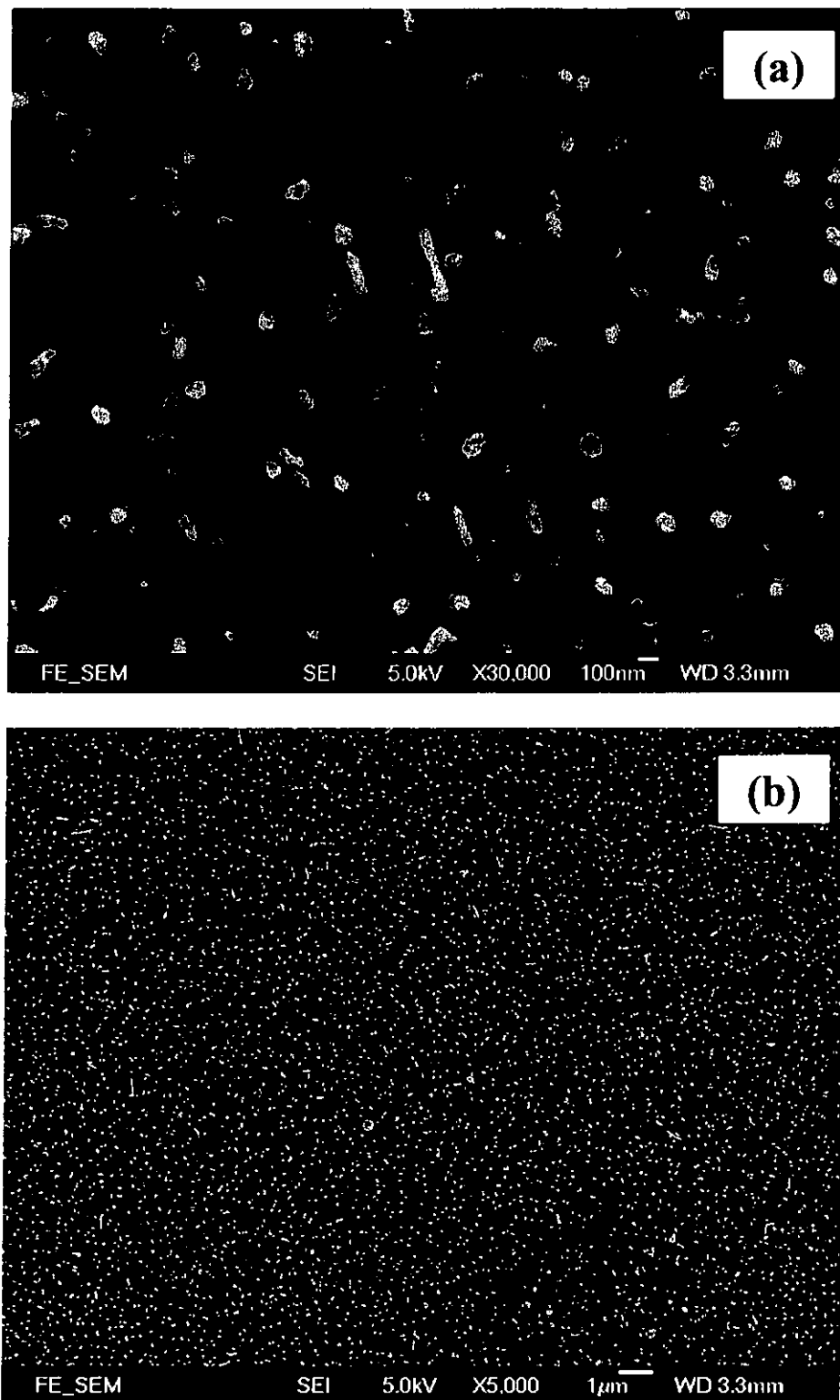
Figure 6.9 SEM images of surface morphology of $Mn_xCo_{1-x}O$ thin film (x = 31.47 %) deposited at 600 °C in $2x10^{-5}$ Torr.

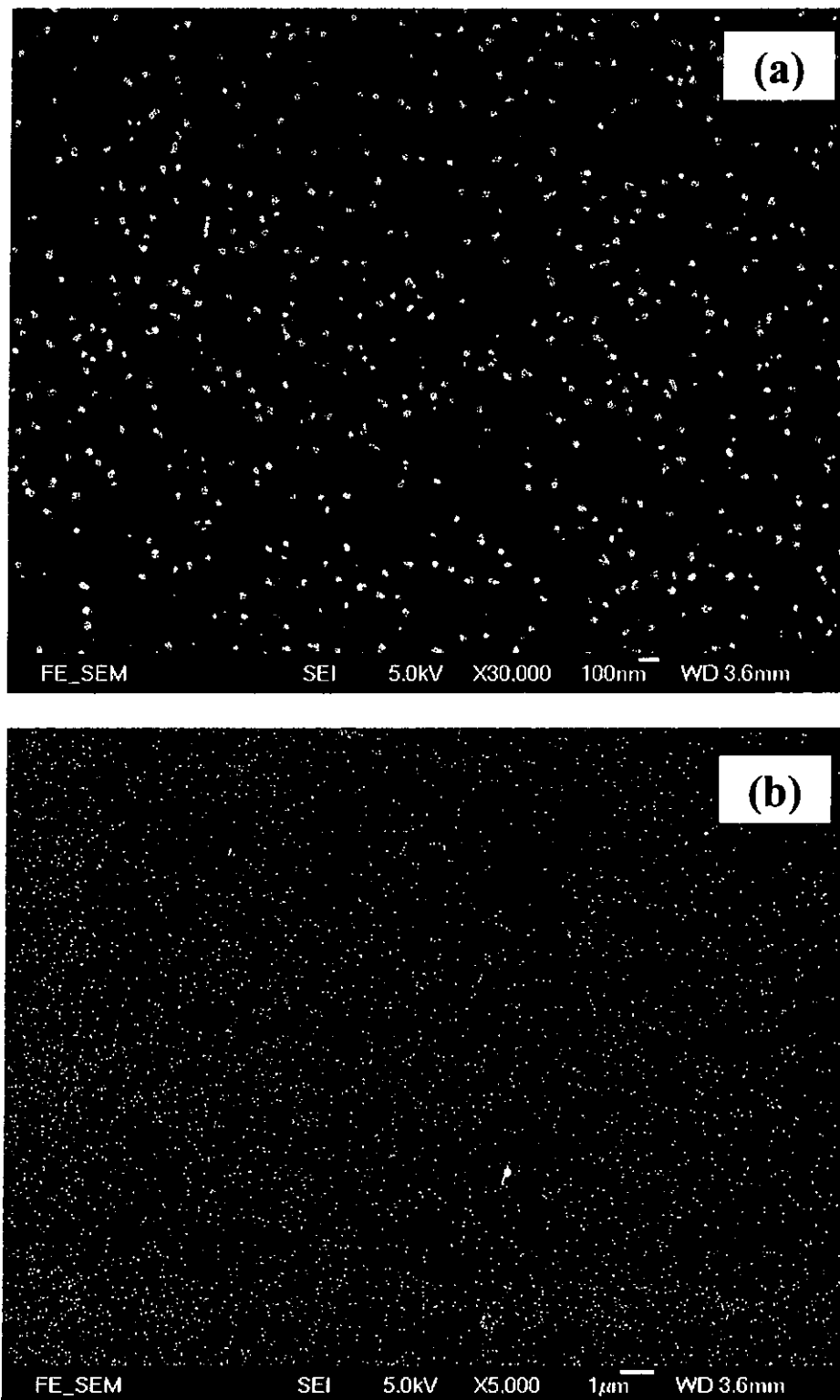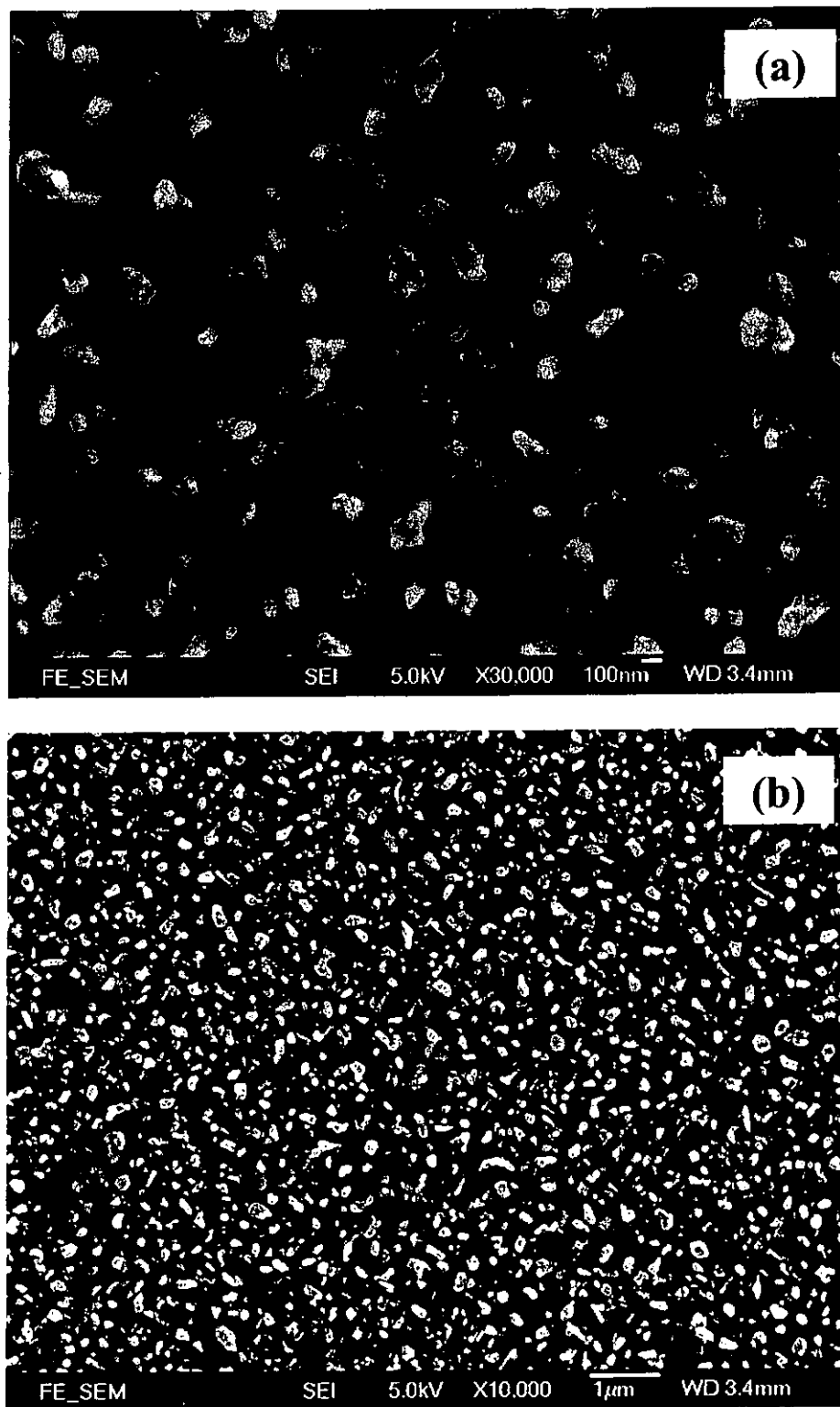Figure 6.10 SEM images of surface morphology of $Mn_xCo_{1-x}O$ thin film (x = 18.65 %) deposited at 600 °C in $2x10^{-5}$ Torr.

6.4.4 Leakage current density

The capacitor structure of $Pt/Mn_xCo_{1-x}O/TiN/Si(001)$ was fabricated in subsequent experiments. The deposition condition for TiN was the same as those described in Section 4.2. All $Mn_xCo_{1-x}O$ films with about 250 nm thickness were deposited on TiN/Si(001) substrates at 600 °C and 2×10^{-5} Torr ambient pressure.

The leakage current density versus applied electric field for the capacitor is shown in Fig. 6.11. By comparing the composition in the oxide films, the leakage current density of the films with higher manganese content is much lower. It is clearly shown in Fig. 6.12 for leakage current density obtained at 2×10^4 V cm^{-1}. The leakage current density in low electric field was selected for comparison because of the small breakdown field of cobalt-rich samples. From Fig. 6.12, the larger leakage current density is probably due more to the bad crystallinity of the oxide film than the intrinsic properties of the mixed metal oxide itself. Besides, the existence of undesirable particles may cause some local thinning or electrically short circuiting the oxide films.
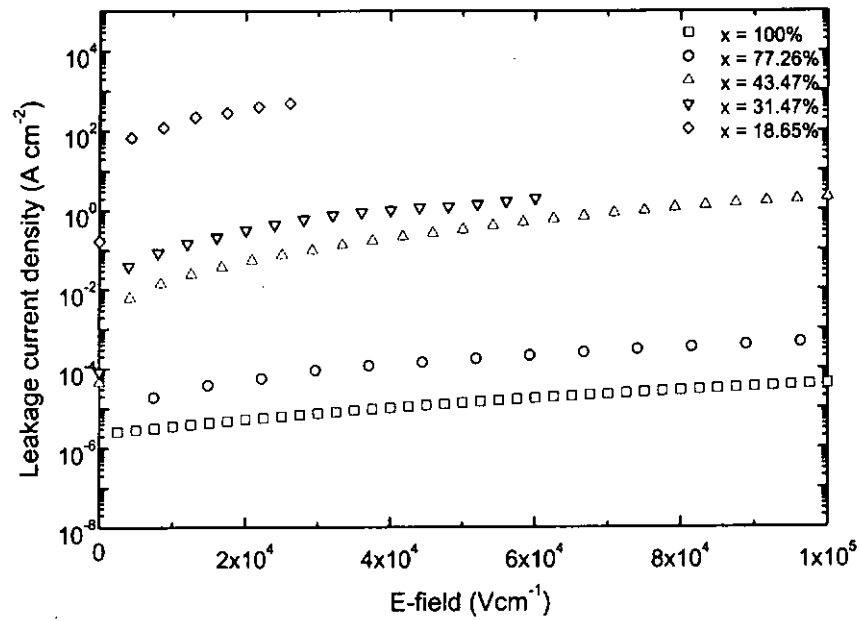
Figure 6.11 The J-E characteristic curves for the 250 nm Mn$_x$Co$_{1-x}$O films prepared at 600 °C in 2x10^{-5} Torr.
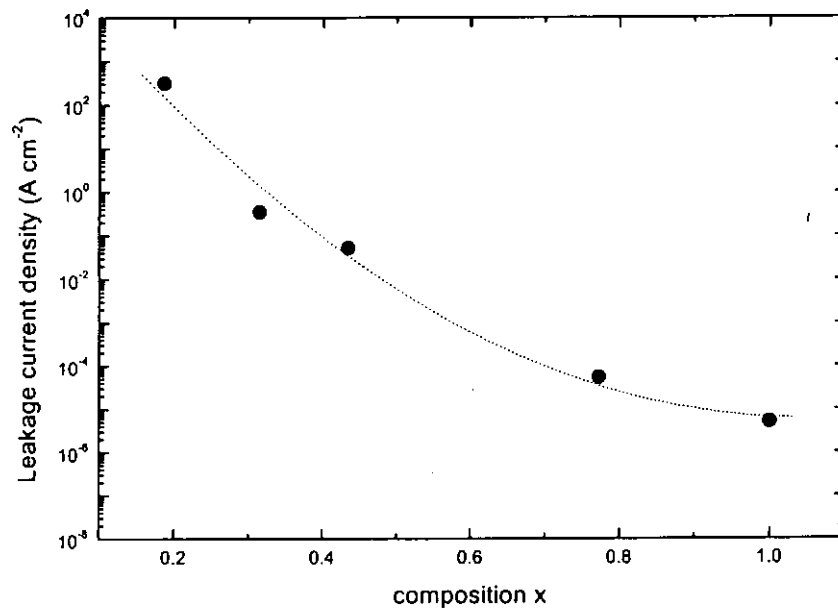
Figure 6.12 Plot of leakage current density versus the composition (x) of Mn$_x$Co$_{1-x}$O thin film at 2x10^4 V cm^{-1}.

6.5 Fabrication of Mn$_x$Co$_{1-x}$O/MgO

6.5.1 Deposition of Mn$_x$Co$_{1-x}$O on MgO(001) and MgO(111) substrate

The MgO substrates were ultrasonically cleaned in acetone. They were then placed on the substrate holder in the vacuum chamber. The mixed metal oxide (Mn$_x$Co$_{1-x}$O) targets were irradiated with KrF excimer laser. The deposition condition was largely the same as that described in Section 6.4.

6.5.2 Structural characterization

XRD was used to determine the crystallinity and the preferred orientation of all deposited films. The formation of a solid solution of single phase was confirmed and the out-of-plane lattice parameters of the Mn$_x$Co$_{1-x}$O samples were obtained. Fig. 6.13 and Fig. 6.16 show the (002) and (111) diffraction peaks of Mn$_x$Co$_{1-x}$O grown on MgO(001) and MgO(111) substrates, respectively. They reveal the epitaxially growth relationship of the mixed metal oxide films on two different orientations of MgO substrate. Also, the out-of-plane lattice parameters of the oxide films vary fairly linearly with x from 0.429 nm to 0.443 nm. The values decrease with increasing the Co content, in accordance to Vegard's law. In summary, we have demonstrated that the Mn$_x$Co$_{1-x}$O films can be successfully grown on either MgO(001) or MgO(111) substrate with a good crystalline structure.
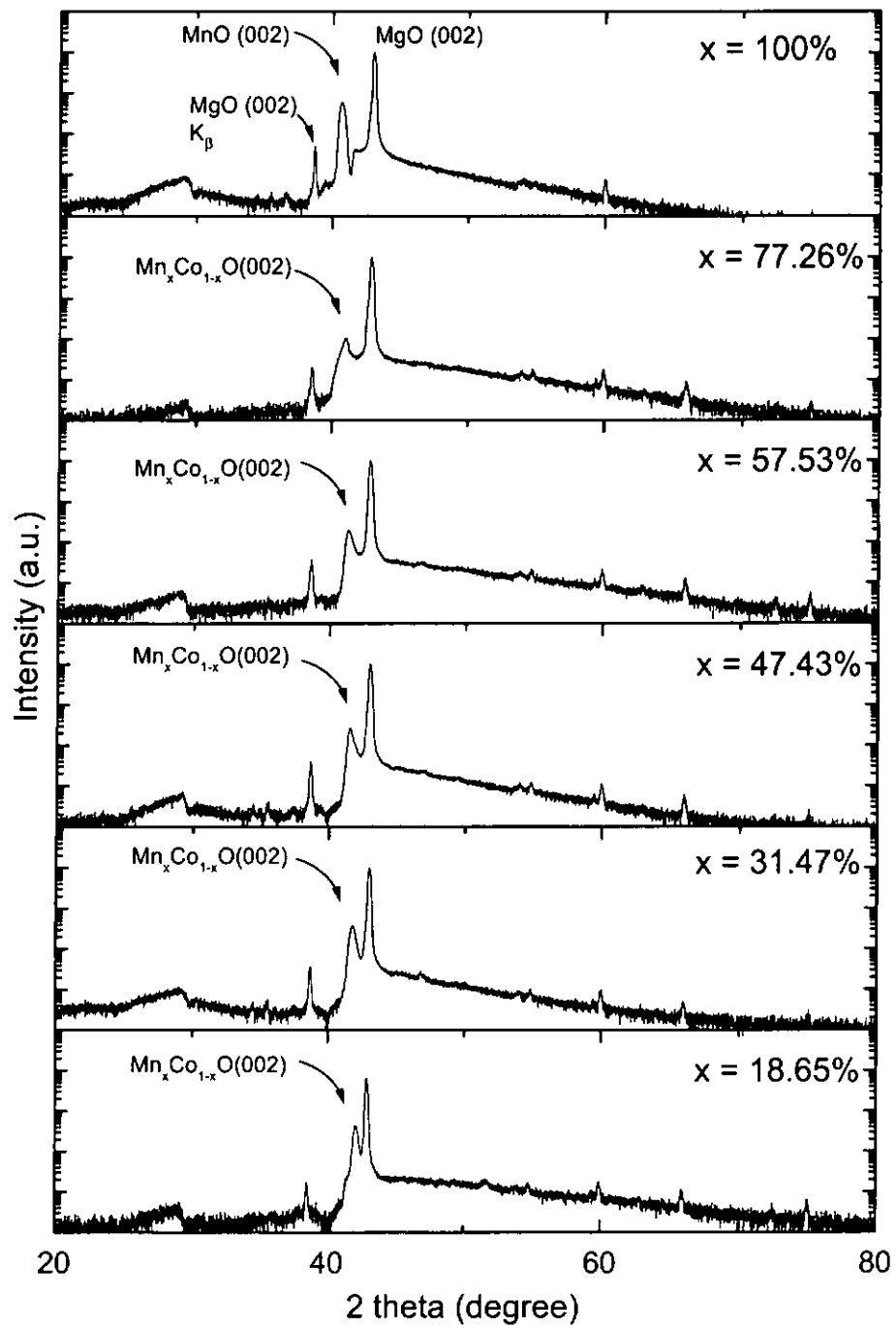
Figure 6.13 XRD patterns for Mn$_x$Co$_{1-x}$O/MgO(001) deposited with different compositions from x = 0.1865 to x = 1.
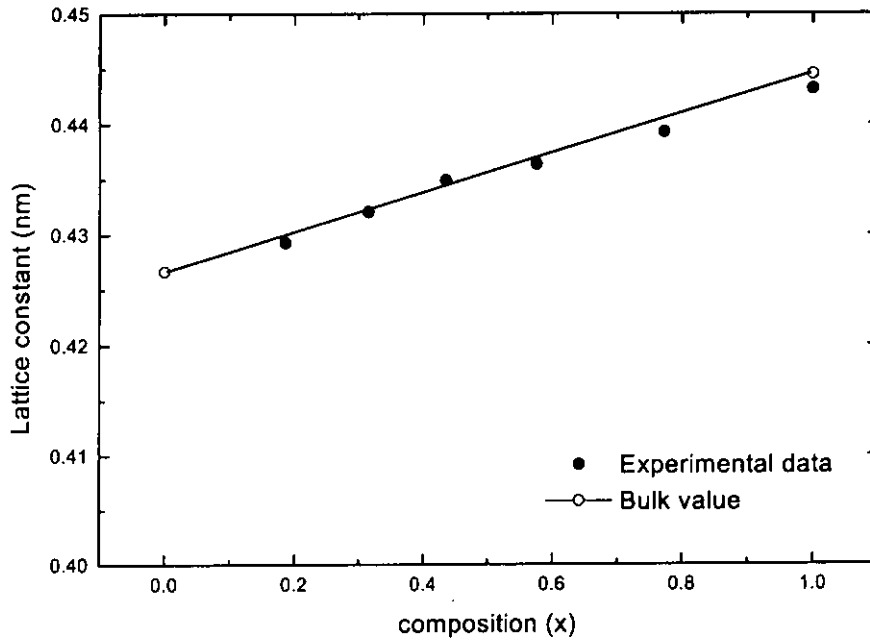
Figure 6.14 Variation of lattice parameter of $Mn_xCo_{1-x}O$ thin films grown on MgO(001) substrates with MnO content.
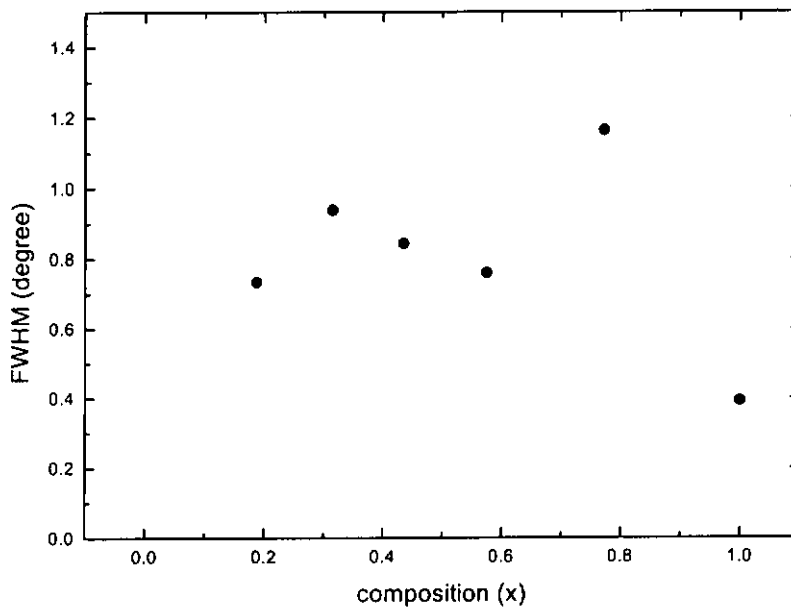
Figure 6.15 The FWHM of $Mn_xCo_{1-x}O$ films deposited on MgO(001) substrates at 600 °C in 2×10^{-5} Torr ambient pressure.
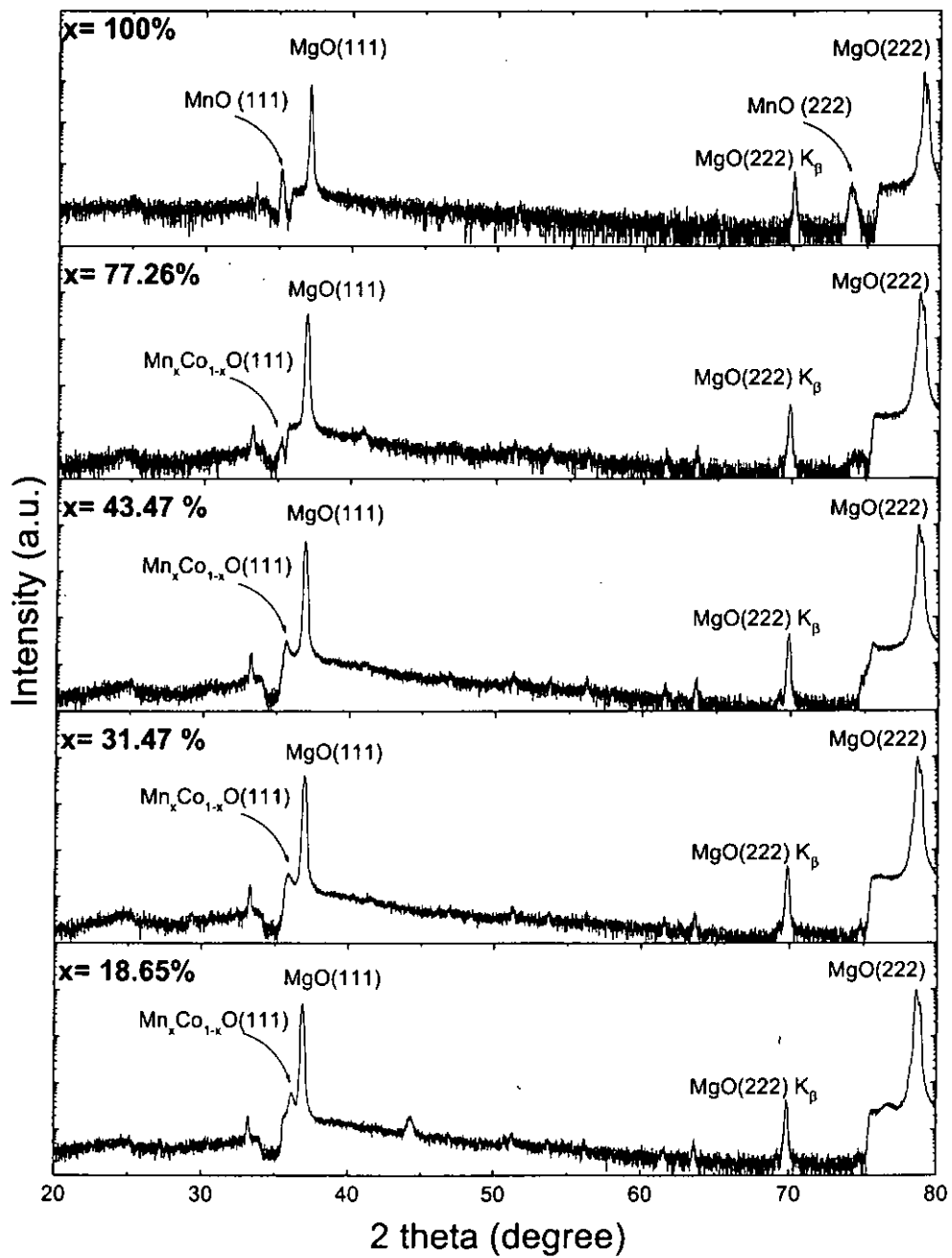
Figure 6.16 XRD patterns for Mn$_x$Co$_{1-x}$O/MgO(111) deposited with different compositions from x = 0.1826 to x = 1.
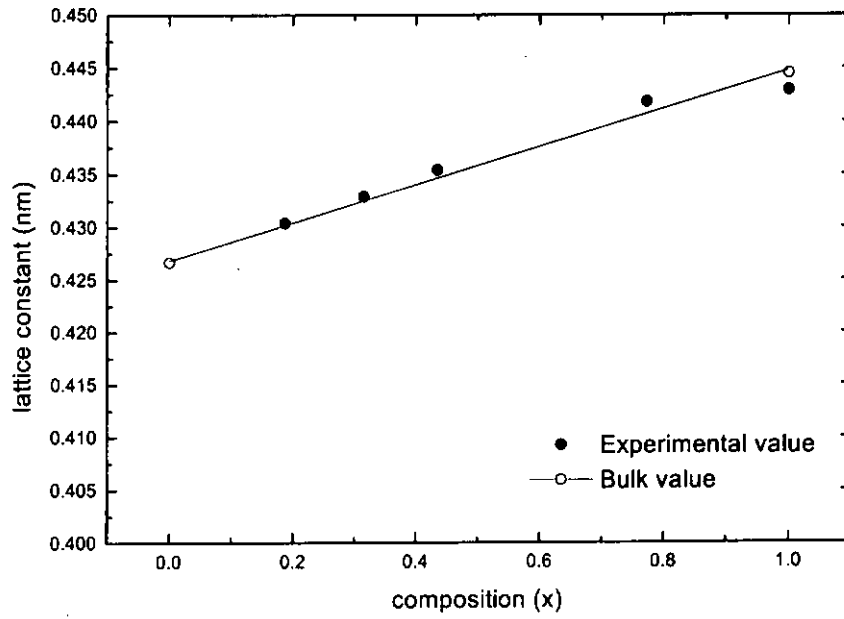
Figure 6.17 Variation of lattice parameter of $Mn_xCo_{1-x}O$ thin films deposited on MgO(111) substrates.
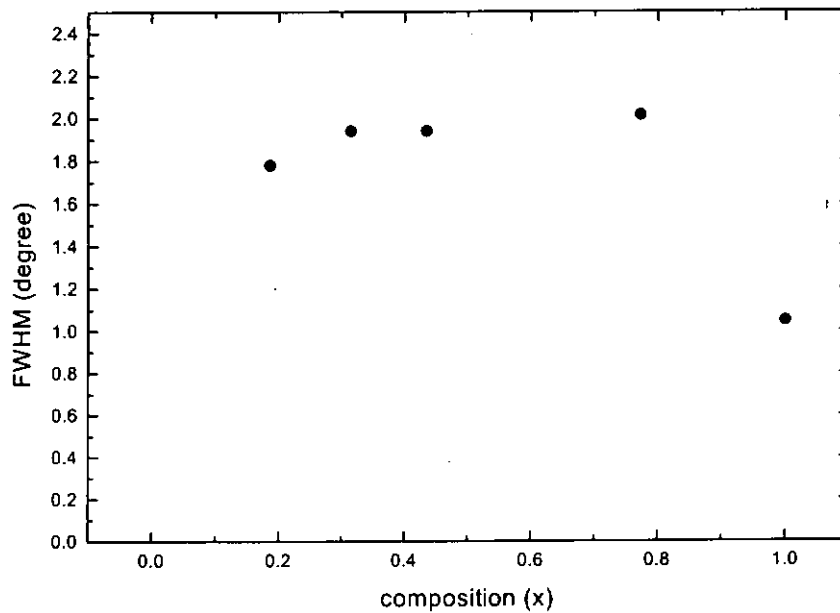
Figure 6.18 The FWHM of $Mn_xCo_{1-x}O$ films deposited on MgO(111) substrates at 600°C in $2x10^{-5}$ Torr ambient pressure.

6.5.3 Electrical transport properties of $Mn_xCo_{1-x}O$

The electrical properties as functions of the manganese oxide content are examined for $Mn_xCo_{1-x}O$ films prepared at 600 °C substrate temperature. The film deposition was carried out in $2x10^{-5}$ Torr and under optimal conditions for the preparation of MnO films. In order to make sure the top Au electrode adhered well to the oxide surface, both samples were annealed at 200 °C in $5x10^{-5}$ Torr for 30 minutes after the deposition of top electrodes.

Fig. 6.19 shows the dependence of electric resistivity of $Mn_xCo_{1-x}O$ films on the manganese content. All samples exhibit semiconducting properties in the temperature range of 300 K to 500 K. The resistivity decreases almost monotonously as the composition x varied from 18.65 % to 1. It means that the pure manganese monoxide has the smallest resistivity. Maximum resistivity occurs for x within the range 31.47 % to 43.47 %, the value of which could not be shown because they are out of the measurable range of the electrometer. In short, the resistivity of the $Mn_xCo_{1-x}O$ films could be controlled by changing the composition.
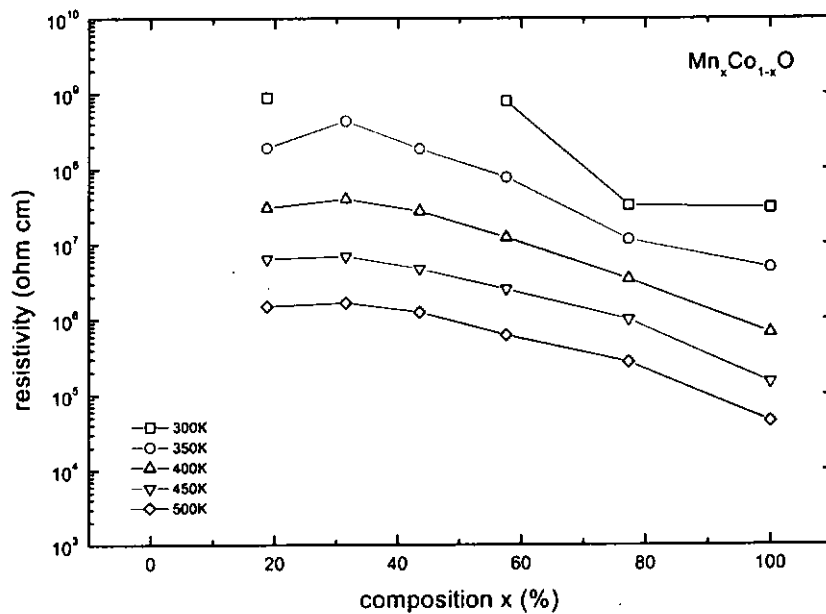
Figure 6.19 Resistivity of epitaxial $Mn_xCo_{1-x}O$ thin film at temperature between 300 K and 500 K.

Fig. 6.20 shows the temperature dependence of TCR parameters for the $Mn_xCo_{1-x}O$ with different compositions. All samples show a negative TCR within 300 K to 500 K temperatures and their response to the temperature is quite different.

According to the experimental results, the thin film resistivity can be changed by altering the relative content of the Mn and Co species, producing a range of rocksalt structured solid solutions. Although the traditional approach to make thermistor sensors has been to use sintered ceramics, we have demonstrated that PLD produced thin films can have electrical properties approaching that of sintered materials.
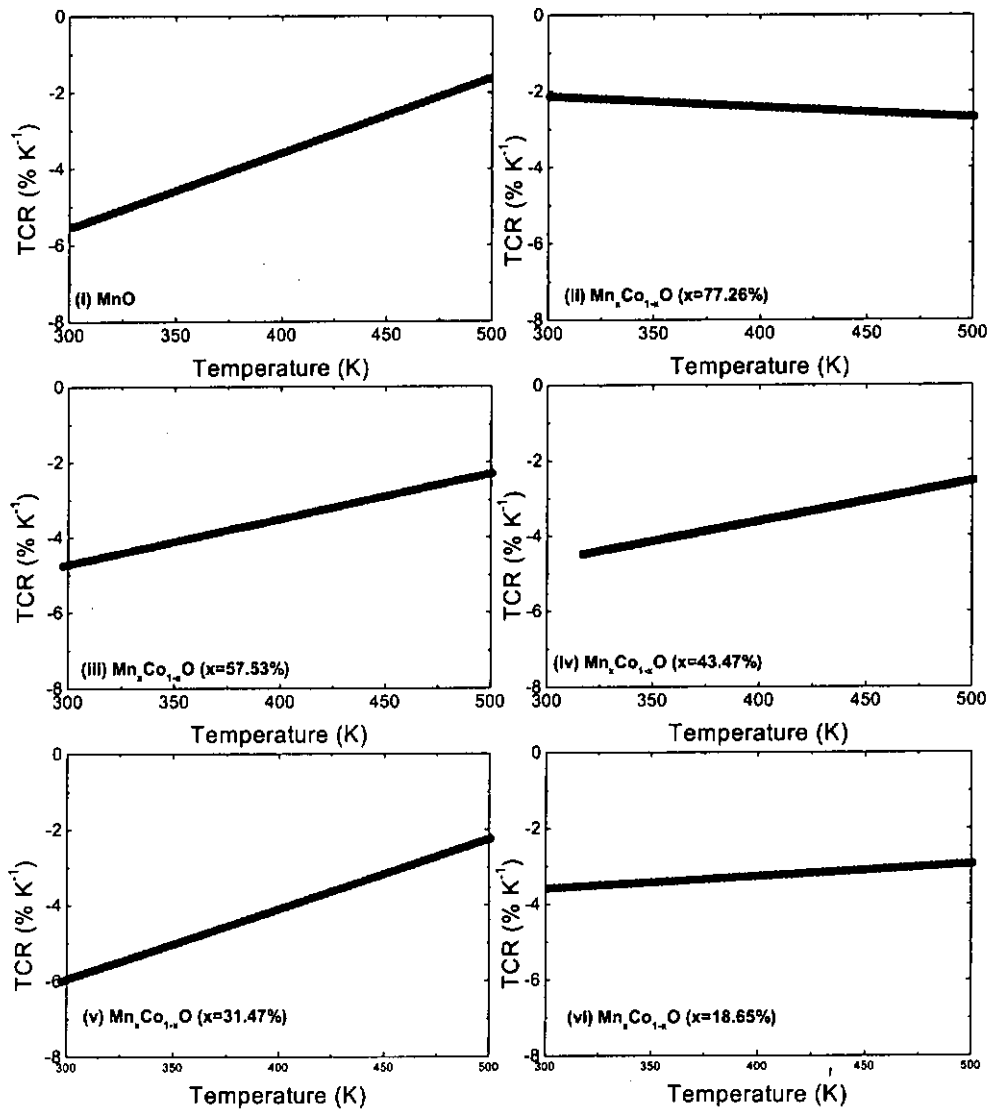
Figure 6.20 Temperature coefficients of the resistivity of different $Mn_xCo_{1-x}O$ films between 300 K and 500 K.

CHAPTER 7

Conclusions

The transition metal monoxide MnO thin films were deposited on TiN buffered silicon and MgO using pulsed laser deposition technique. The ablation target was sintered ceramic with a nominal composition of Mn_3O_4. The surface morphology and crystallinity of the thin films were studied. Electrical properties such as leakage current, dielectric constant and DC conduction were also measured and analyzed from the tri-layer capacitor structure. The relations between the structural and electrical properties of the film were investigated.

Epitaxial MnO films grown on TiN buffered Si(001) substrate have been obtained with a heteroepitaxial relationship of $(001)_{MnO}||(001)_{TiN}||(001)_{Si}$. According to the rocking curve, the FWHM of MnO(002) diffraction peak can be as narrow as $0.61°$. It suggests a very good orientation of the MnO film. The put-of-plane lattice constant of MnO is 0.441 nm, slightly smaller than the relaxed value of 0.444 nm. The small change of lattice parameter may be the results of stress relaxation.

Among the deposition parameters, the substrate temperature and ambient pressure are important in controlling of structure and quality of the grown films. The films were deposited at a wide range of substrate temperature from 200 °C to 800 °C. Their crystallinity and morphology were examined by XRD and SEM. We have demonstrated that the impurity phase of Mn_3O_4 can be successfully removed when

the substrate temperature is higher than 300 °C. The normalized peak intensity and the FWHM of rocking curve of MnO(002) diffraction indicate that a substantial improvement of crystallinity is obtained by increasing the substrate temperature. The effect of substrate temperature on the film surface morphology shows a typical structure–zone model (SZMs). It reveals smooth and crack free surface in MnO film deposited at about 500 °C. A lateral growth with grain sizes larger than the film thickness was observed when the substrate temperature is further increased to 800 °C.

From the deposition pressure studies, the XRD results imply that pure phase of MnO could be obtained at 600 °C over a wide deposition pressure ranging from 2×10^{-5} to 1×10^{-2} Torr. But the corresponding FWHM of rocking curves of MnO(002) varied from 1.33° to 4.66°. The normalized diffraction peak intensity of MnO(002) also drops drastically at higher deposition pressure. Obviously the orientation and crystallinity of the PLD MnO films improve with decreasing deposition pressure.

Dielectric properties of the MnO thin films were studied by fabricating multilayer capacitor structure of MnO insulating layer on silicon substrate with TiN and platinum electrodes. The leakage current measurement of the heterostructure shows a typical metal-insulator-metal capacitor (MIM). At low field, the MnO films exhibit ohmic (linear) conduction with the resistivity of 18.58 Ω cm. The leakage current density-electric field profile is quite symmetric although the two electrodes are different.

Leakage resistance of the MnO capacitor was found to be very sensitive to the fabrication parameters, such as film thickness, substrate temperature and deposition pressure. In the film thickness studies, a substantial reduction of leakage current density from 7.86 to 1.17×10^{-8} A cm^{-2} was obtained for a film thickness change from 34 to 450 nm at an E-field of 1×10^{5} V cm^{-1}.

The relation of substrate temperature and leakage current density was found to be more critical. Generally the leakage current density can be reduced by increasing the substrate temperature. A substantial drop of leakage resistance takes place when the MnO film deposited at 600 °C or higher. It shows a value of 1.2×10^{-3} A cm^{-2} at 500 °C to 8.97×10^{-7} A cm^{-2} at a 600 °C substrate temperature. From data of our investigation, we believed that 600 °C substrate temperature is effective to remove the large number of small grain boundaries which act as scattering centers and current paths for current leakage.

According to the experiment results from the laser ablation studies, the optimal condition for MnO film deposition was deduced. Using a laser beam of fluence of 4 J cm^{-2}, a 600 °C substrate temperature and 2×10^{-5} Torr deposition pressure can produce good quality of MnO films. The room temperature dielectric constant of the Pt/MnO/TiN capacitor was found to be 17.4 with a low dissipation factor of 0.049 at frequency of 0.1 MHz. This dielectric constant is only slightly smaller than the bulk sample value of 18.8.

The successful integration of epitaxial MnO layer on silicon substrate through the TiN buffer system suggests a potential application based on the strong magnetic properties of MnO. Indeed this materials system has good prospects for electronic and magnetic memories as well as spintronics.

In order to study the electrical conduction properties, MnO films were fabricated on insulating MgO single crystal substrates. Highly oriented MnO phase was observed and an epitaxial relation of (001) $_{MnO}$|| (001) $_{MgO}$ was demonstrated. In comparison with the MnO crystal structure deposited on TiN buffered Si, a much better quality MnO film was obtained from deposition directly on template surface of MgO. The effect of deposition parameters on the crystal structure was quite similar to that deposited on TiN buffered Si.

Resistance-Temperature measurement on the MnO films has been carried out. Results show that the 250 nm thick MnO films grown under optimized deposition conditions display a semiconducting behavior. The room temperature resistivity was found to be 70 MΩ cm. The linear plot of ln(ρ/T) against 1/T suggests that the MnO film is a small polaron hopping semiconductor. A hopping energy of 0.51 eV was deduced.

The influences of deposition pressure on the electrical conduction of MnO films were also studied. The room temperature resistivity was decreased continuously by increasing the deposition pressure. There is almost an order of magnitude difference in resistivity for samples prepared at 2×10^{-5} and 1×10^{-2} Torr

ambient pressures. Within 300 K to 500 K temperatures, both samples show semiconducting transport behavior. However, films deposited in pressure higher than 1×10^{-4} Torr exhibit a non-linear relation in the plot of $\ln(\rho/T)$ against $1/T$. It suggests that the MnO films deposited in high pressure no longer obey the small polaron hopping mechanism. A maximum of temperature coefficient of resistance (TCR) of 5.9 % K^{-1} at room temperature was obtained when the MnO films were deposited in 1×10^{-4} Torr.

The magnetic transition of MnO was also studied. A heterostructure of Au/MnO/TiN/MgO(111) was fabricated by PLD. XRD results revealed a heteroepitaxial relation of $(111)_{MnO} \parallel (111)_{TiN} \parallel (111)_{MgO}$. The MnO film was highly oriented with a rocking curve FWHM of 0.7°. The good crystallinity of MnO suggests successful removal of crystal twinning. The magnetic transition, which shows up as a dielectric anomaly at Néel temperature, was not observed in our thin film samples. This is attributed to the internal stress built up in the film which inhibits the proper structural distortion.

We have also shown that pulsed laser deposition is a suitable technique for depositing mixed metal oxide such as $Mn_xCo_{1-x}O$. Films with manganese–cobalt ratio from 0.187 to 1 have been prepared. With increasing cobalt content, the lattice parameter of the rocksalt structure decreases from 0.441 to 0.426 nm.

$Mn_xCo_{1-x}O$ layers were deposited on MgO(001), MgO(111) and TiN/Si(001). Heteroepitaxial relation of $(001)_{(Mn,Co)O} \parallel (001)_{MgO}$, $(111)_{(Mn,Co)O} \parallel (111)_{MgO}$ and

$(001)_{(Mn,Co)O} \| (001)_{TiN} \| (001)_{Si}$ were obtained. The successful growth of the epitaxial $Mn_xCo_{1-x}O$ films on different substrates suggests that the $Mn_xCo_{1-x}O$ can act as templates of variable lattice constant (0.441 to 0.426 nm) for strain layer growth.

Electric resistivity measurements on the $Mn_xCo_{1-x}O$ films with different manganese content have been carried out. Results show that all samples exhibit semiconducting properties in the range of 300K to 500K. The large temperature dependent resistivity of the $Mn_xCo_{1-x}O$ films could be controlled by changing the composition from x =1 to 0.187. It also means that $Mn_xCo_{1-x}O$ films have good potential for use in negative temperature coefficient (NTC) thermistor.

In view of the successes in growing pure MnO phase thin films, PLD technique is expected to be applicable to grow other transition metal oxides, such as NiO, CoO, CdO and ZnO, and their mixed oxides. Similar studies as our present work can be done. Together with the possibility of integrating with Si, research on this aspect can lead to potential materials systems fit for spintronics and chemical sensor.

References

Blanton, T. N. and Liang-Sun Hung, *The Rigaku Journal,* **13** (1996) 3

Bykovskii, Yu.A, Boyakov, V.M., Galochkin, V.T., Molchanov, A.S., Nikolaev, N.I. and Oraevskii, A.N., *Sov. Phys. Tech. Phys.* **23** (1978) 578

Chandhury, A.K. and Rao, K.V., *Phys. Status Solidi.* **32** (1969) 731

Davies, M.W. and Richardson, F.D., *Trans. Fara. Soc.* **55** (1959) 604

Dax, M., *Semicond. Int.* **20**, (1997) 24

Dijkkamp, D., Venkatesan, T., Wu, X.D., Shaheen, S.A., Jisrawi, N., Min-Lee, Y.H., McLean, W.L., and Croft, M., *Applied Physics Letter.* **51**, (1987),619

Fujimori, Y., Kume, S., and Usami, S., *Appl. Surf. Sci.* **70/71** (1993) 351

Galasso, F.S., *Structure and Properties of Inorganic Solids, first ed.,* Pergamon Press, (1970)

Girault, C., Damiani, D., Aubreton, J. and Catherinot, A. *Appl. Phys. Lett.* **55** (1989) 182

Greene, J. E. (1993) in *Multicomponent and Multilayered Thin Films for Advanced Microtechnologies* (O. Auciello and J. Engemann, eds.), NATO/ASI Series E **234**, Kluwer Academic Publishers, The Netherlands (1993) 39

Goodenough, J.B., Progr. *Solid State Chem.* **5** (1971) 260

Gupta, B.R.K. and Verma, M.P., *J. Phys. Chem. Solids.* **38** (1977) 929

Harvey, K.C. and Fehrenbach, Jr., *Rev. Sci. Instr.* **54** (1983) 1117

Haupt, L. von Helmolt, R., Barner, K., Sondermann, U., *Solid State Commun.* **82** (1992) 693

Haywood, B.C. and Collins, M.F., *J. Phys. C* **4** (1971) 1299

Hed, A.Z. and Tannhauser, D.S., *J. Electrochem. Soc.* **114** (1967) 2090

Henrich, V.E., Cox, P.A., *The Surface Science of Metal Oxides,* Cambridge University Press, (1996)

Jarzebski, Z. M., *Oxide Semidoncuctors,* Pwrgamon Press, 1973

Hotzl, J. Z. *Phys.* **151** (1958) 220

Keyser, M.J., Everson, R.C., Espinoza, R.L., *All. Catal. A* **171** (1998) 99

Kinney, T.B. and O'Keeffe, M. *Solid State Commun.* **7** (1969) 977

Langell, M.A., Hutchings, C.W., Carson, G.A. and Nassir, M.H., *J.Vac.Sci. Technol.A* **14** (1996) 3

Levason, W. and McAuliffe, C.A., Coord. *Chem. Rev.* **7** (1972) 353

Lynds, L., B.R. Weinberger, D.M., Potrepka, G.G., Pterson, and M.P. Lindsay, *Physica.* C **159** (1989) 61

Massidda, S., Posternak, M. and Baldereschi, A., *Phys. Rev. Lett.* **82** (1999) 2

Mattox, D.M., *Film Deposition Using Accelerated Ins*, Rec. SC-DR-281-63, Sandia Corp (1963)

Muller, F., de Masi, R., Reinicke, D., Steiner, P., Hufner, S., Stowe, K., *Surf. Sci,* **520** (2002) 158-172

Narayan, J., Tsvetanka Zheleva. and Jagannadham, J., *J. Appl. Phys.* **75** (1994) 2

Neubeck, W., Ranno, L., Hunt, M.B., Vettier, C., and Givord, D., *Appl Sci.* **138-139** (1999) 195-198

Nicolet, M.A., *Thin Solid Films*. Vol. **52**, (1978) 415

Norifumi Fujimuraand Tairo Ito, *Appl. Surf. Sci.* **41-42** (1989) 272-276

Pai, M. and Honig, J. M., *J. Solid State Chem.* **30** (1981) 59

Passerini, L., Gazz. Chim. Ital. **59** (1929) 139

Pearson, W.B., *A Handbok of Lattice Spacings and Structures of Metals and Alloys*, Pergamon Press, New York, (1958)

Prinz, G., Hathaway, K., *Phys. Today.* **48**, (1995) 24

Rainer, D.R., Goodman, D.W., *J. Mol. Cat.* **1-3** (1998) 131

Ramesh, R., Luther, K., Wilkens, B., Hart, D. L., Wang, E., Tarascon, J. M., Inam, A., Wu, X. D., and Venkatesan, T., *Appl. Phys. Lett.* **57** (1990) 1505

Ramesh, R., *Thin Film Ferroelectric Materials and Devices*, Kluwer Academic Publishers, Boston, (1997)

Rizzi, G.A., Zanoni, R., Di Siro, S., Perriello, L. and Granozzi, G., Surf. Sci. **462** (2000) 187

Roth, W.L. *Phys. Rev.* **110** (1958) 1333

Seehra, M.S. and Jagadeesh, M. S., *Phys. Rev B.* **23** (1981) 1185

Schwart, H.., Tourtelotte, H.A., *J. Vac. Sci. Technol.* **6** (1969) 373

Singh, R. K., Holland, O.W., and Narayan, J., *Journal of Applied Physics.* **68** (1990) 233

Suryanaryana, C., Grant Norton., M., *X-Ray Diffraction, Plenum Press,* New York and London, (1998)

Toth, L.E., *Transition metal carbides and nitride,* Academic, New York (1971)

Wittmer Marc, *Apl. Phys.* **53** (1982) 1007